UCRL-17794
cy. 2

University of California

Ernest O. Lawrence Radiation Laboratory

KINETICS OF VAPORIZATION OF SODIUM CHLORIDE

Joseph Eugene Lester
(Ph.D. Thesis)

December 1967

RECEIVED
LAWRENCE
RADIATION LABORATORY

TWO-WEEK LOAN COPY

This is a Library Circulating Copy which may be borrowed for two weeks. For a personal retention copy, call Tech. Info. Division, Ext. 5545

UCRL-17794
cy. 2

DISCLAIMER

This document was prepared as an account of work sponsored by the United States Government. While this document is believed to contain correct information, neither the United States Government nor any agency thereof, nor the Regents of the University of California, nor any of their employees, makes any warranty, express or implied, or assumes any legal responsibility for the accuracy, completeness, or usefulness of any information, apparatus, product, or process disclosed, or represents that its use would not infringe privately owned rights. Reference herein to any specific commercial product, process, or service by its trade name, trademark, manufacturer, or otherwise, does not necessarily constitute or imply its endorsement, recommendation, or favoring by the United States Government or any agency thereof, or the Regents of the University of California. The views and opinions of authors expressed herein do not necessarily state or reflect those of the United States Government or any agency thereof or the Regents of the University of California.

UCRL-17794

UNIVERSITY OF CALIFORNIA
Lawrence Radiation Laboratory
Berkeley, California

AEC Contract No. W-7405-eng-48

KINETICS OF VAPORIZATION OF SODIUM CHLORIDE

Joseph Eugene Lester

(Ph.D. Thesis)

December 1967

TABLE OF CONTENTS

ABSTRACT

I. INTRODUCTION 1

II. VAPORIZATION MODELS AND THEORETICAL CONSIDERATIONS 4

III. CRYSTALS 12

A. Pure Commercial Crystals 12

B. Crystal Purification and Growth of High Purity NaCl Single Crystals 12

C. Doped Crystals 19

D. X-Ray Irradiated Crystals 21

E. Strained Single Crystals 21

IV. EXPERIMENTAL APPARATUS AND PROCEDURES 26

A. General Apparatus Design Considerations 26

B. Microbalance System 31

C. Mass Spectrometer System 41

D. Experimental Procedure 48

1. Crystal Preparation 48

2. Weight Loss Experiments 49

3. Mass Spectrometer Experiments 50

V. ANALYSIS OF EXPERIMENTAL DATA 55

A. Microbalance Results 55

B. Mass Spectrometric Data 58

VI. EXPERIMENTAL RESULTS 65

A. Sample Identification 65

B. Total Evaporation Rates of Several NaCl Crystals (Microbalance Studies) 65

Table of Contents (Continued)

C. Vapor Compsoition and Activation Energies of Vaporization of NaCl (Mass Spectrometric Studies)..... 69

1. Knudsen Effusion Experiment on NaCl 69

2. Annealed and Untreated Crystals 71

3. Impurity Containing Crystals 71

4. High Dislocation Density Crystals 80

VII. DISCUSSION 92

A. Effect of Dislocation Density on the Vaporization Characteristics of NaCl 92

B. Effect of Impurities on the Evaporation Behavior of NaCl 95

C. Comments on the Mechanism ofVaporization of NaCl..... 96

D. Suggestions for Further Experiments to Test the Proposed Model 100

ACKNOWLEDGMENTS 101

APPENDICES

A. Theory of Quadrupole Mass Filter 102

B. Quadrupole Mass Transmission and Ionization Cross-Sections 108

C. Mass Spectrometric Data Analysis 111

D. Symbols Used..... 117

REFERENCES 119

KINETICS OF VAPORIZATION OF SODIUM CHLORIDE

Joseph Eugene Lester

Inorganic Materials Research Division, Lawrence Radiation Laboratory,
and Department of Chemistry,
University of California, Berkeley, California

ABSTRACT

The kinetics of vaporization of sodium chloride single crystals into vacuum have been investigated using microbalance and mass spectrometric techniques in the temperature range 450°C to 650°C. The total evaporation rate from the (100) face of high purity single crystals of low dislocation density (etch pit count ~ $1\times10^6/cm^2$) was found to be lower than the maximum rate calculated from the equilibrium pressure by a factor of two. The activation energy of vaporization for these crystals was 52.6±1 and 62.1±1 kcal/mole vapor for the monomer (NaCl) and dimer (Na_2Cl_2) molecules, respectively. The monomer to dimer ratio in the vapor is given by $\log M/D = -1.17\pm.2 + 2.0\pm.1\times10^3/T$. The total rate of vaporization and the activation energy of vaporization were dependent on the dislocation density. The evaporation rate of crystals having etch pit densities of ~ $10^7/cm^2$ was equal to the maximum equilibrium rate. These crystals had activation energies from 2-4 kcal/mole higher than the crystals with low dislocation densities. The dependence of the vaporization rate on the presence of various cation and anion impurities have also been studied. A model of the vaporization mechanism of NaCl is presented and discussed.

I. INTRODUCTION

The vaporization of solids has been the subject of many studies since the early 20th century. Most of the investigations have been studies of the solid-vapor equilibria,[1,2] primarily, studies of the vapor pressure of the solid. These studies were performed to establish thermodynamic properties of the substance. Relatively little attention has been paid to the kinetics of the vaporization reaction, that is the steps by which a solid constituent breaks away from the lattice on the vaporizing surface. Recently, several investigations[3] have shown that the actual rate of vaporization into vacuum can be as much as several orders of magnitude lower than the rate calculated from equilibrium pressure measurements. However, the only studies which attempted to correlate the evaporation behavior to the properties of the solid state have been performed using As_2O_3,[4] S,[5] As,[6,7] P,[6] and CdS.[8] A review of the probable mechanisms for the vaporization of these materials may be found in the literature.[9,10,11]

Reviews of the theoretical approaches to vaporization kinetics and of the role of crystal imperfections in crystal growth and vaporization may also be found in the literature.[9,12-14]

The purpose of this investigation was to explore the mechanism of vaporization of ionic solids which do not dissociate to the elements upon evaporation, in particular, the alkali halides. The availability of single crystals of reasonably high purity, which are essential for definitive vaporization studies,[11] makes these materials attractive for study. In addition their thermodynamic[15] and electrical properties[16] are well known. Another advantage is that the potential energy of an ion or molecule in the

crystal lattice or at the surface can be calculated to a reasonable accuracy using semi-classical techniques.[17-20] Thus, an experimental study of the evaporation kinetics of the alkali halides should be complementary to the development of a theoretical model of the kinetics of vaporization of ionic solids.

We have studied the evaporation behavior of the (100) face of sodium chloride single crystals under a wide range of conditions of the solid. This face was chosen because it is known to be the most stable crystal face (a crystal cut to another orientation and allowed to equilibrate will facet to expose (100) atomic planes). The solid vaporizes according to the dominant net reaction

$$NaCl\ (solid) \rightarrow (1-X)\ NaCl\ (vapor) + x/2\ Na_2Cl_2\ (vapor)$$

In the temperature range of our investigation (450°C to 650°C) and under the different vaporization conditions the dimer is roughly 5-30 mole % of the vapor. The monomer/dimer ratio is somewhat greater for conditions of free vaporization into vacuum than for vaporization from an effusion cell.[22]

In order to explore the kinetics and mechanism of NaCl vaporization the following studies were performed. The total evaporation rate of one face of a single crystal was measured as a function of temperature using a vacuum microbalance. The vapor composition and the vaporization activation energies of the monomer and dimer were determined using a mass spectrometer. We have investigated the effect of lattice defects (dislocations) and the effect of certain impurities (Ca^{++}, Br^-, OH^-, O_2^-) on the vaporization rate and vapor composition. Ultra high purity NaCl crystals were grown from zone refined crystals in order to study the vaporization

kinetics of impurity free material.

We found that dislocations changed both the activation energies and total evaporation rate of NaCl, and that divalent cation impurities affected the activation energy. Anion impurities had no observable effect. We also present a possible mechanism for the vaporization of sodium chloride which is in accord with the available data.

II. VAPORIZATION MODELS AND THEORETICAL CONSIDERATIONS

The purpose of this section is to examine the current state of the theory of evaporation kinetics. The discussion will not attempt to be complete, in that there are several good review articles in the field.[9,11] All of the theories which have sought to explain the kinetics of vaporization from the properties of the solid have used a monatomic solid as their model. These theories consider only the movement of atoms in space and in general, are based explicitly or implicitly on an equilibrium model. It has been shown that these theories do not apply to the vaporization of II - VI semiconductors where a charge transfer or redistribution process if "rate limiting".[11] It is doubtful whether they are applicable to the vaporization of ionic solids but their consideration is warranted because they illustrate the general approach to vaporization behavior of solids.

The earliest attempt to explain the rate of vaporization of a solid was made by Langmuir.[23] From the kinetic theory of gases the rate at which molecules in a gas strike a unit surface is given by:

$$\frac{dN}{dt}\ (\text{molec/cm}^2\text{sec}) = \rho_v\ \bar{v}/4 \qquad (1)$$

where ρ_v is the gas density, and $\bar{v}$ is the average gas velocity.* Using (1), the ideal gas equation, and assuming the velocity distribution to be Maxwellian, then

---

* A list of definitions of symbols used may be found in Appendix D.

$$\frac{dN}{dt} = P_{eq} \, (2 \, \pi \, m \, k \, T)^{-1/2} \qquad (2)$$

where m is the weight of a molecule of the gas. Langmuir postulated that the evaporation rate of a solid into vacuum was given by Eq. (2). This assumption has been proven not to be the case for a large number of solids,[11] and indeed, there is no a priori reason why the number of molecules evaporating from a surface under non-equilibrium conditions should be equal to the kinetic theory expression (Eq. 2).[24]

Neuman[25] has considered the evaporation rate of a surface of N_s molecules, all having a heat of vaporization E_v, assuming that the energy distribution of the particles is Maxwellian. He found for a system of harmonic oscillators:

$$\frac{dN}{N_s dt} = \left(\frac{kT}{2\pi \, m}\right)^{1/2} e^{-\epsilon_o/kT} \; \frac{\left(\frac{2\pi m \, kT}{h^2}\right)^{3/2} e^{-E_v/kT}}{e^{-\epsilon_o/kT} \prod_{i=1}^{3N} \left(1-e^{-h\nu_i/kT}\right)^{-1}} \qquad (3)$$

where ϵ_o is the zero point energy of the solid. The denominator is equal to the vibrational partition function of the solid Q^c_{vib}. Equation (3) can be written as:

$$\frac{dN}{N_S dt} = \frac{\bar{v}}{4} \; \frac{Q^v_{trans}}{Q^c_{vib}} \; e^{-E_v/kT} \qquad (4)$$

where Q^v_{trans} = translational partition function of gas. Since

$$\frac{Q^v_{trans} \; Q^v_{int}}{Q^c_{vib} \; Q^c_{int}} \; e^{-E_v/RT} = \frac{Q^v_{tot}}{Q^c_{tot}} \; e^{-E_v/RT} = \rho^v_{eq}/\rho^c_{eq}$$

than
$$\frac{dN}{dt} = \frac{\bar{v}}{4} \rho^{v}_{eq} \frac{Q^{c}_{int}}{Q^{v}_{int}} \qquad (5)$$

where
$$Q^{c}_{int}/Q^{v}_{int} = \alpha_{v} \quad .$$

α_v is the vaporization coefficient. Thus, the rate is only equal to the equilibrium rate, in this approximation, if the internal partition functions of the solid and vapor are equal. Since Q^{v}_{int} includes the rotational, vibrational, and electronic partition functions for the vapor and Q^{c}_{int} includes only the rotation and electronic partition functions, then α_v for a polyatomic molecule cannot be unity in this model and should be approximately $\alpha_v = 1/Q^{v}_{vib}$.

Kossel[26] and Stranski[27] postulated that the surface of a crystal is non-uniform energetically and that several characteristic atomic positions are important in growth and vaporization phenomena. Figure II-1 shows a model of a simple cubic lattice with these sites labeled. The most important position is the so-called "kink" or "half-crystal" (position 1/2 in Fig. II-1) as the removal (addition) of an atom from this position constitutes a repeatable (site self-replicating) step in the vaporization (growth) of the lattice. Burton, Cabrera, and Frank[28] have calculated the equilibrium concentration of "kink" positions in steps occurring on the surface of a simple solid taking into account (nearest and next-nearest neighbor interaction energy in a simple cubic lattice or face centered cubic lattice). They find that d_o, the mean distance between kinks, is

$$d_o = a/2 \left(e^{w_1/kT} + 2\right) \qquad (6)$$

where a is the lattice spacing and w_1 is the formation energy of a single kink. For a (10) step on a (100) face of a simple cubic lattice with

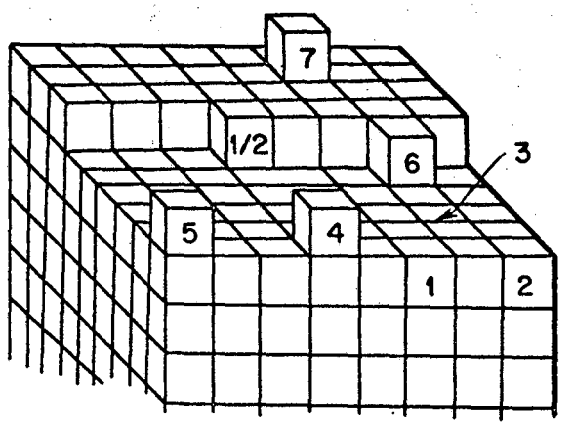

XBL679-5257

Fig. II-1 Kossel-Stranski model of a crystal surface

only nearest neighbor interactions:

$$w_1 \sim 1/6\ E_c$$

where E_c is the energy of crystallization of the lattice. At $E_c/kT = 24$:

$$d_o \sim 300\ \mathring{A}\ .$$

However, they also show that, for low index faces on crystals having nearest neighbor and/or next nearest neighbor interactions, lattice steps are not an equilibrium feature but must arise from dislocations or other non-equilibrium imperfections. Hirth and Pound[29] have used this model of the crystal surface to calculate the rate of vaporization. The assumptions in their derivation are:

1) edges of the crystal serve as ledge sources and the edge spacing is large compared to the ledge spacing.

2) the energy of an atom is proportional to the number of nearest neighbors.

3) the number of kinks in, and atoms at a ledge are equal to their equilibrium number.

They find that surface diffusion of atoms away from the ledge is important in establishing the vaporization rate in this model. The derivation is long and will not be repeated here; the results for α_v, the vaporization coefficient, are:

$$\alpha_v = (2\bar{x}/\bar{\lambda})\ \tanh\ (\bar{\lambda}/2\bar{x}) \qquad (7)$$

where

$$\bar{x} = (D_s/\nu)^{1/2}\ \exp\ (\Delta F^*_{des}/2kT)$$

equals the mean free path for random walk of an adsorbed atom on a close

packed surface, ν = vibration frequency of atoms on the metal surface, D_s = surface self-diffusion coefficient, ΔF^*_{des} = free energy of activation for desorption of an atom from surface to vapor, and $\bar{\lambda}$ represents the average spacing between monatomic ledges on the surface. For the values of $\bar{\lambda}/\bar{x}$ calculated in their derivation:

$$\alpha_v = 2/3\ (P/P_{eq}) + 1/3 \qquad (8)$$

Thus, α_v should be 1/3 when a solid vaporizes into vacuum and should increase to unity when $P = P_{eq}$. This result will only be valid (in this approximation) when the density of ledge sources other than crystal edges is small. Of course, the application of these results to a real crystal depends upon the applicability of the hypotheses to the crystal. Several investigators have found that the ledge spacing on alkali halides is pressure dependent[30,31] and it is also known that the energy of an ion in the lattice depends on more than its number of nearest neighbors, thus the hypotheses seem not to fit the alkali halides.

These calculations indicate that the evaporation rate will be proportional to the area of the sample only when the dislocation density of the solid is low enough to make a negligible contribution to the total ledge (step) length on the crystal surface. For higher dislocation densities, α_v should approach unity. Hirth and Pound[32] calculated that a screw dislocation density of $10^6/cm^2$ is necessary before α_v would become appreciably larger than 1/3. At this point, one must comment that this is essentially an equilibrium theory which has been modified to account for the displacement of the system from equilibrium. The validity of the theory depends on how strongly dependent the concentrations and rate

constants (energies of motions) are on the evaporation rate and structure of the surface.

Essentially the state of evaporation theory is such that the gross features may be explained but the atomistic picture is incomplete. It is hoped that the accumulation of experimental information on the evaporation kinetics of solids of different types (ionic, molecular, metallic, covalent) will allow the formulation of a realistic model of solid vaporizations.

It is informative to consider the conditions necessary for the activation energy to be equal to the equilibrium energy of vaporization, if the final desorption step is the "rate limiting step". Let the vaporization of a solid be considered to occur as a series of simple reactions:

$$A(1/2) \underset{k_2}{\overset{k_1}{\rightleftharpoons}} A(\ell) \qquad k_1/k_2 = K_1 = e^{-\Delta F^\circ_{12}}$$

$$A(\ell) \underset{k_4}{\overset{k_3}{\rightleftharpoons}} A(s) \qquad k_3/k_4 = K_3 = e^{-\Delta F^\circ_{34}}$$

$$A(s) \underset{k_6}{\overset{k_5}{\rightleftharpoons}} A(g) \qquad k_5/k_6 = K_5 = e^{-\Delta F^\circ_{56}}$$

where $k_i = \nu_i \, e^{-E_i^*/RT}$, 1/2 = kink or half-crystal position, ℓ = ledge, s = surface, g = gas, A(n) = concentration at n, and ν_i is a frequency factor. Then, if the system is in equilibrium,

$$\frac{A(g)}{A(k)} = \frac{k_1}{k_2} \frac{k_3}{k_4} \frac{k_5}{k_6} = e^{-(\Delta F^\circ_{12} + \Delta F^\circ_{34} + \Delta F^\circ_{56})/RT}$$

or

$$\frac{d \, \ell n \, A(g)}{d \, 1/T} = \frac{-(\Delta H^\circ_{12} + \Delta H^\circ_{34} + \Delta H^\circ_{56})}{R} = \frac{-\Delta H^\circ_v}{R}$$

Now if the flux from the gas to the surface is zero (free vaporization) but one assumes that all the preceding reactions stay at equilibrium, then

$$\frac{A(s)}{A(k)} = e^{-(\Delta F^{\circ}_{12} + \Delta F^{\circ}_{34})/RT}$$

and

$$A(g) = A(s)\ \nu_5\ e^{-E_5/RT}$$

$$A(g) = A(k)\ \nu_5\ e^{-(\Delta F^{\circ}_{12} + \Delta F^{\circ}_{34} + E^{*}_{5})/RT}$$

thus

$$\frac{d\ \ell n\ A(g)}{d^{1/T}} = \frac{-(\Delta H^{\circ}_{12} + \Delta H^{\circ}_{34} + E^{*}_{5})}{R}$$

Therefore, for the measured activation energy of vaporization to be equal to ΔH°_{v}, $E^{*}_{5} = \Delta H^{\circ}_{56}$. This implies that there is no energy barrier to desorption of the molecule from the surface. Therefore if this last desorption step is to be "rate limiting" (all previous reactions at equilibrium) it must be because the pre-exponential factor in this rate constant is small. Then, the evaporation coefficient and condensation coefficient cannot be exponentially temperature dependent because there is no energy barrier to either process.

III. CRYSTALS

A. Pure Commercial Crystals

The majority of the sodium chloride single crystals used in this research were purchased from the Harshaw Chemical Company.[33] They were optical grade crystals of nominal 99.99% purity and were single crystal. The pieces were approximately 2 cm^3 in volume and were bounded by (100) cleavage planes. This last fact made orientation of the crystals quite trivial. The crystals were purchased in two lots. Both lots were analyzed for cation impurities. The second lot was also analyzed for some anion impurities. The concentrations of cation impurities were almost identical in the two lots. The results of the analyses are shown in Table III-I (Lots I and II). The anion impurity concentration brings the actual purity level down to about 99.95%. The Harshaw crystals were grown by a Bridgman[34] technique under a nitrogen atmosphere. A number of the pieces in the second lot seemed to have low angle twin boundaries on some faces and were not used in the evaporation studies. These crystals were cleaved to the appropriate sample size, or annealed at 500°C for 16-36 hr in a quartz tube which had been sealed off under vacuum and then cleaved to size for use in the vaporization experiments.

B. Crystal Purification and Growth of High Purity NaCl Single Crystals

Because of the high anion impurity concentration in the Harshaw crystals which was suspected of being responsible for the irreproducibility of the early experimental data, it was decided to grow some crystals by a modified Kryopoulos[35] technique. In order to reduce the bromine and oxygen containing impurity concentrations the reagent grade starting material was

Table III-1 Impurity analysis of sodium chloride crystals used.[1]

Lot	I	II	III	IV	V
Description	Harshaw	Harshaw	Semi-Element	Zone Refined	Br^- doped
Impurity					
Al	P < 1	P < 1	5	ND	ND
Ba	ND < 4	ND < 4	ND	P < 10	P < 10
Ca	P < 1	P < 1	40	ND	ND
Cd	NA	NA	< 20	ND < 20	ND
Cr	4	3	30	ND < 1	ND < 1
Cs	ND < 50	ND < 50	NA	ND < 50	ND
Cu	P < 1	P < 1	10	ND < 1	ND < 1
Fe	1	1	7	P < 1	P < 1
K	20	15	NA	5	8
Li	15	15	NA	15	P < 1
Mg	P < 1	P < 1	ND < 1	P < 1	P < 1
Mn	ND < 1	ND < 1	10	ND	ND
Ni	ND < 10	ND < 10	20	ND < 10	ND
Rb	ND < 4	ND < 4	ND	ND	ND
Si	1	1	50	5	5
Sn	NA	NA	< 10	ND	ND
Ti	NA	NA	< 10	ND	ND
Tl	ND < 1	ND < 1	ND	ND	ND
Br	NA	200	NA	29	0.35%
F	NA	50		< 10	28
I	NA	NA	< 5	< 5	< 5
O*(2)	NA	520	< 5	< 5	< 5

1. Concentrations in ppm unless specified. P = present, ND = not detected, NA = not analyzed for
2. All oxygen containing impurities

zone refined under an atmosphere of HCl gas according to a procedure developed by Warren.[36] The hydrogen chloride gas aids the removal of bromine and oxygen containing anions by chemical reaction. Removal of the reaction products from the region of the salt is accomplished by condensing them on a cold (-78°C) surface. This zone refined material was then used as the melt from which a crystal was pulled using a Harshaw crystal as a seed. The procedure is outlined below

Zone refining was done in the apparatus shown in Fig. III-1. The furnace tube and sample container are quartz (28 and 24 mm OD respectively). The furnace tube had a quartz-to-pyrex graded seal to the pyrex O-ring joint outside the hot zone. The sample tube was sealed at one end. The joint was sealed with a teflon O-ring and the stopcock between the gas handling system and the furnace tube was of pyrex-teflon construction. Thus, when the stopcock was closed only pyrex, quartz, and teflon are in contact with the corrosive gas. The O-ring joint had to be ground and clamped with flanges instead of the ordinary joint clamp in order to keep it from leaking during the zone refining. The gas handling system was stainless steel, copper and brass. The furnace tube was wound with a coil of nichrome ribbon of approximately 10-ohms resistance. The ribbon was made by rolling 16 gauge nichorme wire to about 2-1/2 mm width. Then the coil was covered by a single layer of asbestos paper (except for a slit the length of the tube which was left uncovered so that the sample could be seen). A 36 mm OD quartz tube was used as an outer jacket in order to keep the asbestos paper in place. The coil was heated by A.C. power from a 220 V. 20A. Variac. No attempt was made to regulate the temperature during the zone refining. The hot zone was formed by a fire

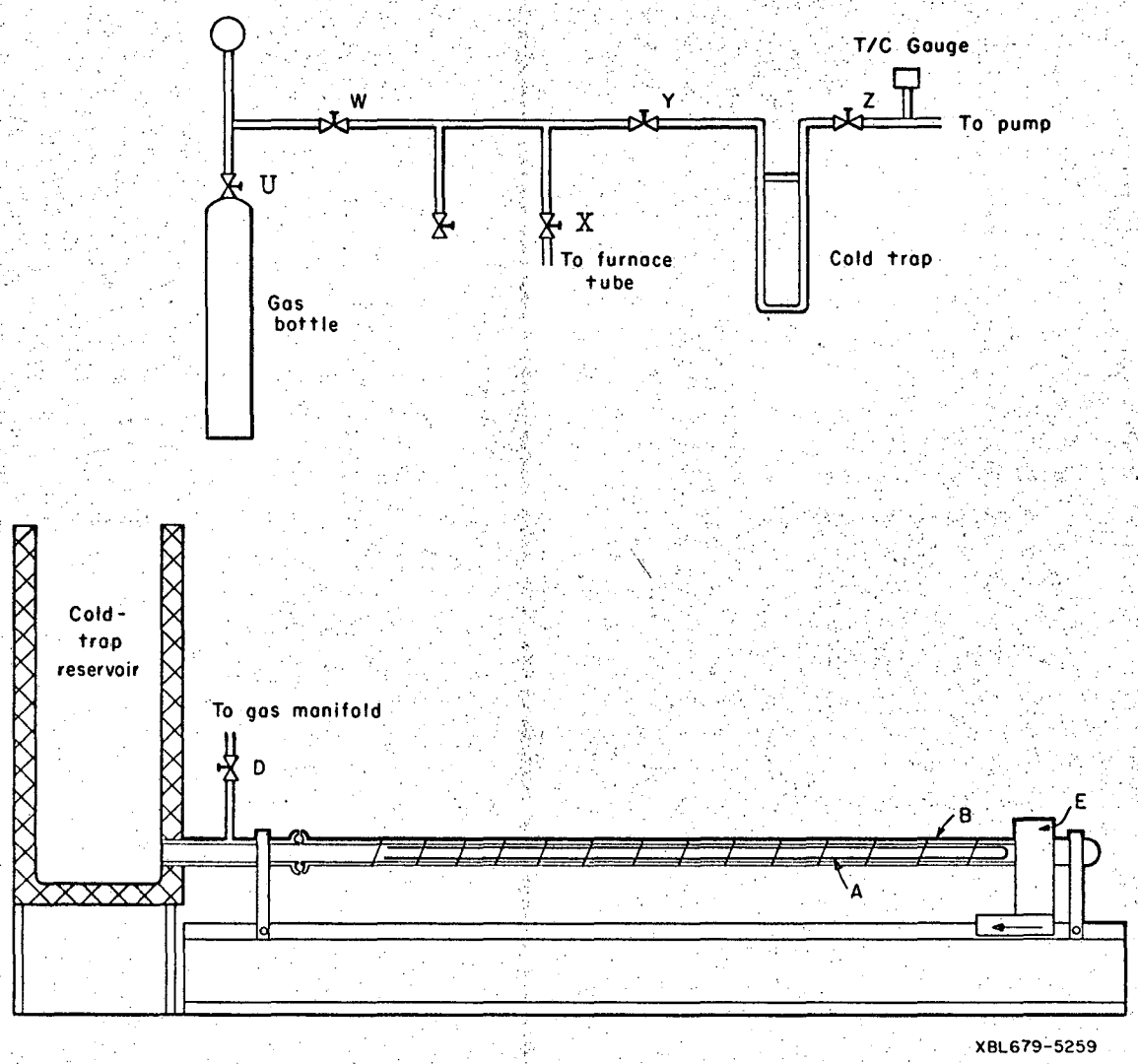

Fig. III-1 Crystal purifying and zone refining system

brick which had a hole in it for the tube to pass through. The brick was mounted on a trolley which was pulled along a track by a wire and a pulley arrangement.

The refining procedure was as follows. The sample tube was filled with reagent grade salt and put in the furnace tube. The O-ring joint was sealed and the system pumped down to less than 10μ with the liquid nitrogen trap (LN trap) cooled and pumped on at this pressure for more than two hr. Valves Z and Y (see Fig. III-1) were closed and 1 atm HCl (commercial grade) was let in through valve U. Valve Y was opened and the HCl condensed into the LN trap. Valve Z was opened and the non-condensable (at 77°K) gases pumped out of the system. The pressure was returned to less than 10μ, then Z was closed and the LN trap warmed until the pressure was about 1/2 atm. Valves Y and X and the stopcock D were closed to isolate the refining chamber from the manifold. The LN trap was chilled and the HCl left in the manifold condensed into it; the trap was removed from the manifold and the gas disposed of in a hood. This procedure removes most of the oxygen and water vapor from the gas. The furnace tube was warmed slowly, with dry ice in the reservoir, until the temperature of the tube reached about 600°C (about 24 hr was used). Quite a bit of ice was formed on the glass wall between the furnace tube and the dry ice reservoir during this heating. A gas change was made at this point. The stopcock and valves X and Y were opened to condense the HCl into the liquid nitrogen trap. Then the dry ice reservoir was emptied and warmed so that the ice formed during the heating was transferred to the LN trap. Valve Z was opened and the system pumped down to less than 10μ. All the valves were closed and the LN trap removed to a hood

and emptied. It was replaced on the manifold and the system pumped down. Then the system was refilled with HCl by the same procedure used for the original filling. The temperature of the furnace tube was increased to 700±30°C and a zone pass was made. It is not necessary to close the end of the sample tube because the zone was stopped before the end of the tube was reached and the unmelted salt kept the melt in the tube. The temperature in the hot zone was not measured, but the molten zone was about 10 cm long. The forward travel speed of the trolley was 0.7 mm/min. After one pass the gas was changed again. Then, six to ten zone passes were made. The last pass was made at about 0.2 mm/min. The furnace tube was cooled slowly to room temperature and the HCl pumped out. The tube was back filled with nitrogen and the sample removed. This material was unsuitable for vaporization studies because it contained bubbles of HCl gas which had been dissolved in the melt. It was also highly strained and had stuck to the tube in several places. This zone refining procedure produced crystals with an order of magnitude lower bromine and oxygen impurity content. An analysis of a typical zone refined sample is shown in Table III-I. This material was used as the melt from which the final crystals were pulled.

The apparatus for the crystal pulling is shown in Fig. III-2. The tybe was pyrex. The crucible to hold the melt was platinum and the crucible holder was quartz. The tubes used as seed holders and crucible holder support were stainless steel (Type 304). A chromel-alumel thermocouple passed through a feed-through at the bottom of the support tube to a copper commutator arranged so that the tube could be rotated and the temperature measured simultaneously. The bead of the thermocouple was in contact with the bottom of the crucible. This thermocouple served as the

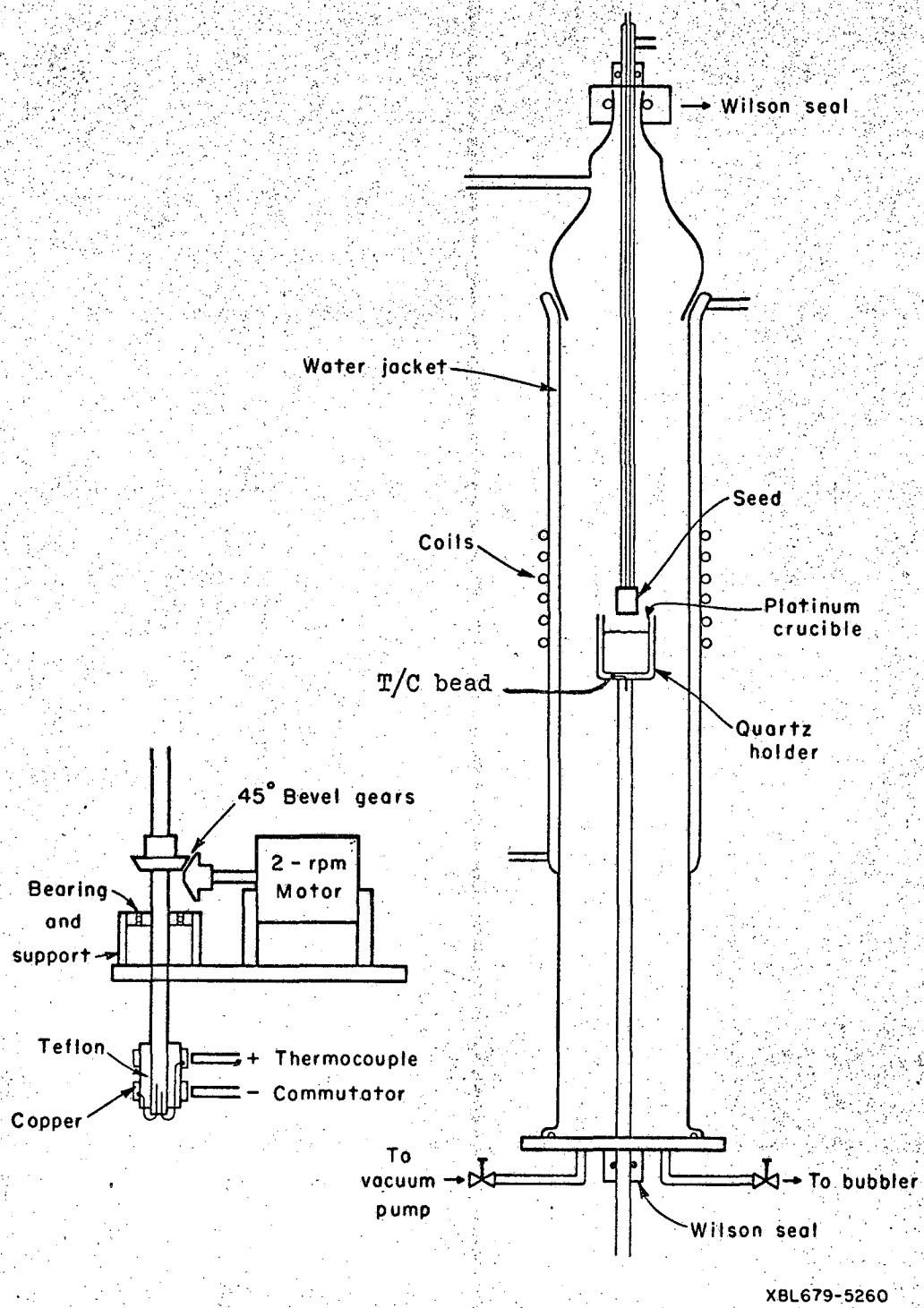

Fig. III-2 Crystal pulling apparatus

sensor for a temperature controller which controlled the R.F. generator heater power level. The seed was attached to the stainless steel tube by a platinum holder and platinum wire through a hole drilled in the seed crystal.

The growing procedure was as follows. The crucible was filled with the zone refined material and a seed attached to the upper tube. The crucible was put in the holder and the upper joint greased and sealed. The system was pumped out with a liquid nitrogen trapped mechanical pump and filled with high purity dry nitrogen gas twice. Then nitrogen was allowed to flow slowly through the system for about an hour. The R-F generator was turned on and the crucible heated to 500°C. It was kept at this temperature for about an hour to drive off any adsorbed water. Then the temperature was raised to 820±20°C to melt the salt. This was done as quickly as possible to minimize the evaporation of the NaCl charge with consequent coating of the pyrex tube growth chamber. Then the cooling air to the upper concentric tubes which held the seed was started and the seed was dipped into the melt. At first the end of the seed melted. The seed-melt interface was watched carefully and the temperature adjusted slightly until no more melting occurred and growth started. Crystal growing continued until about 7 to 8 cm of crystal had grown. The crystals had a rectangular cross-section with rounded corners. The minimum dimension was approximately 1.5 cm. An analysis of one of these crystals is shown in Table III-I (Lot IV). The bromine and oxygen contents are, as expected, appreciably lower than those of the Harshaw samples.

C. Doped Crystals

Sodium chloride crystals were deliberately doped with several

impurities in order to determine whether or not changing the concentrations of these impurities had any effect on the evaporation rate, activation energies for monomer and dimer evaporation, and/or the monomer to dimer ratio.

1) Calcium doped crystals were obtained from Semi-Elements Corporation.[37] These crystals had a reported calcium content of approximately 10^3 ppm. However, the analysis (shown in Table III-I) indicates only 40 ppm mole % of Ca.

2) Oxygen doped samples were prepared by heating 1×1×2 cm pieces of Harshaw NaCl in an oxygen atmosphere at 750±10°C. The oxygen flow rate was 5-10 cc/sec at one atmosphere. Treatment times of 20 hrs to 170 hrs were used. It has been postulated[38] that the oxygen enters the crystal by the following mechanism:

$$O_2 + Na^+Cl^-(s) \rightarrow Na^+O_2^-(s) + 1/2\ Cl_2$$

Kanzig[38] and Kanzig and Cohen[39] have shown that in oxygen doped KCl crystals there is a paramagnetic impurity center on a chlorine site in the lattice at a concentration of ~ 10^{15}/cc. They assigned this impurity as O_2^- oriented so that the O-O axis is in a (110) crystal direction. It is reasonable to assume that oxygen behaves similarly in sodium chloride.

3) A bromine doped crystal was grown by the same Kyropoulos method that was used to grow the pure sodium chloride crystals. The starting sodium chloride charge was not zone-refined. Sodium bromide analytical reagent grade granular crystals were used to provide the bromine content. The salts were mixed and then melted under a nitrogen atmosphere in a platinum crucible. The crystals were grown using Harshaw crystals as seeds. The crystal used in the experiments was grown from a melt containing

0.5 mole percent sodium bromide. The analysis of the crystal is shown in Table III-I.

D. X-Ray Irradiated Crystals

X-ray irradiated crystals were prepared by exposing a Harshaw crystal to unfiltered x-ray radiation from a tungsten target (operated at 20 ma cathode current and 50 KV) for 1.5 hr. After treatment the crystal had the typical yellow color characteristic of sodium chloride crystals containing F centers (electrons trapped at chloride ion vacancies). After the crystals had been left at room temperature for 16 hours the crystal had a bluish color. The color change is believed to be due to the migration and aggregation of the excess sodium into aggregates of colloidal size. The irradiated sample was colorless when it was removed from the mass spectrometer after the evaporation experiment. No detectable absorption bands were found in the range 8,000 A to 3,000 A. It is apparent from this change that the excess sodium must diffuse rapidly out of the lattice at the evaporation temperature.[40]

E. Strained Single Crystals

Straining a sodium chloride single crystal beyond its plastic yield point introduces dislocations into the lattice.[42] The purpose of this treatment was to study the effect of dislocations on the vaporization phenomena of NaCl. Strained crystals were prepared by a) compressing the crystal beyond its plastic yield point (Fig. IIIa), or b) bending the crystal (Fig. III-b).[41,42]

The crystal bending had to be done under water to keep surface cracks from propagating and the crystal from breaking under load. Compressive loading proved to be a more reliable and a more easily controlled

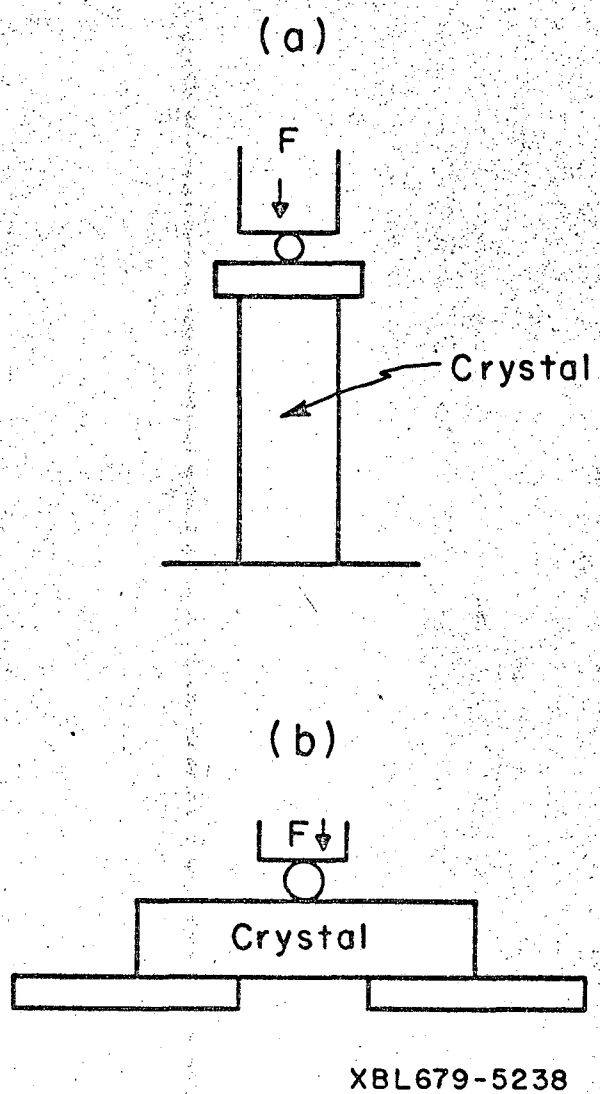

Fig. III-3(a) Schematic of compressive straining apparatus
(b) Schematic of bending apparatus

method of introducing dislocations into the lattice. The dislocations introduced by compressive loading were not uniformly distributed throughout the lattice. They tended to appear in "slip bands" between which were areas of lower dislocation density. A discussion of the mechanisms by which dislocations may be generated and move in a lattice may be found in the literature[43] or in several textbooks.[42,44]

After deformation the surface of the crystal was mechanically polished then chemically polished in a 50% ethanol-50% water solution. They were then etched to develop etch pits at dislocation terminations on the surface.[42,45] The etching solution used was 0.3g $HgCl_2$ in 1,000 cc absolute ethanol.[45] This was prepared as a stock solution of 0.3g $HgCl_2$ in 100 cc ethanol then diluted 10:1 for use. In order to get the proper etching action the solution had to be freshly prepared. The crystals were etched 2 minutes then rinsed in absolute ethanol. Photomicrographs were taken on a Zeiss Metallographic microscope using obliquely incident reflected light. If there was a large variation in the number of etch pits on a surface, several areas were photographed and the results averaged. This was the case for the deformed crystals. The unstrained Harshaw crystals had a fairly uniform etch pit density and in most cases only a single picture was taken. Etch pit counts for several crystals prepared under different conditions are given in Table III-II and a typical micrograph in Fig. III-4.

Table III-II Etch pit counts on NaCl crystals

Crystal	Preparation	Etch pit count (no./cm^2)
I 1(100)	As received	16×10^6
I 2(100)	As received	1×10^6
I 5(100)	Annealed in vac	$.8\times10^6$
I 6(100)	Oxygen doped	3×10^6
II 2(100)	As received	$< 1\times10^6$
II 56	Bent	4×10^6
II 58	Annealed	2×10^6
II 59	8 kg/cm^2 load	4×10^6
II 59	After annealing	3×10^6
II 60	10 kg/cm^2 cycled	6×10^6
II 62	>20 kg/cm^2	15×10^6
III 1	M^{++} doped	4×10^6
IV 19	As grown	2×10^6
V 21	Br doped/as grown	1×10^6

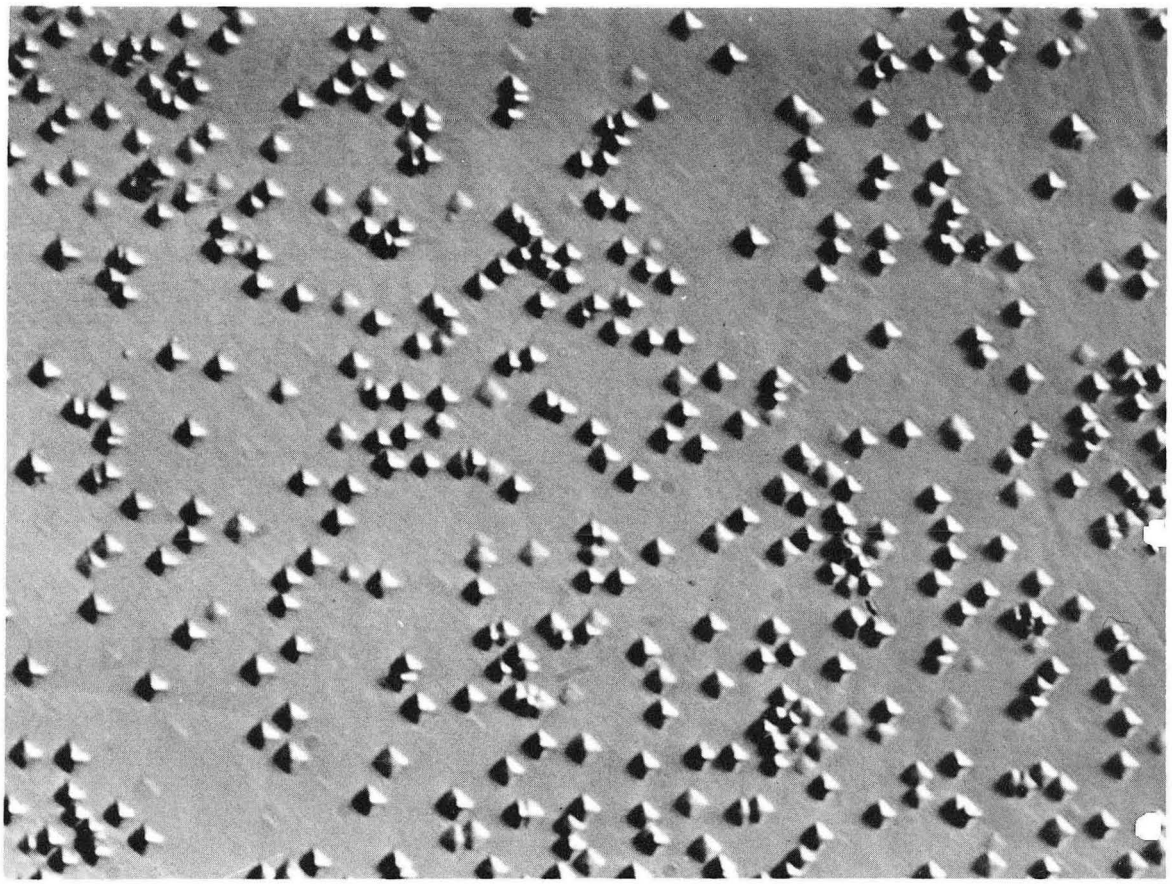

XBB 670-6196

Fig. III-4 Etch pit micrograph of sample 15 (100) A.
× 1000

IV. EXPERIMENTAL APPARATUS AND PROCEDURES

One of the basic experimental problems in this research is to determine the rate of evaporation into vacuum of each of the vapor species from a sample at a known temperature. A vacuum balance combined with proper sample area measurements and temperature measurements can be used to determine the total vaporization rate of the sample; however, it yields no information about the vapor composition. A mass spectrometer can determine the vapor composition; however, it must be calibrated in order to obtain absolute vaporization data. Both of these detection methods were used in this research since their results are complementary.

A. General Apparatus Design Considerations

There are three basic design considerations which must be applied to vacuum vaporization:

1) Minimization of the effect of the ambient environment on the sample,

2) Reduction of the flux of vaporizing molecules back onto the sample to as low a level as possible,

3) Supply of a heat source of geometry and power such that the surface temperature of the sample is closely approximated by the bulk temperature of the sample.

1). The first condition implies that there should be no materials in contact with the sample which could alter any of its chemical or physical properties. First, the sample holder should be unreactive to the sample material and second the background gas should not contain any components at pressures sufficient to effect the sample. It has been

noted by several people[11,52] that diffusion pump oil molecules on the surface of a sample may drastically impede the vaporization processes. A pressure of 10^{-6} torr is sufficient to create a monolayer of adsorbed species per second, if all the impinging molecules stick.

The sample holders in this research were made of platinum and/or high density graphite. These materials are thermodynamically inert toward NaCl. We maintained the background pressure such that the background flux striking the sample was at least an order of magnitude below the evaporation flux of sample material.

2) It is possible to rigorously evaluate the fraction of the vaporization flux which will return to the vaporizing surface in certain geometrical shapes.[46] It is necessary to assume some form for the condensation coefficient of the molecules on the walls. In our case we are only interested in the order of magnitude of the returning flux, so a much less rigorous calculation will suffice. Consider the geometry shown in Fig. IV-1. The sample is vaporizing only from the surface S. Then assume that, instead of coming from the sample, an equivalent flux is evenly distributed across the tube in the plane of S. That is, assume that the tube, from S, a length equal to half the length of the furnace (nD), is the orifice of a Knudsen cell and that the pressure is low enough for molecular flow to prevail. Then one can apply the Clausing factor to get the transmission ratio of the tube.

$$J_v W_c = \text{flux out}$$

$$J_v(1-W_c) = \text{returning flux}$$

where $W_c = f(n)$. For $n = 10$; $W_c = 0.2$ and for $n = 5$; $W_c = 0.5$. So that

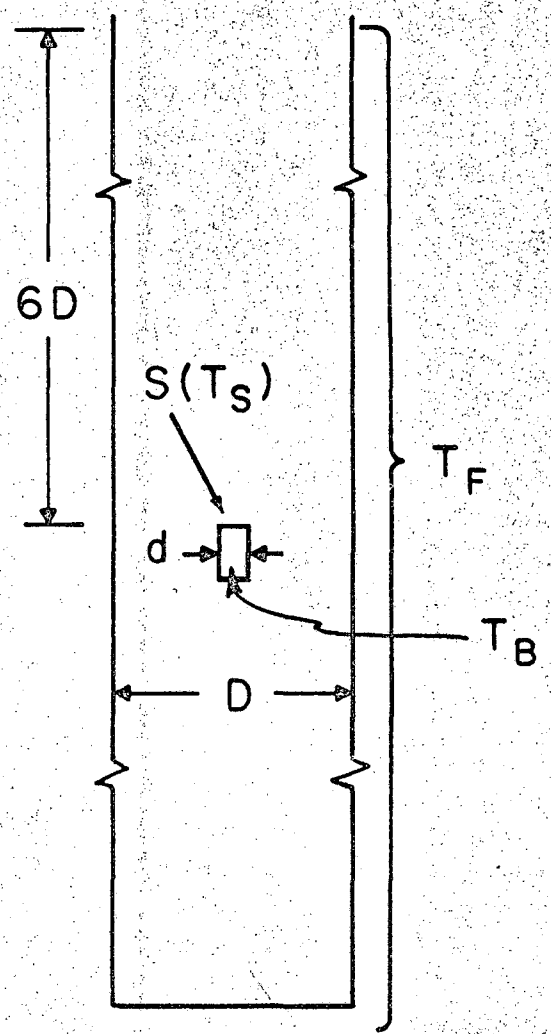

XBL679-5239

Fig. IV-1 Typical furnace and sample geometry

$$J_{ret} \sim .5\ J_v \text{ to } .8\ J_v$$

Now the sample intercepts a fraction of this flux, equal to the ratio of its area to the area of the tube, therefore the fraction of the vaporization flux which returns (eventually) to the sample surface is $\approx d^2/D^2$. Thus, one wants to keep the sample cross section as small as possible with respect to the tube cross section. Problems of maintaining a good temperature gradient in the furnace limit the diameter of the furnace tube to about 1/10 to 1/15 of the length of the furnace. In our case, the sample area was about 0.1 cm^2 and the tube area about 7 cm^2; therefore, the maximum return flux was 0.014 J_v.

3) When the sample vaporizes heat is taken from the solid by the vaporizing molecules. There is also heat loss to cold walls by radiation and conduction loss through the sample supports. Since it is undesirable to put a thermocouple directly on the vaporizing surface temperature with a temperature measured elsewhere on the sample.

Assuming that the heat is supplied to the crystal by radiation then the power absorbed by the crystal is

$$P_F = \epsilon K_{SB} \left(T_F^{\ 4} - T_B^{\ 4}\right)^* A_s$$

where ϵ is the emissivity of the surface, K_{SB} is the Stefan-Boltzmann constant = 5.6×10^{-5} ergs cm^{-2} sec^{-1} K^{-4}

T_F is the furnace temperature

T_B is the bulk sample temperature

A_s is the surface area of the sample

P_F is the power input from the furnace

P_v is the power loss by vaporization

The heat loss due to vaporization is $P_v = \Delta H_v^* R_v$ where R_v is the rate of vaporization in moles cm^{-2} sec^{-1}. Assuming $\Delta H = 50$ kcal/mole and $R_v = 10^{-6}$ (about an order of magnitude higher than any observed flux) then

$$P_v \cong 2\times10^{-6} \text{ ergs sec}^{-1}$$

If this is the only heat loss then,

$$P_F = P_v = 5.6\times10^{-5}\ \epsilon(T_F^4 - T_B^4) * A_s = 2\times10^6 \text{ ergs sec}^{-1}$$

$$(T_B/T_F) \cong (1-2\times10^{-6}/5.6\times10^{-5}\ \epsilon\ A_s T_F^4)^{1/4}$$

Letting $T_F = 900°K$, $\epsilon = .3$, and $A_s = 1\ cm^2$

$$T_B/T_F \cong .996 \text{ and } T_B = T_F - 4°K$$

Experimentally, by imbedding a thermocouple in the sample, we found $T_B = T_F \cong 6°K$ at this temperature.

To get an estimate of the gradient from the bulk to the evaporating surface assume that the heat flux is incident on a plane, A, 0.5 cm from the vaporizing end. Let $P_v = 2\times10^5$ ergs sec^{-1}; then $P_v = KA_E \cdot 0.5\ (T_A-T_S)$ where K is the thermal conductivity of the vaporizing substance. Let $K = 0.02$ cal sec^{-1} cm^{-1} $°C^{-1}$ then $2\times10^5 \cong 8\times10^5\times.1\ (T_A-T_S)$; $T_A-T_S = .25°C$. Thus, for materials with reasonably high thermal conductivities the surface temperature lowering due to vaporization should be negligible at these vaporization rates.

B. Microbalance System

The microbalance used for the weight loss measurements was made, in part, after a design by Honig and Czandera[47] (Fig. IV-2). Designs of various types of vacuum microbalances and design considerations for the pivotabl null balance which we constructed may be found in the literature.[48] This type of balance had the advantage of being rugged and able to support relatively heavy loads (~ 1-2g) while still having good sensitivity (weight changes as small as 1μg have been detected). The beams are made of 1 mm quartz; the pivot points are 0.10 in. tungsten rods electropolished to a .001 in. radius tip; the end pivots are .003 in. tungsten wire stretched with about a 3 pound load while being attached to the beam. Both the center pivots and the end pivot wires are held in place by epoxy cement of a very low vapor pressure type. The pivots were made co-planar to within ±.0005 in. by using a flat table and precision blocks. First the center pivots were attached so that the three center beams were horizontal and so that the center of gravity of the balance was below the pivot points. If the center of gravity is above the plane of the pivot points then the balance does not have a stable equilibrium position. Also the center beam ends were adjusted so that they were approximately co-planar with the pivots. After the pivots had been cemented and the cement cured, the end pivots were positioned so that all pivot points were co-planar to within ±.0005 in. Then the end pivots were cemented in place. After the whole assembly had been cured at 60°C for 24 hr, the alignment was checked. Fixing the plane by one end pivot and the center pivots, the other end was 0.0005 in. ± .0003 in. above the plane

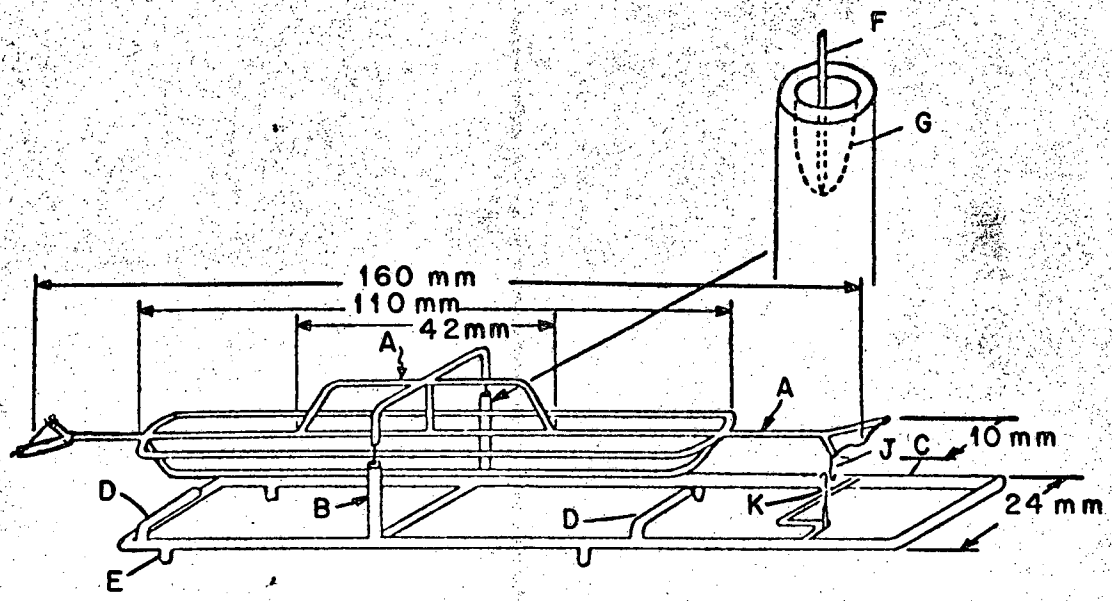

XBL679-5240

Fig. IV-2 Microbalance and support
(from Hoenig and Czandera, Ref. 47)

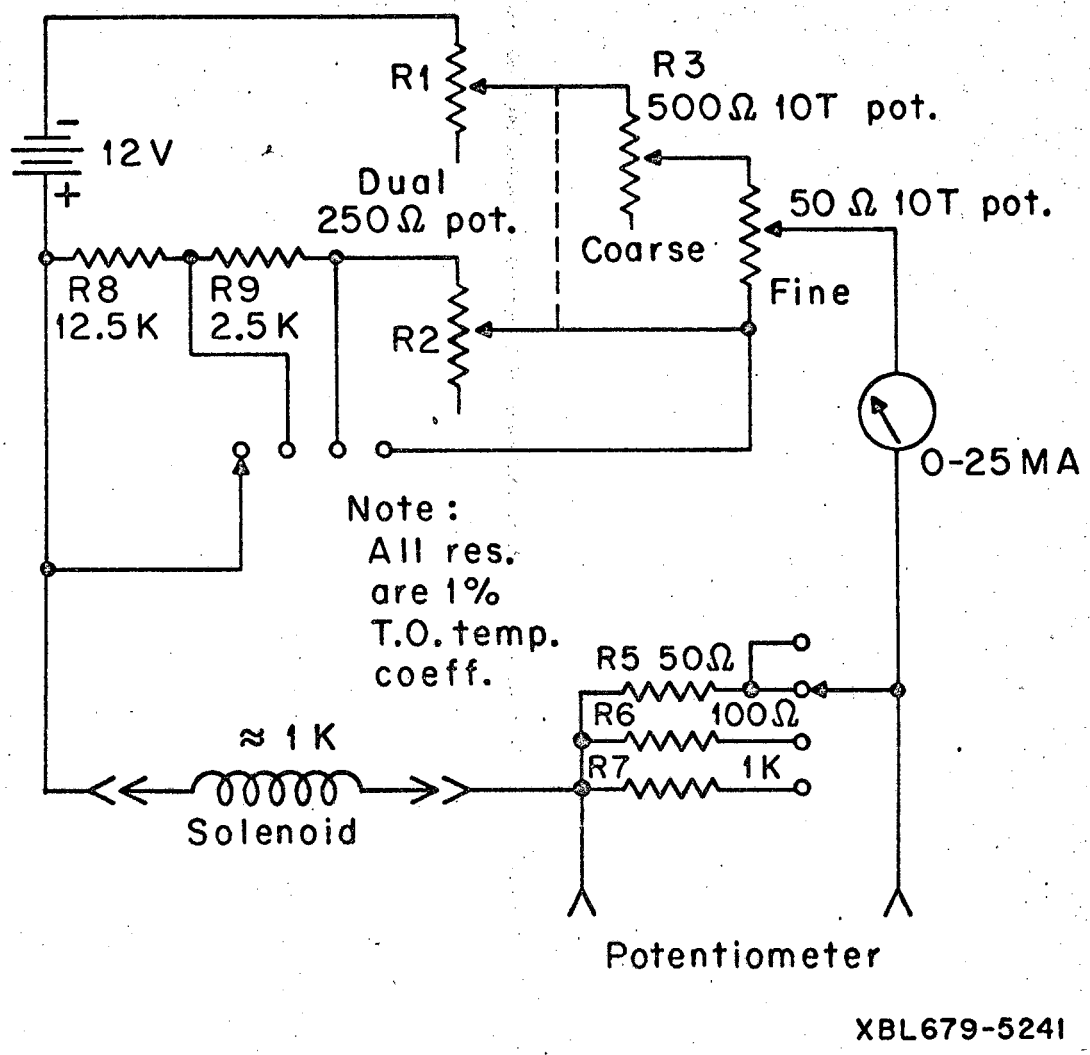

Fig. IV-3 Microbalance solenoid current supply

with no load on the balance. The center pivots were supported by quartz cups having a parabolic cross-section near the bottom. Beam arrests were placed on the balance support frame to limit the motion of the beam to ~2 mm vertical motion at the arrests. This prevented the pivots from hitting the walls of the support cups. A better pivot system can be built using sapphire bearings,[48] but this simple system seemed to perform adequately.

The balance was used as a null device. The restoring force for a change in sample weight was produced by a magnet and solenoid. The magnet was made of two pieces of .020 in. diameter "Cunife" wire 1 in. long sealed in glass. The solenoid was 12,500 turns of No. 34 copper wire wound on a 1/2 in. diameter by 2 in. long form. The magnet was suspended from the balance inside the vacuum while the solenoid was outside the vacuum. The solenoid was positioned so that the top of the magnet was about 5 mm above the tope of the solenoid. This position gave some damping of the balance motion. Solenoid current was provided by the circuit shown in Fig. IV-3. A Leeds and Northrup Millivolt potentiometer was used to measure the voltage drop across the standard resistor.

The balance was mounted on its support frame in a 50 mm pyrex tube as shown in Fig. IV-4. Both magnet and sample were supported by quartz fibers with hooked ends. The rod A in Fig. IV-4 had a hook on its end so that the sample support fiber (and sample) could be lifted off the balance and up about 10 in. This provision allowed the sample to be removed from the hot zone of the furnace when the temperature was changed

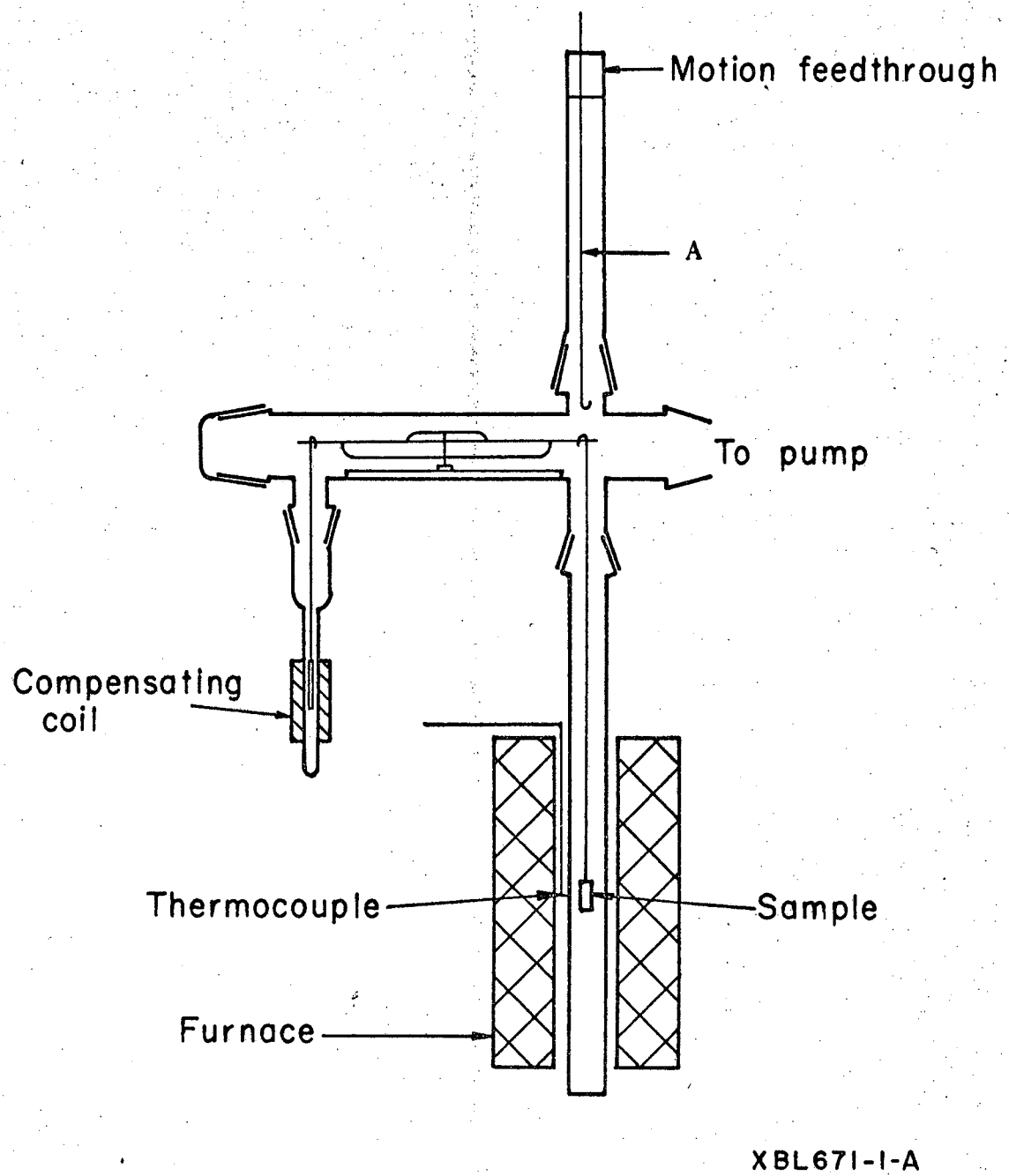

Fig. IV-4 Microbalance system

and while the temperature of the furnace reached a new steady state, thus conserving the sample.

The position of the end of the balance beam with respect to the null point of the balance was determined by observing a fiducial mark on the beam with a 40 power measuring microscope with a micrometer scale eyepiece. The balance could be nulled to ±.005 mm vertical displacement 8 cm from the center pivot which is 6×10^{-5} radians. The null point can be picked arbitrarily since the restoring force, not the deflection of the beam, was used to measure the weight change.

The balance was calibrated using a set of weights which had been weighed on a Mettler Microbalance. These weights were used to increment the weight on the sample side of the balance. All weighings were made with the system pumped down to $P < 10\mu$ pressure. The voltage across the standard resistor was measured. The balance sensitivity is therefore expressed in mv/mg and S is 18.06±.1 mv/mg with the 50-ohm standard resistor. Unbalancing the beam by 1 division (.025 mm) on the microscope scale and using the above sensitivity yields the sensitivity expressed in the usual terms: $\sigma = \Delta\theta/\Delta$ mg where θ is the angle of the beam to the horizontal, thus $\sigma = \Delta\theta/[\Delta mv/s]$. One division on the microscope scale equals 3×10^{-4} radians and is equivalent to Δ mv = 1.59 mv. Therefore, σ = 3.4 milliradians/milligram. Of course, the practical sensitivity is the imbalance needed to cause a unit displacement on the measuring scale which is 0.09 mg/div. The accuracy of any reading is not better than $\sigma \cdot 6\times10^{-5}$ rad. = .02 mg because of the error in locating the null point. A balance calibration plot is shown in Table IV-I.

Table IV-I Balance calibration
(11-3-66)

Added wt. mg	Pot. reading mv	Sens. $\Delta mv/\Delta mg$
0.00	17.70 ± .3 [a]	-
2.292 ± .002	59.01 ± .1	17.94
4.672 ± .002	102.93 ± .1	18.24
10.488 ± .002	206.16 ± .06	17.96
13.208 ± .002	256.29 ± .07	18.06
18.227 ± .002	348.07 ± .1	18.13
	Avg.	18.06 ± .1 mv/mg
1 div of set on mic scale	1.59	0.09

[a] Error estimate is not reading error but variance from reading to reading after balance arrested.

The vacuum system consisted of a NRC chevron baffle trapped 6 in. oil diffusion pump backed by a 5ℓ/sec mechanical pump. The system could be pumped down to 2×10^{-7} torr and all runs were made with the pressure below 2×10^{-6} torr.

The furnace used in these experiments was a Hoskin Chromel wound furnace. The windings were more closely spaced near the ends of the furnace to reduce the temperature gradients at the ends. The temperature profile at the center of the sample tube is shown in Fig. IV-5. The temperature was measured with a Pt-10% Rh/Pt thermocouple having its reference junction in an ice bath. A Rubicon thermocouple potentiometer was used to measure the voltage and the conversion tables published by the National Bureau of Standards were used to convert to temperature readings. Thermocouples were checked at the melting point of lead (327.4) and aluminum (659.7). Any necessary correction was applied to the measured temperature to obtain the actual temperature. In a preliminary experiment a thermocouple was imbedded in a sample and placed in the center of the sample tube. The difference between this thermocouple and one attached to the outside of the sample tube was measured at several temperatures in the range that the vaporization was to be done. These differences are shown in Fig. IV-6. The outer thermocouple was used to determine the temperature of the sample during the actual experiments. The temperature of the furnace was controlled with a Honeywell 7086A temperature controller. The maximum oscillations were about ±3°C at the highest temperatures used. The temperature oscillation period (20 sec) was short compared to the time between weight measurements (> 3 min) so that the effect of the oscillations are averaged out. The exposed area

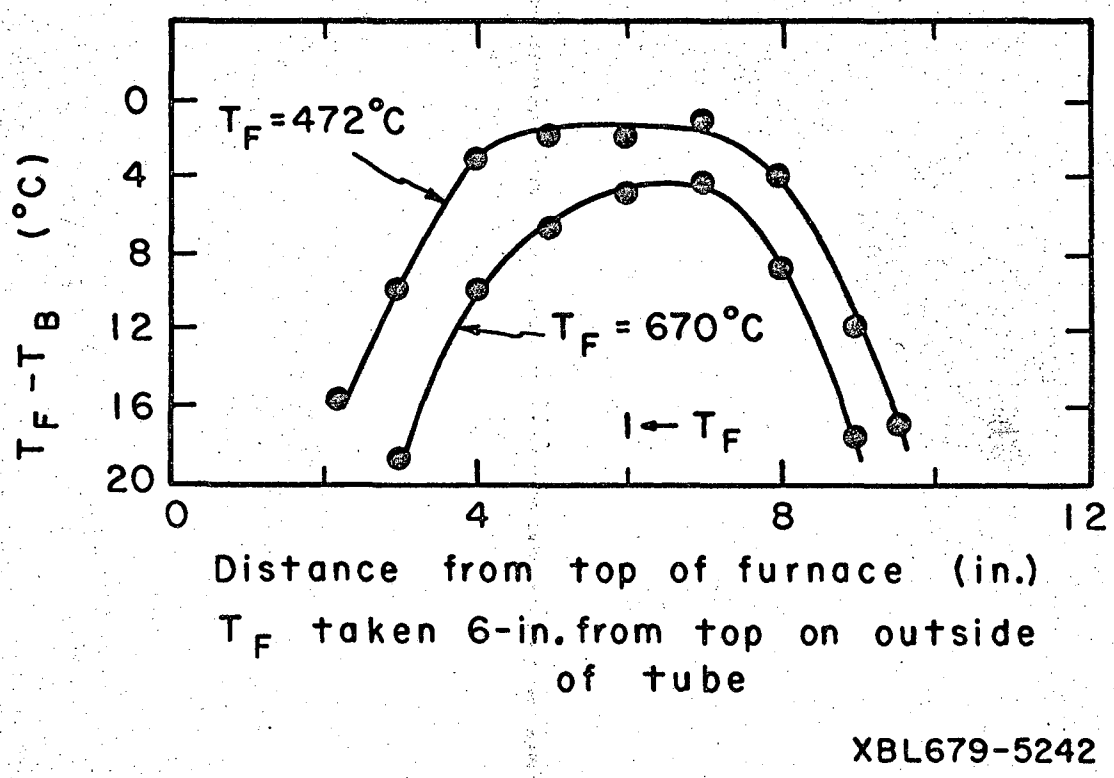

Fig. IV-5 Furnace temperature profile

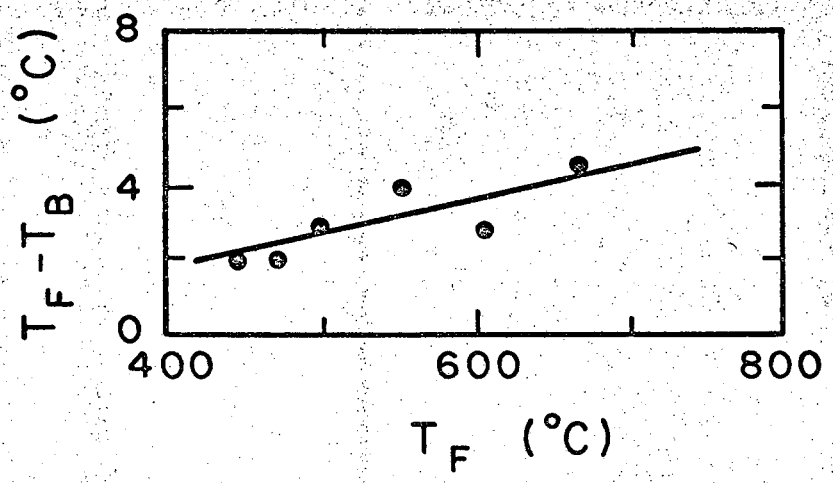

XBL679-5243

Fig. IV-6 Temperature difference between sample and furnace wall

of a sample was measured to $(\pm 0.1\ mm)^2$ before and after a run. This accuracy corresponds to about 3% of the area.

C. Mass Spectrometer System

In order to determine the composition of the vapor coming from the evaporating sample a system containing a mass spectrometer was built. The system is shown in Fig. IV-7. The major parts are 1) the quadrupole mass spectrometer, 2) sample holder, heater, and beam defining slit, and 3) vacuum system.

1) The mass spectrometer is an Electronic Associates, Inc. (EAI) Quadrupole Mass Spectrometer, Model 200.[49] It is shown schematically in Fig. IV-8. The ionizer section is described by EAI as an axial beam ionizer since it is capable of accepting a molecular beam on the axis of the quadrupole. However, it is not used in this configuration in this system. Instead, the molecular beam from the vaporizing sample enters the ionizer perpendicular to the quadrupole axis. Those molecules in the beam that are not ionized continue on their path through the ionizer and strike a cold (20°C) wall of the vacuum system. This orientation of the molecular beam is desirable because the sensitive dynodes of the electron multiplier are not exposed to a high flux of condensable neutral molecules from the beam. The ionizing electrons are produced by a Pierce[50] type filament arrangement. The electron beam is in the shape of a sheet of electrons and it also enters the ionizing region perpendicular to the quadrupole axis. The angle between the velocity vector of the molecular beam and that of the electron beam is about 50 degrees. The ions that are formed by electron impact in the ionizer are then drawn out into the

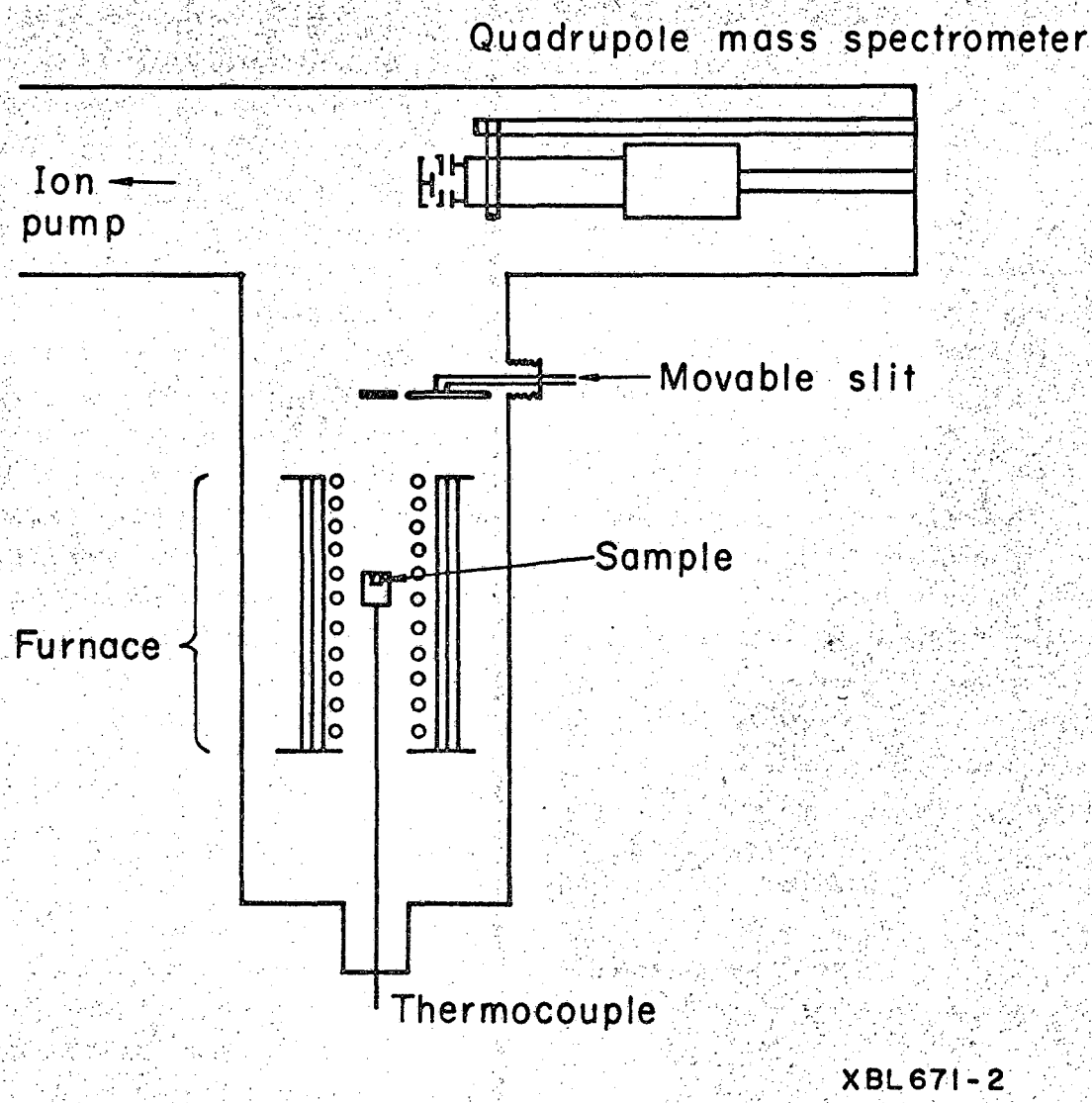

Fig. IV-7 Mass spectrometer system

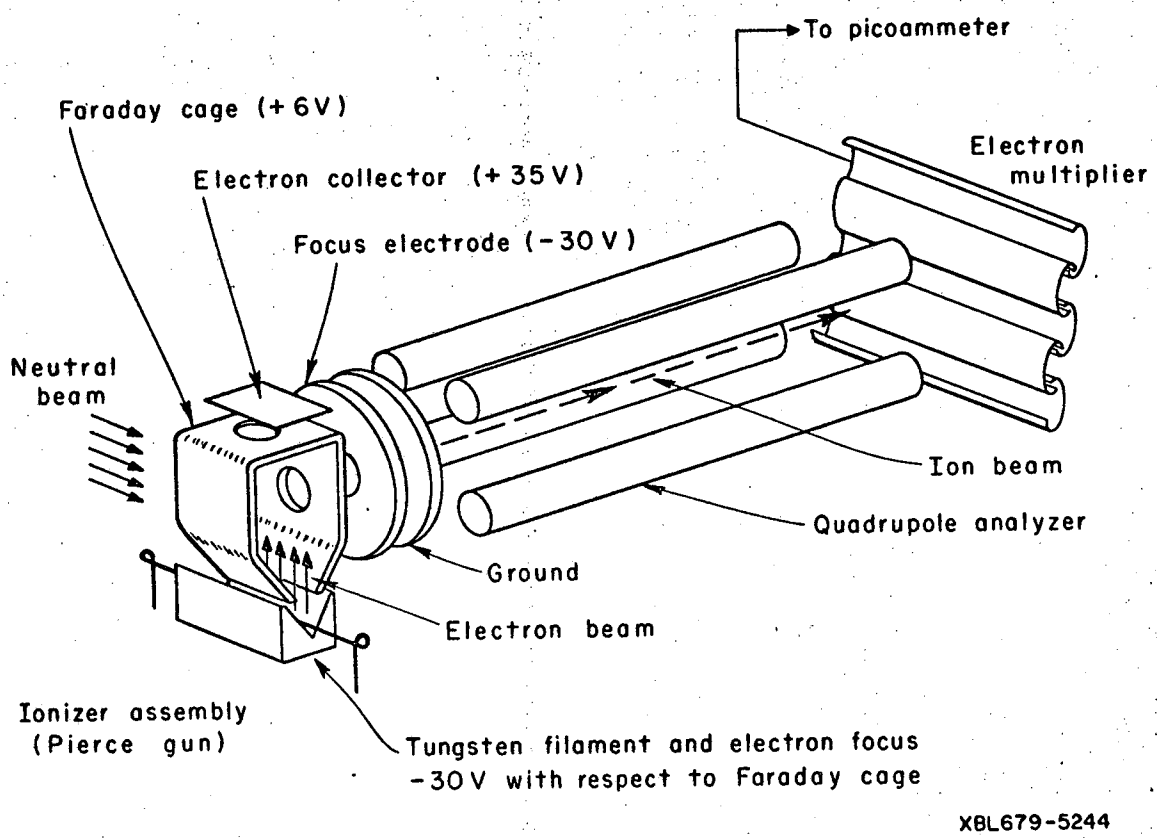

Fig. IV-8 Schematic of quadrupole mass spectrometer

quadrupole analyzer along its axis.

This geometry allows the maximum intersection volume of the molecular beam and electron beam while causing the unionized beam to strike an unimportant surface.

The analyzer section of the mass spectrometer is a set of quadrupole rods. By applying the proper voltages to the rod pairs, (Fig. IV-8), this system can be made to act as a filter: only particles with a given mass to charge ratio (m/e) will have bounded trajectories through the analyzer. The conditions for a stable orbit have been analyzed by Paul[51] and are summarized in Appendix A. The results of the analysis are that the condition for stability is

$$e/m = 0.354\ (r_o^2 w^2)/2V_o$$

thus

$$m = 0.136\ V_o/r_o^2\ f^2$$

where V_o is the R.F. voltage in volts

r_o is the rod spacing in cm

f is the frequency in m.c.

Thus by fixing V_1/V_o and f where V_1 and V_o are the amplitudes of the R.F. + D.C. voltages respectively and f is the R.F. frequency and sweeping V_o one can bring linearly (with voltage) all the masses within a range into a stable orbit. This type of analyzer has the advantage of not needing magnetic fields (thus no hysteresis problem) and rapid scan

rates (10-150 AMU in 50 ms). The scanning capabilities were not utilized in this work. The instrument also has no critical aperture alignment problems and transmits a higher ratio of the ions formed of a given species than does a magnetic deflection machine of equivalent resolution. The disadvantage of this type of analyzer with respect to a magnetic deflection type is that it does not have a fixed transmission ratio as a function of ionic mass. That is, the fraction of ions (of a stable mass) incident upon the analyzer which gets through the analyzer to the detector is dependent on the ion's mass. The cause of this effect is discussed in Appendix A. and a method of calibrating the instrument in order to correct for this transmission ratio is given in Appendix B.

The ions are detected with a 14 stage Cu-Be dynode electron multiplier whose output is measured by either a Keithley 610 B electrometer or 416 Picoammeter. Finally the signal is displayed on a strip-chart recorder. A Vidar data acquisition system has also been used to convert the output signal to digital form. These data, along with other experimental information necessary to data analysis (temperature, etc.), were punched on tape for analysis by a computer.

2) The sample holder and furnace section of the system is shown in more detail in Fig. IV-9. The sample holder is a high density 3/4 in.

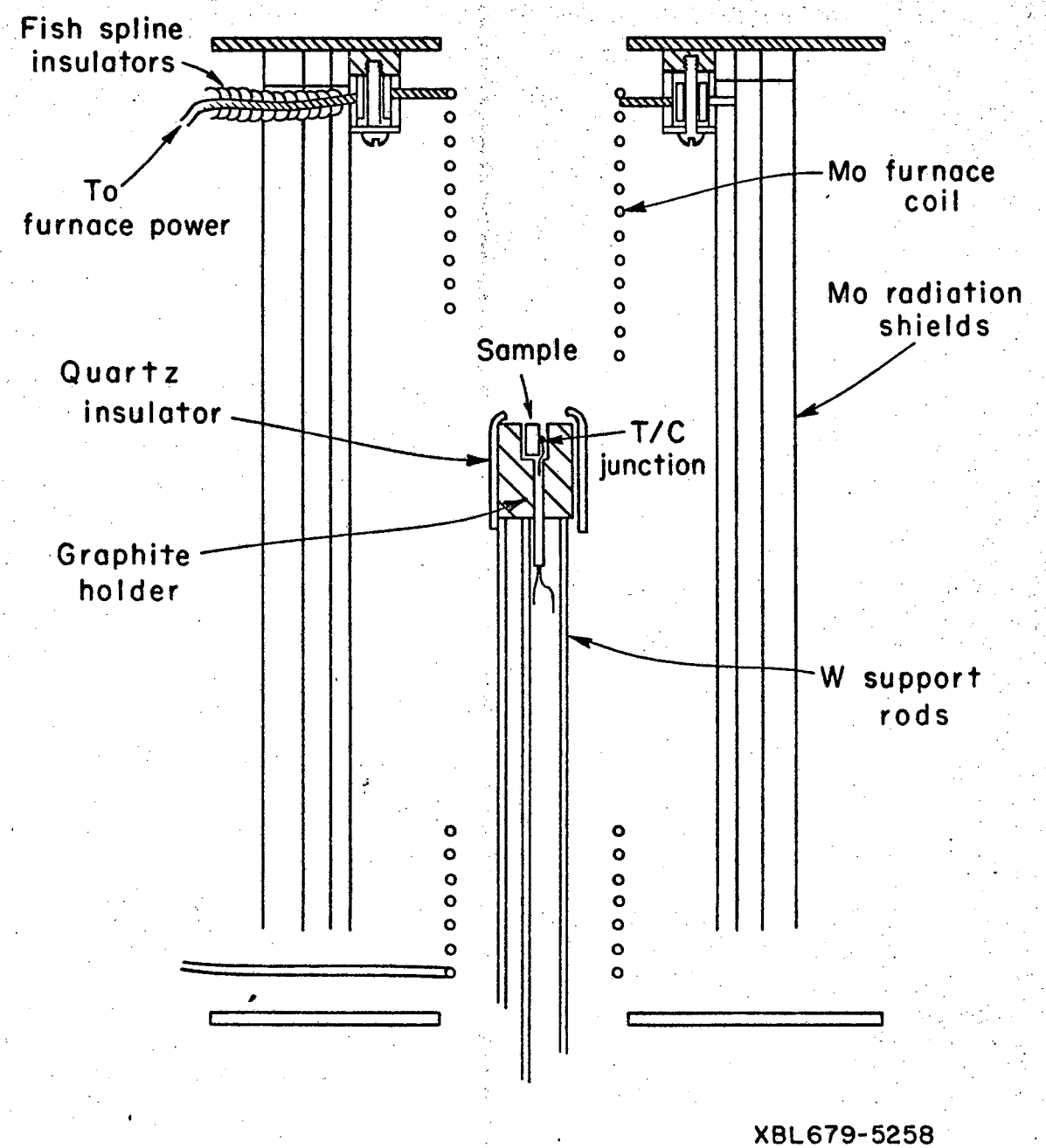

Fig. IV-9 Furnace and sample holder of mass spectrometer system

diameter graphite cylinder with a 1/4 in. diameter by 3/8 in. deep hole in the top. A 3.5×3.5 mm sample wrapped in Pt foil just fits into this hole. The graphite block sits on three tungsten rods. A Pt/Pt-10% Rh thermocouple is held by pressure against the side of the sample. Placement of the thermocouple is not critical as any point in the 1/4 in. hole is within ±1.5°C of the indicated temperature. This thermocouple is passed through the vacuum wall and used for both controlling and reading the temperature of the sample.

The heating furnace was made of a free standing coil of .020 in. molybdenum wire 1 in. in diameter and 8 in. long. The coil was supported at the ends by ceramic supports so that it was electrically insulated from the vacuum chamber. It was surrounded by three concentric .002 in. thick Mo radiation shields. The coil was heated by AC current from the secondary of a 4:1 stepdown transformer. The temperature was controlled by a Honeywell 7086A Controller to better than ±2°C.

There is a slit approximately 10 cm above the sample which defines the size of the molecular beam. It is 3 mm wide and 4 mm long. The slit is movable and connected to a micrometer through a bellows. In its "open" position the slit allows a molecular beam of the size of the crystal surface to pass through to the ionizer region. When the slit is moved to its "closed" position, the ionizer cannot "see" the sample. Thus when the slit is "closed" the flux from the crystal cannot add to the ion current. The flux when the slit is "closed" is taken to be due to the ambient background.

3) The vacuum system was built of 304 stainless steel. Flanges were of the Varian Con Flat type (knife-edge-crushed Cu gasket). Everything

used in the main vacuum chamber has characteristics suitable for obtaining ultra-high vacuum and can be baked to at least 250°C. The system was pumped by a 250 ℓ/s VacIon Pump and rough-pumped by Ultek sorption pumps. Pressure is measured by a Varian "Nude" Ionization Gauge. After baking, the system has a base pressure (furnace off) of less than 10^{-9} torr. After the furnace had been heated to 600°C for an hour the pressure was usually less than 2×10^{-8} torr. When the furnace had been on more than 24 hr the background pressure was generally less than 10^{-8} torr in the sample section.

A gas handling manifold is part of the system. It is pumped by the sorption pumps and has valved connections for three gas sources. There is a gold foil leak between the manifold and the main chamber. A bakeable valve is in the line from the leak to the main system so that the manifold can be completely isolated.

D. Experimental Procedure

1. Crystal Preparation

The Harshaw crystals were prepared for vaporization studies by one of the following techniques:

a) A crystal was cleaved into 5×5×10 mm pieces which were put into a quartz tube. The tube was pumped down to about 2×10^{-6} torr and the section containing the crystals sealed off under vacuum. The tube was then put in a furnace and the crystals annealed at 500°C for 16 to 36 hr. These annealed pieces were then cleaved to yield vaporization samples about 3×3×6 mm to 4×4×6 mm in size. These samples were etched in methanol -10% H_2O and then wrapped in platinum foil so as to expose only one of the ends. These samples were used for microbalance measurements.

b) A crystal was cleaved into sample size (approximately 3x3x6 mm) pieces which were used after methanol -10% H_2O etching for 15 sec. These samples, as all samples, were tightly wrapped in platinum foil so as to leave only one face exposed. This preparation was used for both microbalance and mass-spectrometric measurements.

c) A crystal was cleaved to size, etched in a 50% H_2O-50% ethanol solution for 5-10 seconds, washed in absolute ethanol, and wrapped in foil.

One of the samples used in the mass spectrometer was annealed in dry nitrogen rather than vacuum at 750°C; this sample is labelled II58(100)A. After annealing the rest of the preparation was the same as c) above. All of the doped or Kyropoulos grown samples were simply cleaned, etched in 50% ethanol-50% H_2O and wrapped. Samples for the weight loss experiments were measured before and after the weight loss measurements to ±0.1 mm accuracy.

2. Weight Loss Experiments

A typical microbalance experiment proceeded as follows. The sample was cleaned and wrapped in Pt foil, mounted on the sample support fiber and platinum wire weights added so that about 20 mg of sample could be evaporated. The system was pumped down, usually overnight. The furnace was heated and the temperature allowed to stabilize. The sample was lowered into the furnace and its support fiber gently hooked over the balance pivot wire. Weight loss measurements were taken at this temperature. The sample was pulled out of the hot zone and the temperature changed. After the temperature stabilized the sample was again lowered into the furnace and more weight loss measurements were taken. This procedure was repeated until the allowable weight had vaporized. Then the furnace was cooled,

the sample was removed, the platinum foil trimmed back even with the crystal surface, the sample replaced and sufficient weight added to allow another 20 mg to vaporize. The system was pumped down and more measurements were made.

3. Mass Spectrometer Experiments

Because of the adverse effect of long periods of exposure to the atmosphere on the electron multiplier in the mass spectrometer, this system is kept evacuated even when not in use. The usual schedule followed when changing samples and performing an experiment on this equipment is outlined below.

The furnace must have been off at least 2 hr. The VacIon pump and ionization gauge are turned off. Check the mass spectrometer to see that the filament and all high voltages are off. Fill the sorption pump dewars with liquid nitrogen. Before letting the system up to atmosphere make sure that the valves on both sides of the leak are closed. Attempting to fill the system with one of these valves open will rupture the gold foil. Let the system up to atmosphere with dry nitrogen and leave valve open so that the gas will flow. Loosen the sample flange in order to take out the old sample; slowly, so that the quartz sleeve insulator around the sample holder is not pulled off the sample holder. The flange must be supported while the sample is changed so that the T/C feedthroughs are not disturbed. A piece of 2-1/2 in. pipe does nicely. Change samples, making sure that the thermocouple junction is touching the sample and held there. Put the sample flange back in place with a new gasket and tighten it. Release the over pressure of nitrogen that has built up and close the backfilling valve. Open the valve to the first sorption

pump which should have been chilled for at least 20 minutes. It should take about 30 minutes for the system to pump down to less than 50μ. When this or lower pressure is reached, close the first and open the second sorption pump valve. When the system pressure is below 5μ, start the VacIon pump. If the system does not get to 5μ but is less than 10μ and the second pump has been pumping at least 20 minutes, start the VacIon pump anyway. When the pump has fully started, turn it on "protect" and turn on the ionization gauge. When the pressure is below 5×10^{-6} close the bakeable valve between the manifold and the system. Make sure the cooling water to the sample section is disconnected and the tubing drained. Turn on the "bake-out" control and set the furnace controller to about 250°C (Variac at 25). The thermocouple leads must be connected for the furnace controller to go on. After the bake out, preferably while the system is still warm, out-gas the ion gauge and turn on the mass spectrometer filament. Heat the furnace to the desired temperature range. Only after the furnace gets to temperature should the cooling water be connected. This allows a last outgassing of the sample section walls. Turn on the mass spectrometer so that the voltages and oscillator frequency can stabilize. Put ice in the T/C cold junction dewar and connect the extension wires for temperature reading to the feed throughs. The mass spectrometer system-data acquisition system interfacing and an abstract of the program to convert the paper tape to a useful format are given in Appendix C.

During the actual measurements the temperature was set and allowed to come to the set point (~ 15 to 30 minutes after the original heating period) then the intensity of the ion flux was measured for each of the ions of interest with the slit both "open" and "closed" so that background contributions to the signal could be subtracted out. In the case of

sodium chloride, these ions were mass 23 (Na^+), 58 ($NaCl^+$), 81 (Na_2Cl^+). The mass spectrometer had a lower usable limit to the electrometer signal current of about 3×10^{-12} at the anode (collector) of the multiplier. This limit is the current at which the signal to noise ratio is about one. It is set by multiplier noise and photoelectron generation at the first multiplier dynode by the light emitted by the electron emitter filament. Assuming that the multiplier had a gain of 10^5 then this current corresponds to 3×10^{-17} a = 190 ions/sec hitting the dynode of the multiplier. The upper limit of the usable current (10^{-6} a) corresponded to a flux of about 10^{+17} molecules-cm^{-2} sec^{-1} leaving the surface of the sample and is the upper bound of the molecular flow region near the sample. Thus the instrument can be used to measure five orders of magnitude variation in the molecular flux density.

The mass spectrometer was run with the following ionization region parameters: electron energy = 30 eV, emission < 0.2 ma, electron trap voltage = +35 eV, trap current = 50 μa, ion energy = 6 eV, focus voltage = -28 V. For taking the ion appearance potential data the trap voltage was lowered to 10 V so that the electrons would have a narrower energy spread. The resolution of the analyzer was set at 100* so that the mass 81 peak had a negligible contribution from its neighboring peaks. A typical background spectrum is shown in Fig. IV-10. The sodium chloride peaks occur at "windows" in the normal background which is a definite advantage at low fluxes. The background is subtracted from the ion intensity by "closing" the slit and taking only the difference between the open and closed positions as being signal due to molecules which originate from the

---

* Width of 81 peak at 1/2 height, i.e., $m/\Delta m_{1/2}$ at m/e = 81.

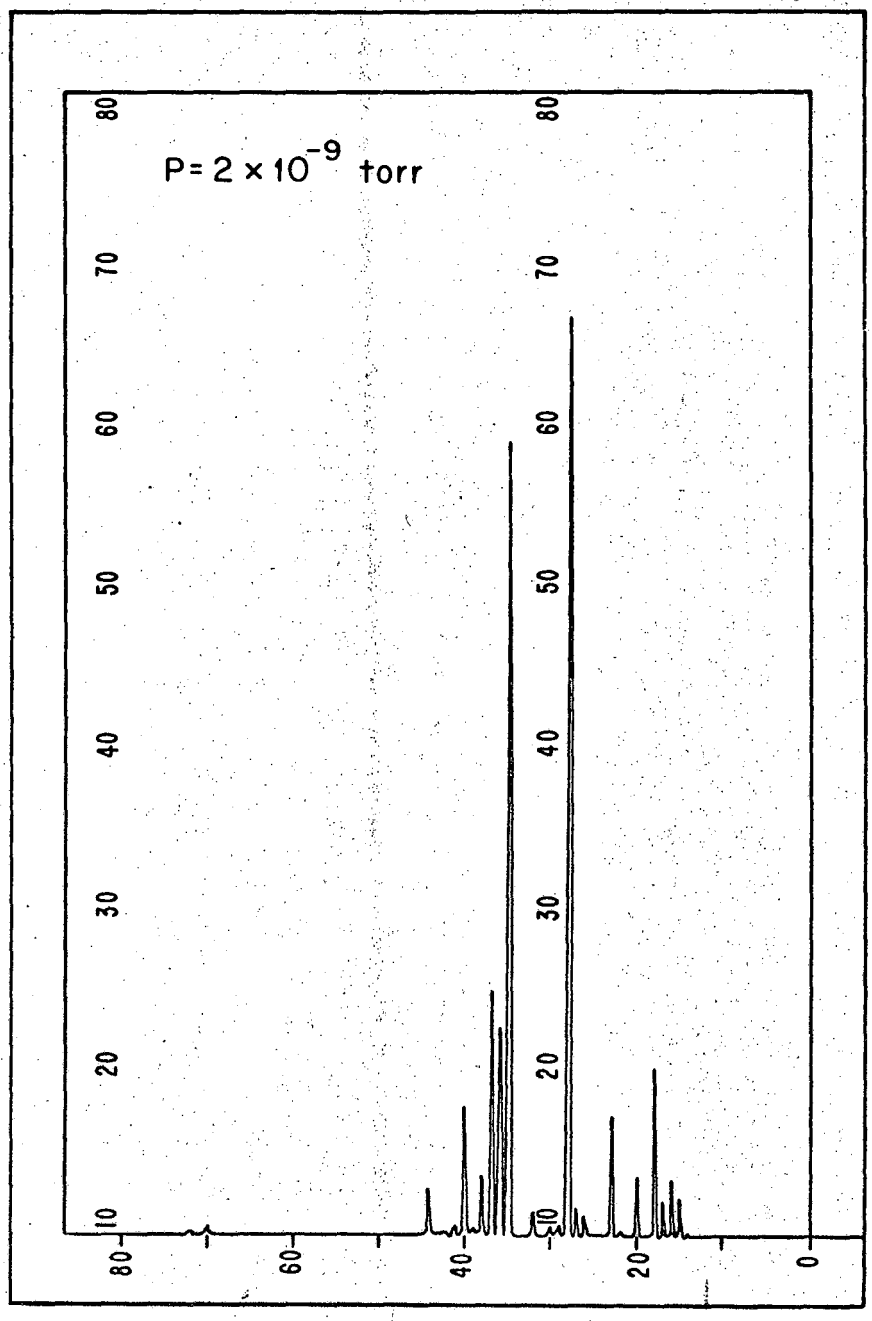

Background spectrum

XBL679-5246

Fig. IV-10. Typical residual gas mass spectrum after bakeout

vaporizing crystal. During a typical experiment measurements are made both while increasing the temperature between intensity measurements and while decreasing. There was no observed difference between the intensities taken going up or down in temperature which could be attributed to lag in the sample responding to temperature changes. In the case of some of the strained crystals differences between intensities taken early in the experiment and those taken later could be found, however, these differences were attributable to changes in the morphology of the crystal surface. Generally about 20 to 30 intensity and temperature measurements to the signal from each ion were made during an experiment.

V. ANALYSIS OF EXPERIMENTAL DATA

A. Microbalance Results

The vacuum balance measurements yield the weight, w, of the sample as a function of time and temperature. The time derivative of the weight, $\dot{w}$, is the rate of weight loss. This time derivative is found from the raw data by taking finite differences. Thus, we have assumed that the rate is constant over the time interval of the measurement. Actually, because of the temperature oscillations the rate oscillates; however, these oscillations are small and their period is short compared to the measurement period, thus they average out.

The rate of vaporization, $\dot{w}$, is divided by the geometrical area of the vaporizing surface to obtain the rate R_v (mg/cm^2 sec). The (100) face samples were cleaved so that all the surfaces are mutually perpendicular, therefore, the dimensions of the exposed face will be constant throughout the experiment. This geometrical surface area was taken as the vaporization area on all of the microbalance samples. This does not mean that we believe that the number of evaporation sites is equal to or directly proportional to the geometrical surface area. The surface of a sample roughens visibly during vaporization as shown in Figs. V-1 and V-2. This roughening produces an unknown increase in the exposed surface. All of the crystals showed similar behavior as far as macroscopic surface topology, thus the geometrical surface area should be an adequate normalization factor. An apparent pressure, P', can be calculated from this rate by use of the Langmuir equation (Eq. II-2)

$$P' = R_v \left(\frac{2\pi RT}{M} \right)^{1/2} \qquad (1)$$

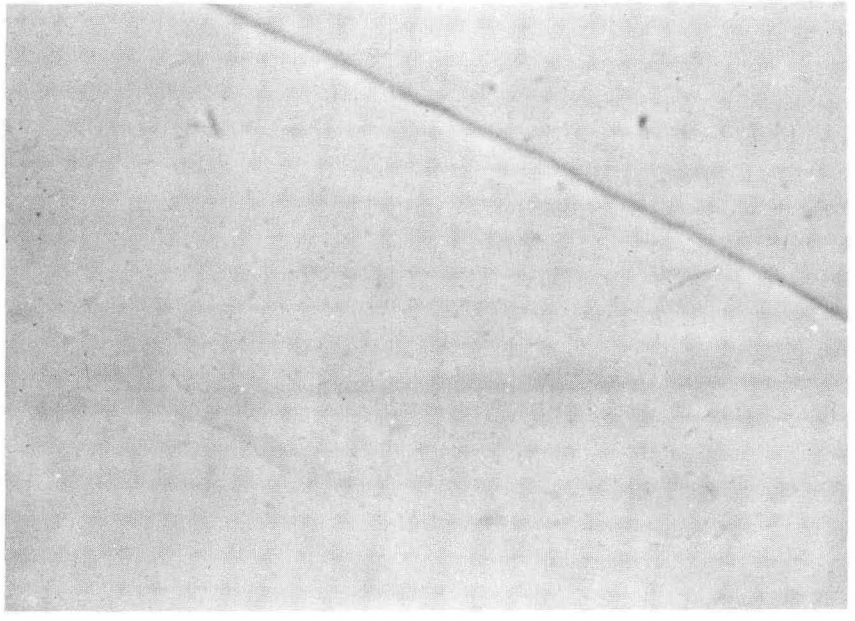

XBB 670-6194

Fig. V-1 Micrograph of typical sample before evaporation ×1000

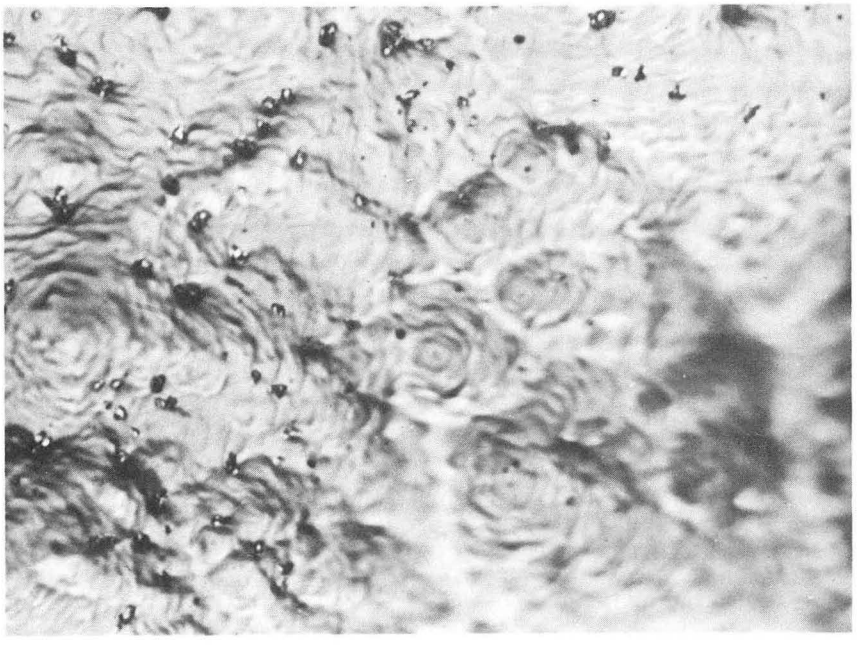

XBB 670-6195

Fig. V-2 Micrograph of typical sample after evaporation × 1000

where M is the molecular weight of the vaporizing material.

$$P'(\text{torr}) = 1.72\times10^{-2}\ R_v(T/M)^{1/2} \qquad (2)$$

In the case of sodium chloride the vapor consists of more than one species[21] (only the monomer (MX) and dimer (M_2X_2) have significant pressures), thus one must use the actual average molecular weight in Eq. (2). The relative fractions of monomer and dimer molecules in the vapor were found to differ from crystal to crystal (Sec. VI), and, in any case have a temperature dependence which is not well known, therefore we have chosen to assume that the vapor consists entirely of monomers and take M = 58.5 g/mol when computing P' by Eq. (2). If the relative abundance of the monomer and dimer in the vaporization flux are known then P'_M and P'_D may be found from P' by

$$P'_M = P'(1 + 2a_2)^{-1} \qquad (3a)$$

$$P'_D = \sqrt{2}\ a_2 P'\ (1 + 2a_2)^{-1} \qquad (3b)$$

where a_2 = the ratio of dimer flux to monomer flux

P'_M = monomer apparent pressure

P'_D = dimer apparent pressure

The rate R_v obeys the Arrhenius expression

$$R_v = Ae^{-E^*_v/RT} \qquad (4)$$

where E^*_v is the activation energy of vaporization. Thus,

$$\log R_v = \log A - E^*_v/RT \ln 10 \qquad (5)$$

Using Eqs. (2) and (5) we have

$$\log P' = \log A + E_v^*/RT \ln 10 + 1/2 \log T + \text{const.}$$

Now,

$$\frac{d \log R_v}{d\, 1/T} = \frac{-E_v^*}{R \ln 10} \qquad (6)$$

therefore,

$$\frac{d \log P'}{d\, 1/T} = \frac{-E_v^*}{R \ln 10} - T/2 \qquad (7)$$

Within the accuracy of our experiments (since $E_v^* \sim 50{,}000$ cal and $T \sim 800°K$) one may assume that

$$\frac{d \log P'}{d\, 1/T} \cong \frac{-E_v^*}{R \ln 10} \qquad (8)$$

B. Mass Spectrometric Data

The mass spectrometer ion currents cannot be directly converted to molecular fluxes because the ion peaks may have several molecular precursors.[53] Also, because of instrumental problems, the mass spectrometer was not calibrated to yield absolute ionic or molecular fluxes. However the various ion currents may conveniently be used to obtain the vapor composition and activation energies of each of the vapor components.

The ion peaks which were observed in the NaCl mass spectrum were m/e = 23, 58, 60, 81, 83.

$$Na^+ = 23$$
$$NaCl^+ = 58, 60$$
$$Na_2Cl^+ = 81, 83$$

The chlorine containing peaks have the proper chlorine isotope ratio. Berkowitz and Chupka[54] reported a $Na_3Cl_2^+$ ion in the spectrum of NaCl

vapor from a Knudsen cell, but its intensity was less than 1% of the $NaCl^+$ ion at the highest temperature used. In the case of NaCl the 23, 58, and 81, peaks were measured for temperature dependence and vapor composition studies.

Electron impact could fragment the vapor molecules of the alkali halides in several ways. For example, in the case of the dimer:

$$M_2X_2 + e^- \rightarrow M_2X^+ + X^\circ + 2e^-$$

$$M_2X_2 + e^- \rightarrow M_2X^+ + X^- + 2e^-$$

$$M_2X_2 + e^- \rightarrow MX^+ + MX^\circ + 2e^-$$

$$M_2X_2 + e^- \rightarrow M^+ + MX + X^\circ + 2e^-$$

and the monomer:

$$MX + e^- \rightarrow MX^+ + 2e^-$$

$$MX + e^- \rightarrow M^+ + X^\circ + 2e^-$$

Thus the dimer could contribute to both the MX^+ and M^+ peak as well as the M_2X^+ peak. If this fragmentation can be suppressed by using low energy electrons then one can separate out the ion intensity due to each parent molecule. The ion currents as a function of electron energy (appearance potential plots) for sodium chloride are shown in Fig. V-1 for low electron energies. As can be seen there are no definite changes of slope in the curves which would indicate the onset of some high energy fragmentation process. The appearance potentials for all three of the ions are similar. Therefore, nothing is to be gained by using low energy ionizing electrons. It would be impossible to work at electron energies low enough to eliminate the fragmentation because of instrumental limitations.

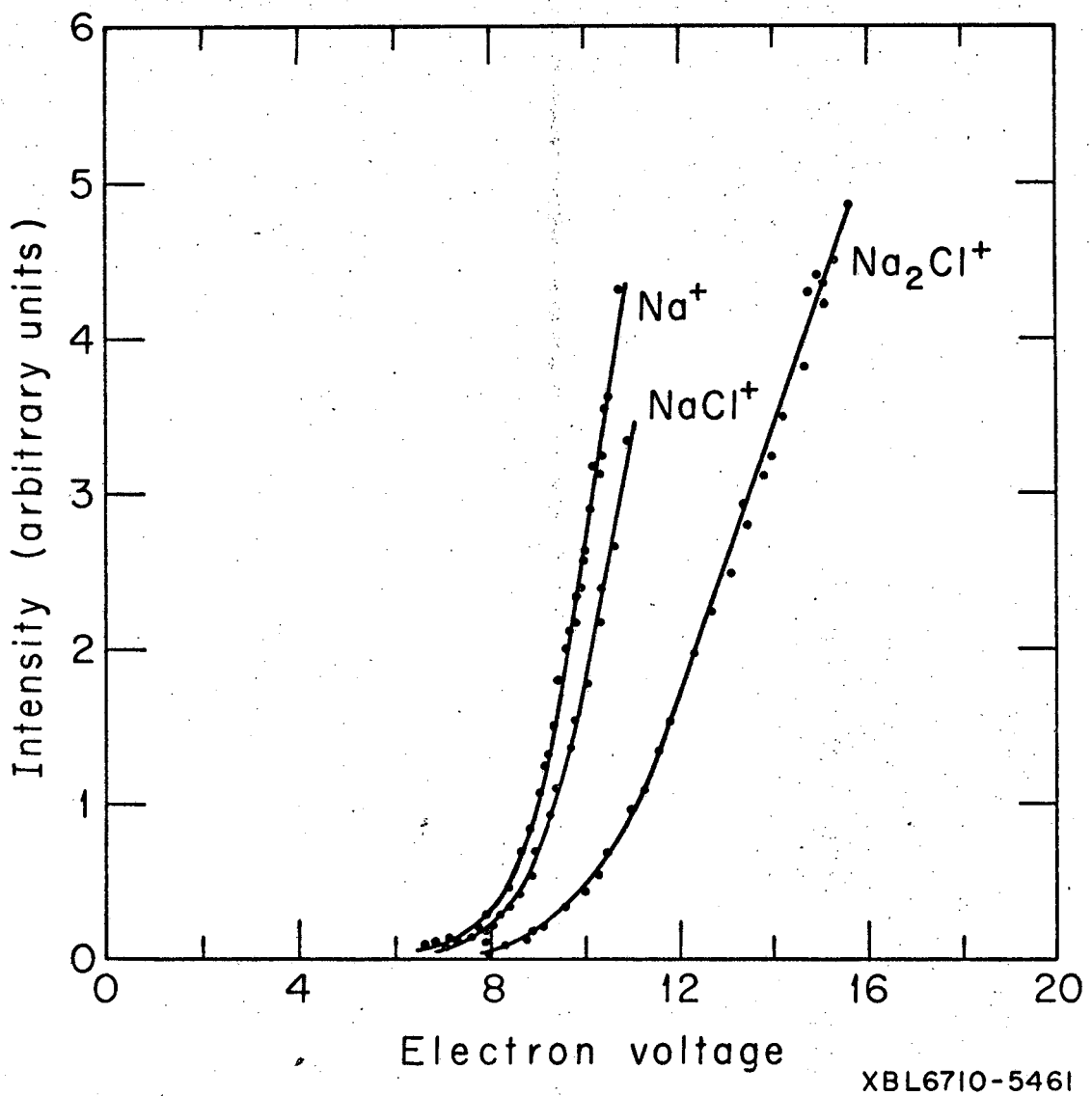

Fig. V-3 Appearance potential plot of NaCl ions

The lowest practical electron energy in our mass spectrometer is about 15 ev. The actual experiments were run at 30 ev electron energy. Fortunately, Gorokhov, et al.[55,56] have devised a way of determining the contribution of the dimer to each of the lower mass peaks by use of a double oven effusion source for the vaporization of sodium chloride in their mass spectrometer. The ion efficiency curves for the sodium chloride ions are given in Fig. V-5. Their results are expressed by the following equations:

$$a_{k\ell} = I_{k\ell}/I_{\ell\ell}$$

where $I_{k\ell}$ is the contribution of the ℓth molecule to the kth ion current. I_k (k = 0,1,2 refers to M^+, MX^+, and M_2X^+, respectively). The results with 70 ev electrons for sodium chloride were: $a_{01} = 2.35 \pm 0.08$; $a_{02} = 0.24 \pm 0.12$; and $a_{12} = 0.17 \pm 0.04$. Thus,

$$I_{01} = I_0 - a_{02}I_2,$$

$$I_{11} = I_1 - a_{12}I_2,$$

$$I_{22} = I_2$$

neglecting the trimer concentration entirely. The Na_2Cl^+ (dimer) ion current is less than 50% of the monomer current thus contribution of the dimer to the mass 58 peak is less than 10%. The mass 81 peak is assumed to be due entirely to the dimer.

The ion intensities given in the next section are the experimental ion intensities. They have not been corrected for any instrumental or other factors except for isotope ratios.

The ion current due to a molecular species may be related to the

apparent pressure of the species in the beam by

$$P_i' = k_i I_i T \tag{9}$$

where P_i' = the apparent pressure

I_i = ion current of the ith ion ($i = 1 = M^+$, $i = 2 = MX^+$, $i = 3 = M_2X^+$)

k_i = constant dependent on geometry and species but not on P_i or T.

Thus

$$\frac{d \log P_i'}{d\ 1/T} = - \frac{E_i^*}{R \ln 10} \frac{d \log IT}{d\ 1/T} \tag{10}$$

The mass spectrometer data were analyzed by use of this equation. A least squares best fit equation of the form $\log I_i T = A_i + B_i(T)$ was fit to the data (see Appendix B for details of program) and $E_i^* = R\ B_i \ln 10$ computed. Since the fragmentation of the dimer molecules contribute to the monomer ions the computed monomer activation energy (E_1^* or E_2^*) is displaced from its real value. This error can be calculated from

$$IT = I_1 T + a_{12} I_2 T \tag{11}$$

Let

$$I_1 T = A_1 e^{-E_1^*/RT}$$

$$I_2 T = A_2 e^{-E_2^*/RT}$$

then

$$-\frac{E^*_{meas}}{R} = \frac{d \ln IT}{d\, 1/T} = \frac{d \ln (I_1T + a_{12}I_2T)}{d\, 1/T}$$

$$= \frac{\left(1 + a_{12}\, A_2/A_1\, E^*_2/E^*_1\, e^{-(E^*_2-E^*_1)/RT}\right)}{\left(1 + a_{12}\, A_2/A_1\, e^{-(E^*_2-E^*_1)/RT}\right)} \qquad (12)$$

For sodium chloride choosing representative values from our experimental results $a_{12} \sim .2$, $A_2/A_1 \sim 100$, $E_2 \sim 62$ kcal, $E_1 \sim 53$ kcal.

$$\frac{E^*_{meas}}{R} = \frac{E^*_1}{R}\,(1.01)\,. \qquad (13)$$

This means E^*_1 is approximately 0.5 kcal higher than E_1. This is of the order of the experimental error but will be subtracted from the computed values of E^*_1 to obtain the tabulated values of E^*_1 in the next section. Error estimates in activation energies reported are taken as the greater of $1/2(E^*_{23} - E^*_{58})$ or the standard deviation of the computed slopes.

Monomer-dimer ratios are computed from the ion current ratios by using the relative ionization cross-section which fit the equilibrium data (see Appendix B). Following his proposal the monomer current for NaCl is taken as $I_{23} + I_{58} + I_{60}$. Let

$$\frac{I_M}{I_D} = \frac{I_{23} + I_{58} + I_{60}}{I_{81} + I_{83}} \qquad (14)$$

then the monomer to dimer ration, M/D, is given by

$$\frac{M}{D} = \frac{I_M}{I_D} \frac{\sigma_D}{\sigma_M} \frac{\tau_D}{\tau_M} \tag{15}$$

where σ_D and σ_M are ionization cross-sections and τ_D and τ_M are transmission probabilities for the ions through the analyzer. (See Appendix B for an evaluation of $\frac{\tau_D \sigma_D}{\tau_M \sigma_M}$.)

VI. EXPERIMENTAL RESULTS

A. Sample Identification

The sample identifying numbers may be deciphered as follows: Sample II 60 (hkℓ) A implies that this sample came from Lot II, crystal 60. It was cleaved to an orientation such that vaporization took place from a nominally (hkℓ) surface. The final symbol, A, designates the particular sample, if more than one sample were cut from a crystal. If this symbol contains an S it indicates that the crystal was deliberately strained to introduce dislocations. The lot identification numbers are given in Table VI-1.

Table VI-1 Correlation of lot numbers with crystal source

Lot	Description
I	Harshaw NaCl
II	Harshaw NaCl
III	Semi-Elements Ca Doped NaCl
IV	Zone Refined and Pulled NaCl
V	NaBr Doped NaCl

B. Total Evaporation Rates of Several NaCl Crystals (Microbalance Studies)

The total evaporation rate data for the (100) face of several NaCl samples taken from crystals I1 and I2 are given in Table VI-2. The etch pit count on crystal I1 was $15\times10^6/cm^2$ and on crystal I2 was $1\times10^6/cm^2$.

Table VI-II

Total evaporation rates for NaCl samples I1(100)A-F.

Sample	T[a] (°K 6)	1/T (°K^{-1})	Rate (mg/cm^{2}sec)	p'[b] (torr)
I1(100)A	899	1.112	$4.7\pm.1\times10^{-2}$	3.21×10^{-3}
	865	1.156	$1.67\pm.05\times10^{-2}$	1.10×10^{-3}
	851	1.175	$1.04\pm.05\times10^{-2}$	6.84×10^{-4}
	833	1.200	$5.0\pm.15\times10^{-3}$	3.26×10^{-4}
	821	1.218	$4.1\pm.15\times10^{-3}$	2.62×10^{-4}
I1(100)B	847	1.181	$8.2\pm.1\times10^{-3}$	5.37×10^{-4}
	866	1.155	$1.56\pm.1\times10^{-2}$	1.00×10^{-3}
	865	1.156	$1.42\pm.1\times10^{-2}$	9.15×10^{-4}
	867	1.131	$2.3\pm.06\times10^{-2}$	1.54×10^{-3}
	884	1.131	$2.3\pm.06\times10^{-2}$	1.54×10^{-3}
	824	1.214	$2.7\pm.1\times10^{-2}$	1.75×10^{-4}
	892	1.121	$2.1\pm.07\times10^{-2}$	1.42×10^{-3}
	919	1.088	$3.2\pm.1\times10^{-2}$	2.1×10^{-3}
I1(100)C	861	1.161	$1.5\pm.06\times10^{-2}$	9.59×10^{-4}
I2(100)D	828	1.208	$1.9\pm.15\times10^{-3}$	1.24×10^{-4}
	822	1.217	$1.4\pm.1\times10^{-3}$	8.86×10^{-5}
I2(100)F	836	1.196	$2.6\pm.1\times10^{-3}$	1.68×10^{-4}
I2(100)F	834	1.199	$2.54\pm.12\times10^{-3}$	1.63×10^{-4}
I2(100)F	834	1.199	$2.5\pm.1\times10^{-3}$	1.61×10^{-4}

a) Error estimate is absolute accuracy, not relative precision.

b) Computed by Eq. (V-1).

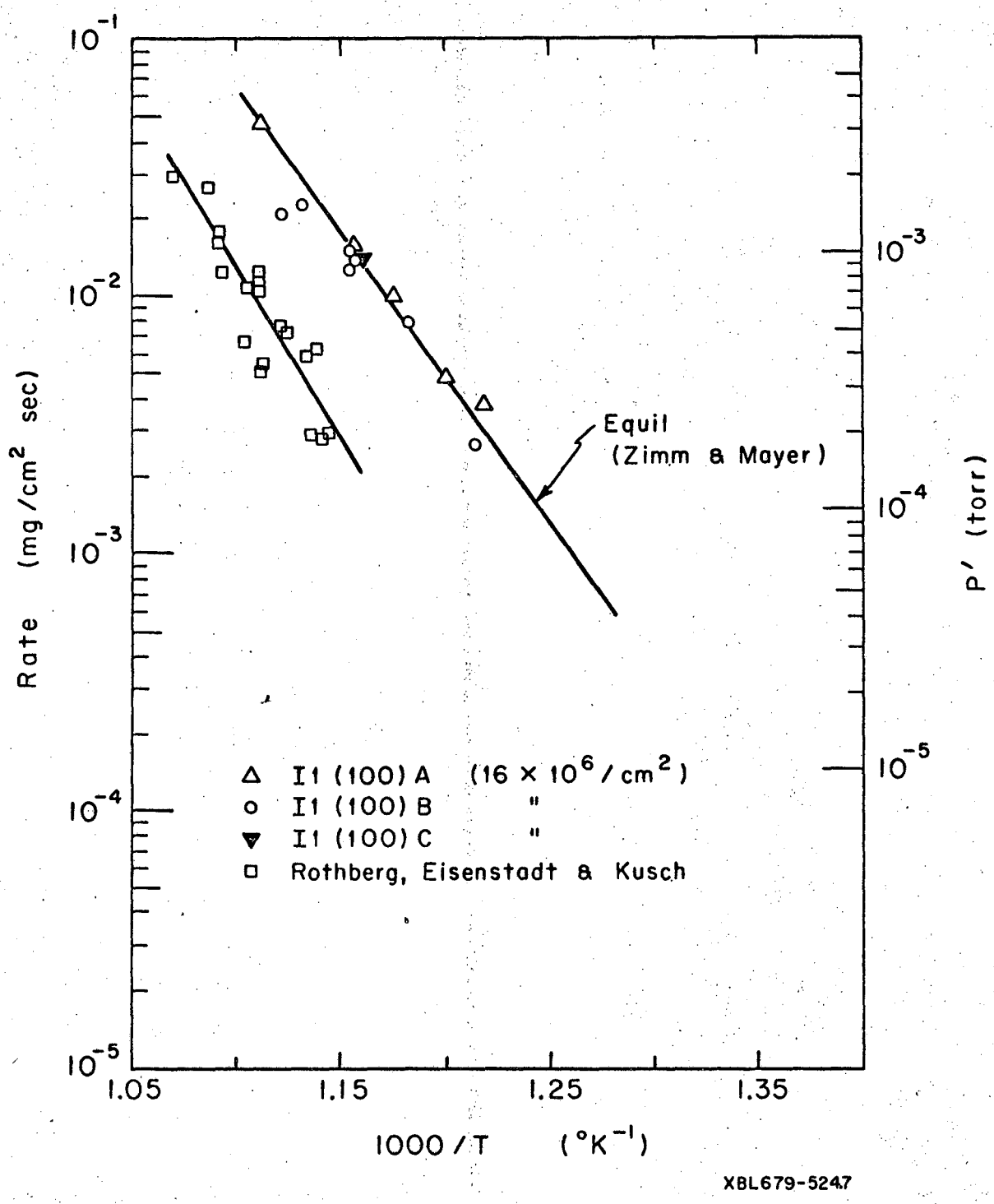

Fig. VI-1 Total evaporation rates of several samples. (Numbers in parentheses after sample number are etch pits per cm^2.)

The data from I1 (100) A, B, and C are plotted in Fig. VI-1. The equilibrium total evaporation rate calculated from the data of Zimm and Mayer[57] is included. The other free evaporation data plotted are the results of Rothberg, Eisenstadt, and Kusch.[22] The least squares fitted curve to the data of I1 (100) A, B, and C was

$$\log R = 9.2 \pm .5 - 9.6 \pm .3\times10^3/T$$

The data from several samples of lot II are given in Table VI-III. Crystal II2 had an etch pit count of $1.2\times10^6/cm^2$ and crystal II 60, which had been strained to introduce dislocations, had an etch pit count of $\sim 6\times10^6/cm^2$. The data from samples I2 (100) D and F, II2 (100) A and II60 (100) A are plotted in Fig. VI-2. Except for dislocation density these crystals were identical as far as we could tell (impurities, preparation technique). Since the dislocation densities of I2 and II2 were essentially identical they were fit to the same curve. The least squares curve for the data of I2 (100) D and F and II2 (100) A was

$$\log R = 11.7 \pm .3 - 1.2 \pm .1\times10^4/T$$

and to II60 (100) AS

$$\log R = 12.1 \pm .3 - 1.1 \pm .1\times10^4$$

Table VI-III and Fig. VI-2 also contain the microbalance data for the Semi Elements Company calcium doped crystal (Lot III). This crystal had a polyvalent (Al, Ca, Fe, Cu, Pb) impurity content of about 1100 ppm and an etch pit count of $4\times10^6/cm^2$. These were insufficient data to fit a meaningful curve but the evaporation rate measured was not as high as that of the strained crystals. The total evaporation rates of samples with high dislocation densities were significantly higher than the rates of crystals with low dislocation densities.

Table VI-III

Total evaporation rates for sodium chloride samples.
II2(100)A, II60(100)AS and III1(100)A

Sample	T (°K±6)	1/T (°K^{-1})	Rate (mg/cm^{2}sec)	P'[a] (torr)
II2(100)A	850	1.176	$4.45\pm.1\times10^{-3}$	2.92×10^{-4}
	827	1.209	$1.66\pm.1\times10^{-3}$	1.06×10^{-4}
	846	1.182	$3.16\pm.14\times10^{-3}$	2.07×10^{-4}
	880	1.136	$1.31\pm.1\times10^{-2}$	8.69×10^{-4}
	865	1.156	$7.7\pm .2\times10^{-3}$	5.05×10^{-4}
	838	1.193	$2.58\pm.1\times10^{-3}$	1.68×10^{-4}
	749	1.335	$5.0\pm.1\times10^{-5}$	3.07×10^{-6}
	899	1.112	$2.16\pm.1\times10^{-2}$	1.47×10^{-3}
II60(100)AS	774	1.292	4.89×10^{-4}	3.08×10^{-5}
	795	1.258	1.46×10^{-3}	9.22×10^{-5}
	814	1.229	3.18×10^{-3}	2.04×10^{-4}
	832	1.202	5.09×10^{-3}	3.31×10^{-4}
	852	1.174	1.15×10^{-2}	7.80×10^{-4}
	871	1.148	2.17×10^{-2}	1.43×10^{-3}
III1(100)A	885	1.130	$8.4\pm.1\times10^{-3}$	9.9×10^{-4}
	865	1.156	$7.65\pm.1\times10^{-3}$	5.02×10^{-4}
	863	1.158	$7.55\pm.1\times10^{-3}$	4.96×10^{-4}

a) Calculated from Eq. (V-1).

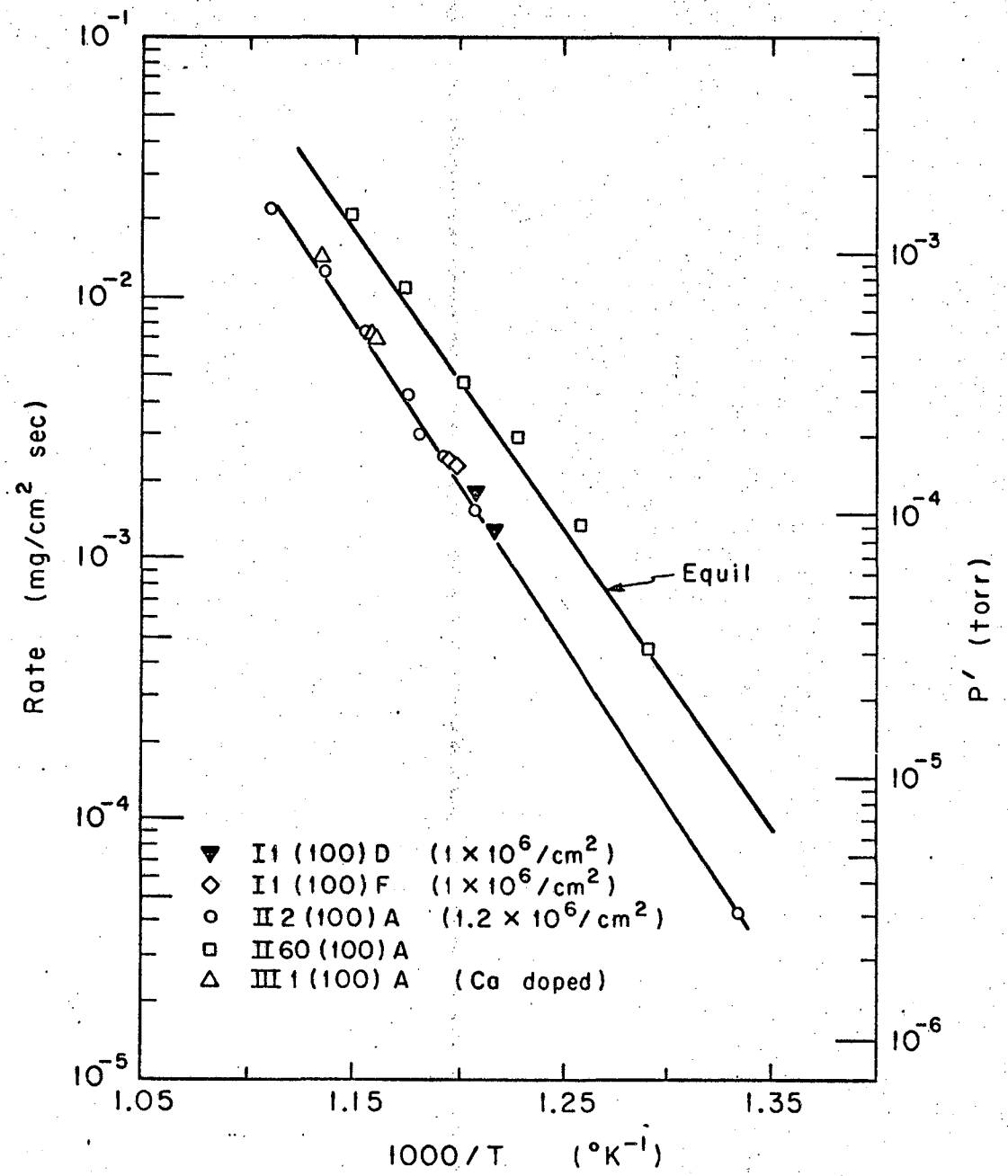

Fig. VI-2 Total evaporation rates of NaCl samples with low and high etch pit counts. The numbers in parentheses after sample numbwrs are etch pits per cm^2.

C. Vapor Composition and Activation Energies of Vaporization of NaCl (Mass Spectrometric Studies)

The vapor emitted from a NaCl crystal contains both monomer and polymer molecules.[54] The dominant species are NaCl (v) and Na_2Cl_2 (v). The contribution of each of these species to the vapor flux from the NaCl samples was monitored as a function of temperature using a quadrupole mass spectrometer. Because of the large number of samples used in these experiments the data will be tabulated by the parameters of the least squares curves fitted to

$$\log I_i T = A + B/T$$

$$i = 1, 2, \text{ and } 3.$$

The monomer/dimer ratio data are reported as

$$\log I_M/I_D = A_{MD} + B_{MD} (1/T)$$

This monomer/dimer ratio may be converted to pressure ratios using the applicable relative ionization cross sections and of transmission factors for the various molecules. (See Appendix B) Thus,

$$\log \frac{P_M}{P_D} \sim A_{MD} + B_{MD}/T$$

1. Knudsen Effusion Experiment on NaCl

An effusion cell measurement was made with sodium chloride in order to test the accuracy of the experimental apparatus. The results are

$$\log I_{23}T = 7.07\pm.2 - 1.133\pm.02\times10^4/T$$

$$\log I_{58}T = 7.42\pm.3 - 1.158\pm.02\times10^4/T$$

$$\log I_{8k}T = 8.38\pm.3 - 1.277\pm.02\times10^4/T$$

and are shown in Fig. VI-3. The measured heats of vaporization for the monomer and dimer were 52.4±1 and 58.4±1 kcal/mole at 800°K. The accepted values are 52.1 and 59.5 kcal/mole; at this temperature.[15,58] The agreement is quite good, thus the activation energies measured in this research should be reliable. The monomer to dimer ionic ratio for these data is given by

$$\log I_M/I_D = .7\pm.2 + 1.2\times10^3\pm.1/T$$

At T = 1000°K this yields $I_M/I_D = 2.6$. The only reported value at 1000°K is for the pressure ratio M/D and is 3.0.

2. Annealed and Untreated Crystals

A number of crystals were used after cleaving and etching without any further preparation. Several crystals were annealed in vacuum or under an atmosphere of dry nitrogen. The results obtained from both sets of samples are given in Table VI-IV and plotted in Figs. VI-4 to VI-10. Monomer-dimer ratios were not calculated for samples I2 (100) G-I4 (100) A because instrumental repairs that altered the transmission probabilities were made between the experiments on these samples and the rest of the experiments.

3. Impurity Containing Crystals

The effect of certain impurities on the activation energy or the monomer to dimer ratio was investigated for the impurities: Br^-, O_2^-, OH^- and Ca^{++}. Bromine was chosen because it was present in relatively large concentrations in the Harshaw samples: oxygen and OH^-, because they could have been introduced by suspected impurities in the crystal growth apparatus; and calcium, because it was a polyvalent ion and

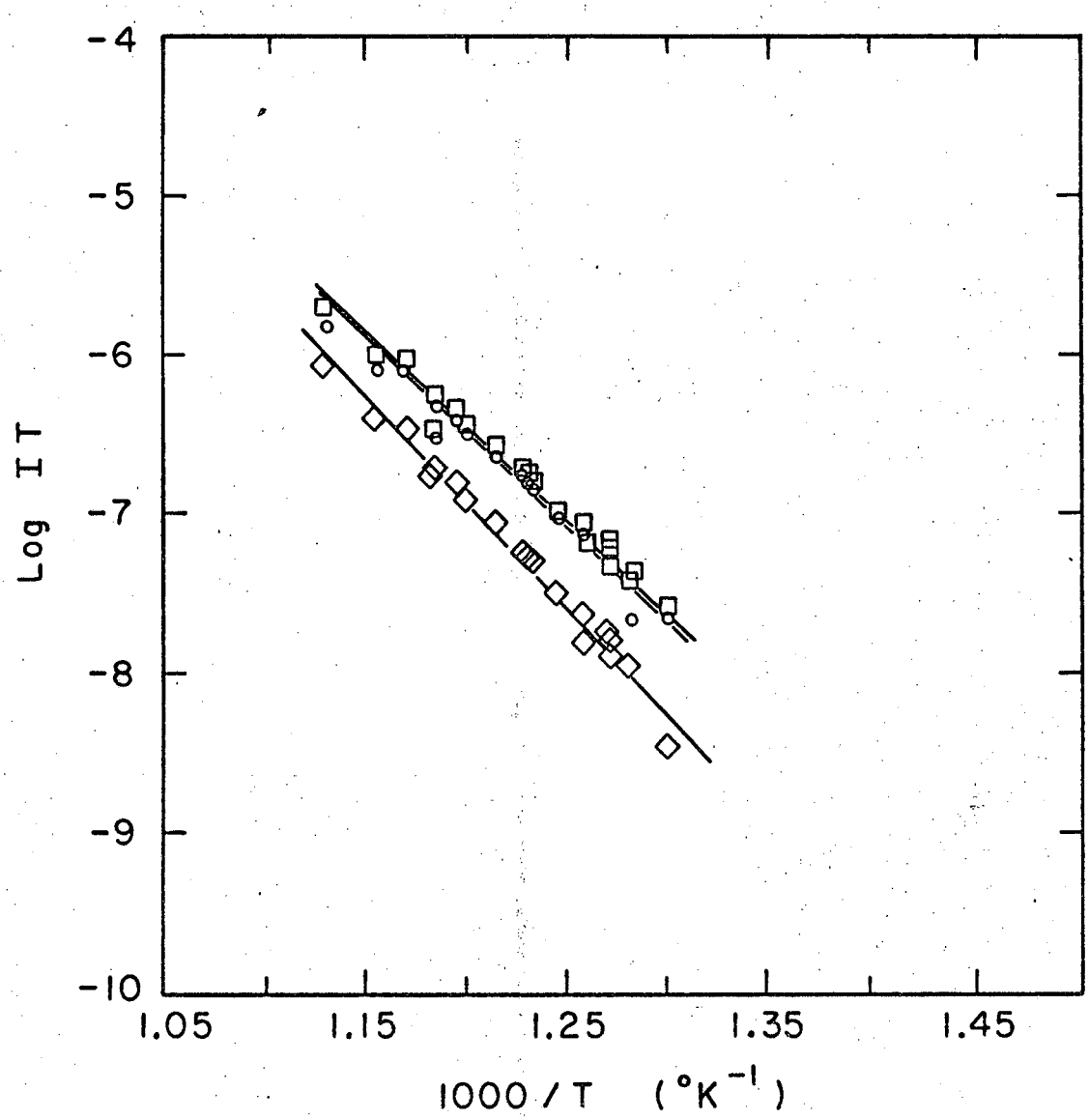

XBL679-5249

Fig. VI-3 Knudsen effusion results
(O = Na^+ ; □ = $NaCl^+$ ◇ = Na_2Cl^+)

Table VI-IV

Mass spectrometer results on NaCl.

Sample	I2(100)G	I3(100)A	I4(100)A	I5(100)A	II51(100)A	IV19(100)K	II58(100)A
Annealing	none	none	none	450°C vac	none	none	700°C N_2
Etch Pit density	--	--	--	$.8\times10^6$	--	$\sim2\times10^6$	2×10^6
A_1	8.61±.2	8.41±.3	9.48±.3	7.61±.2	8.04±.4	8.59±.3	8.28±.2
$-B_1\times10^{-4}$	1.157±.02	1.144±.03	1.242±.02	1.116±.015	1.162±.05	1.188±.02	1.188±.01
A_2	8.10±.2	8.69±.3	9.24±.3	7.63±.2	7.28±.3	8.55±.3	8.03±.2
$-B_2\times10^{-4}$	1.101±.02	1.150±.03	1.212±.02	1.1018±.02	1.112±.03	1.190±.03	1.169±.02
A_3	10.52±.2	10.59±.3	11.36±.3	9.155±.2	10.28±.3	10.23±.3	9.68±.1
$-B_3\times10^{-4}$	1.341±.02	1.345±.03	1.422±.02	1.2725±.02	1.405±.05	1.361±.02	1.354±.01
$-A_{MD}$	--	--	--	.96±.2	2.3±.3	1.2±.2	1.3±.2
$B_{MD}\times10^{-3}$	--	--	--	1.4±.2	2.7±.3	1.6±.2	1.8±.2
E^*_M	51.7±1.4	52.4±1.5	56.1± 1	50.7± 1	52.0±1.2	54.4± 1	54.0± 1
E^*_D	61.3±1.4	61.5±1.6	65.1± 1	58.2± 1	64.3± 2	62.3± 1	62.0±.4

AVG[1] E^*_M 52.6± 1

AVG E^*_D 62.1± 1

1 Corrected for dimer contribution to monomer peaks.

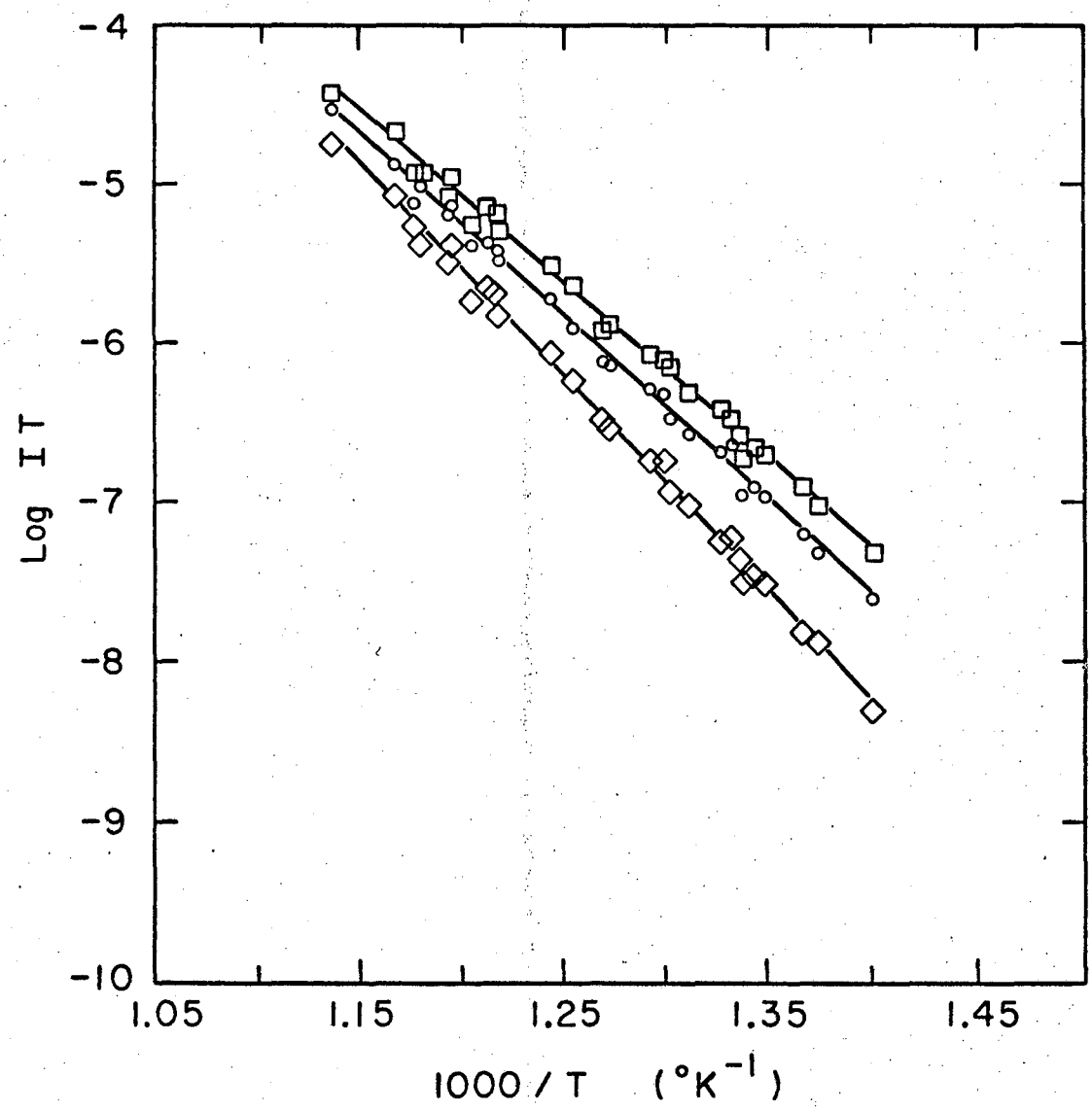

XBL679-5250

Fig. VI-4 Mass spectrometric results for sample I2 (100) G
(O = Na^+ □ = $NaCl^+$ ◇ = Na_2Cl^+)

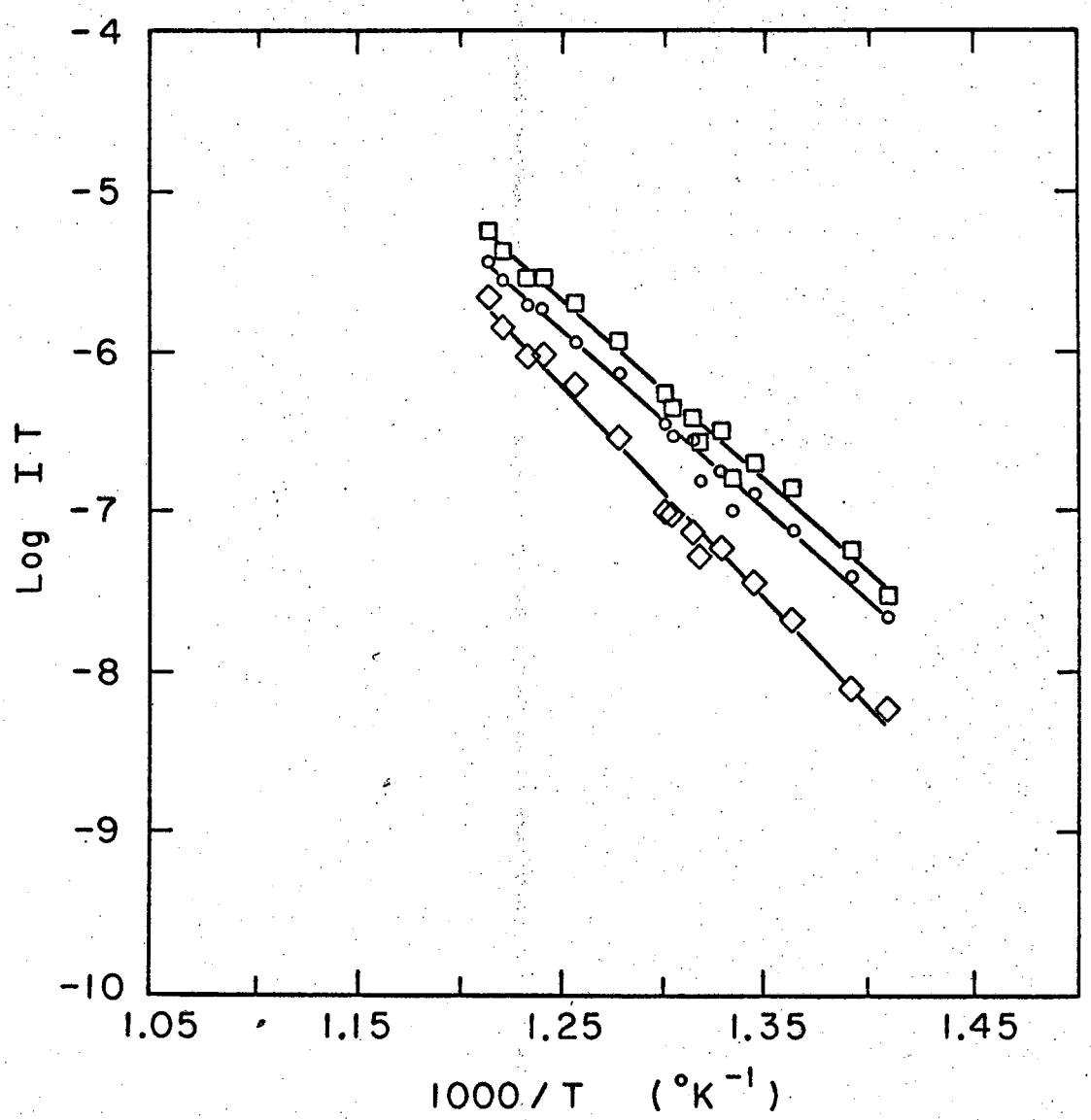

XBL679-5251

Fig. VI-5 Mass spectrometric results for sample I 3 (100) A

(O = Na^+ □ = $NaCl^+$ ◇ = Na_2Cl^+)

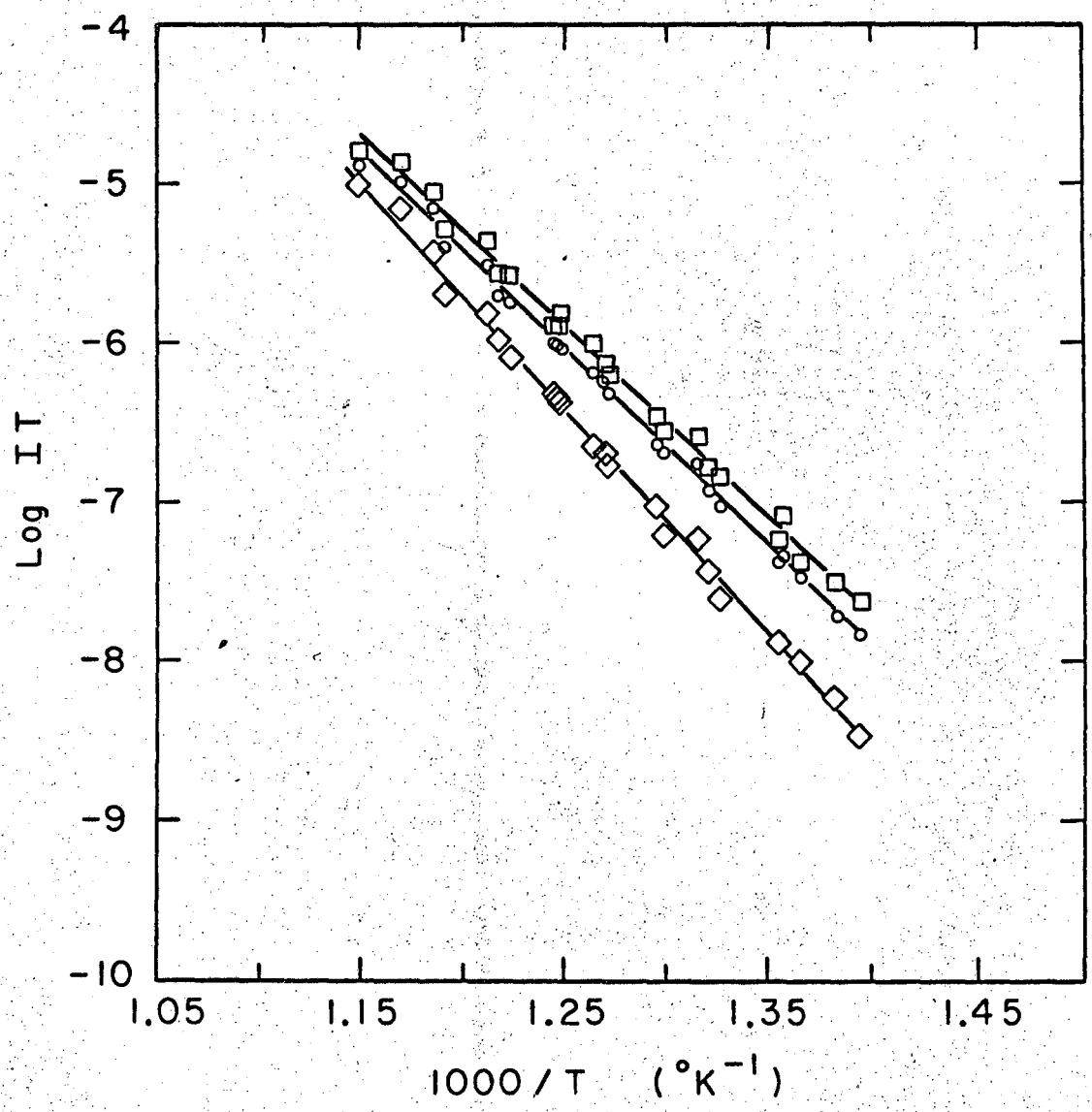

XBL679-5252

Fig. VI-6 Mass spectrometric results for sample I 4 (100) A
(O = Na^+ □ = $NaCl^2$ ◇ = Na_2Cl^+)

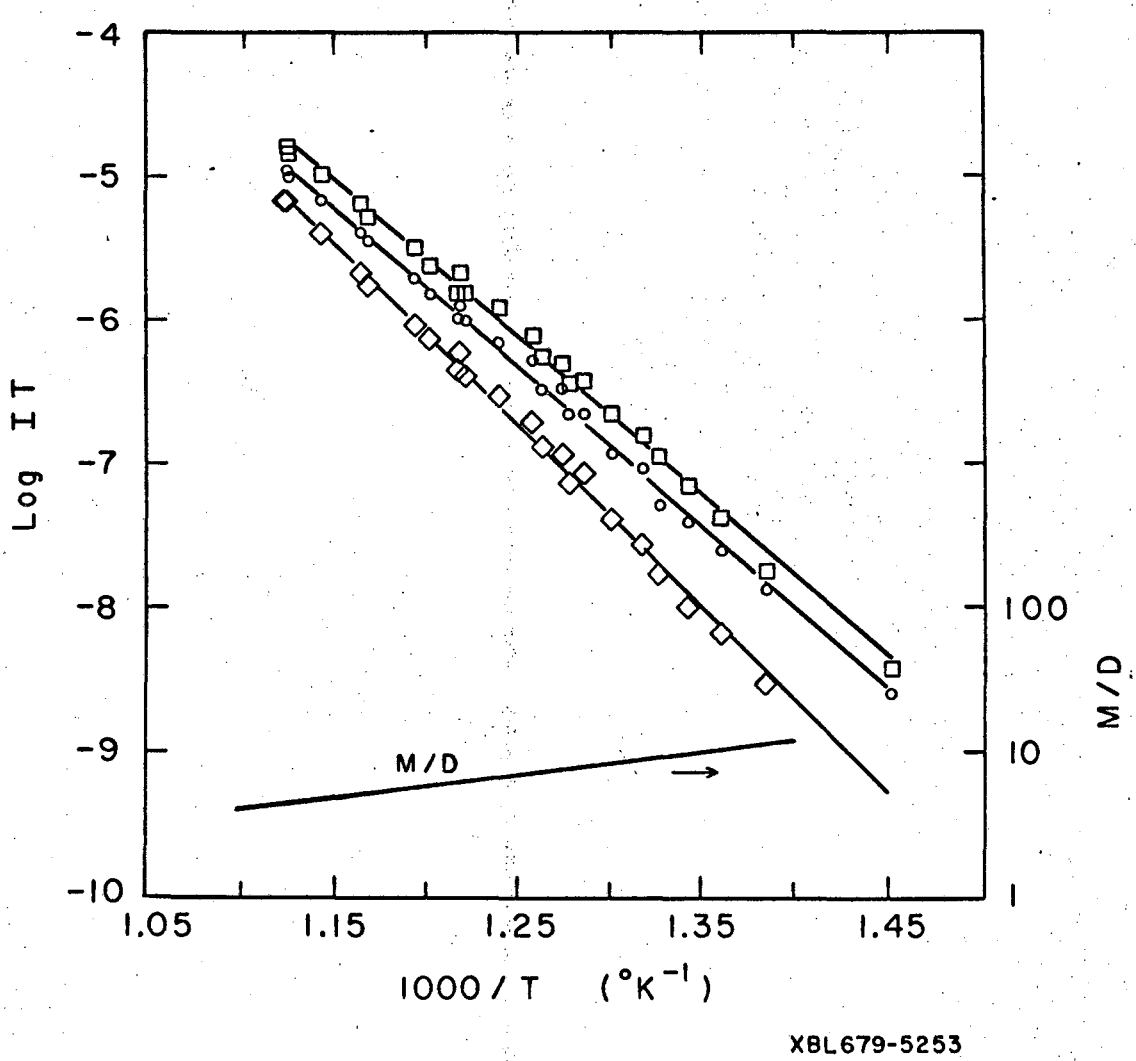

Fig. VI-7 Mass spectrometric results on sample I 5 (100) A

(O = Na^+ □ = $NaCl^+$ ◇ = Na_2Cl^+)

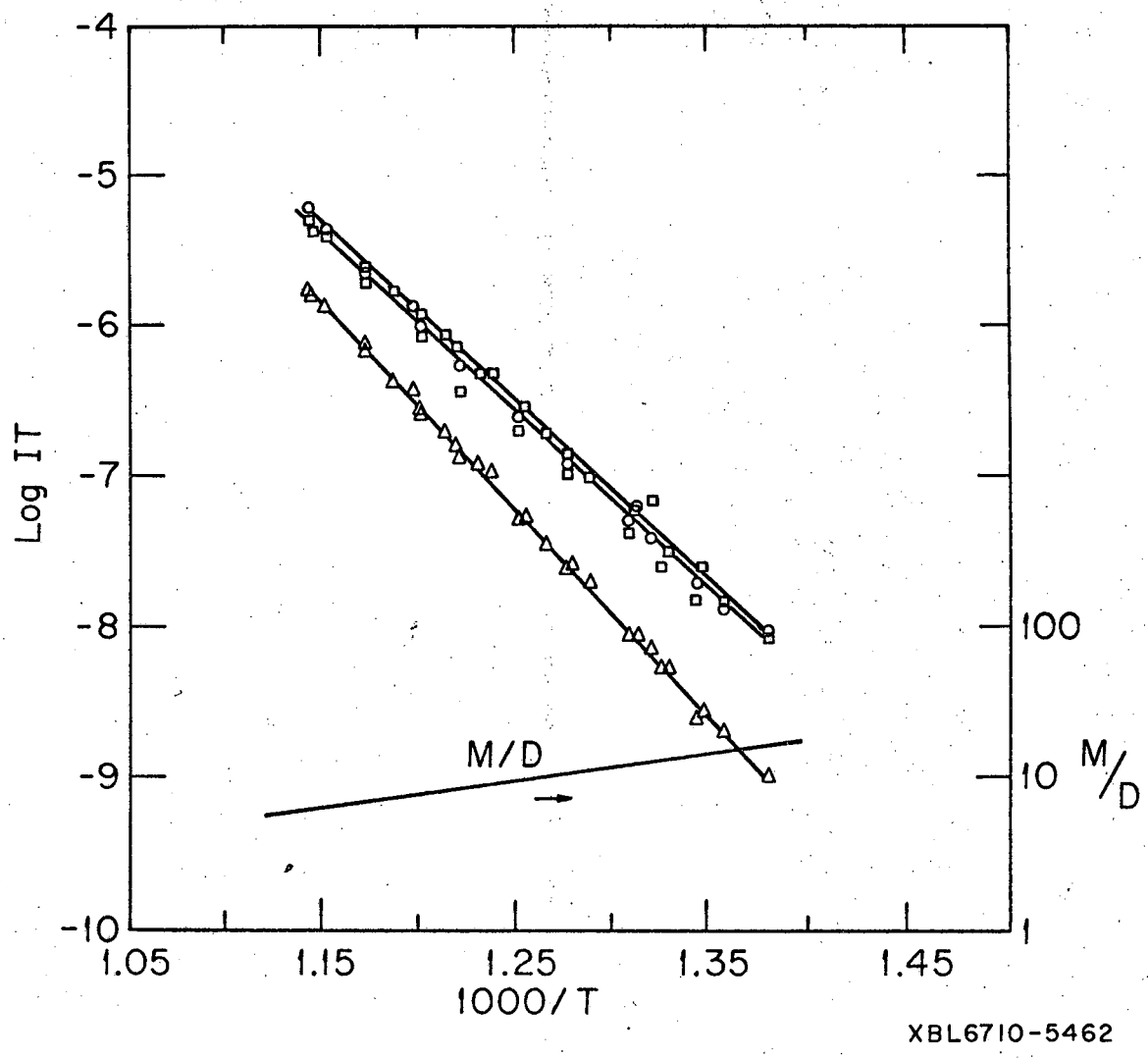

Fig. VI-8 Mass spectrometric results for sample II 51 (100) A
(O = Na^+ □ = $NaCl^+$ △ = Na_2Cl^+)

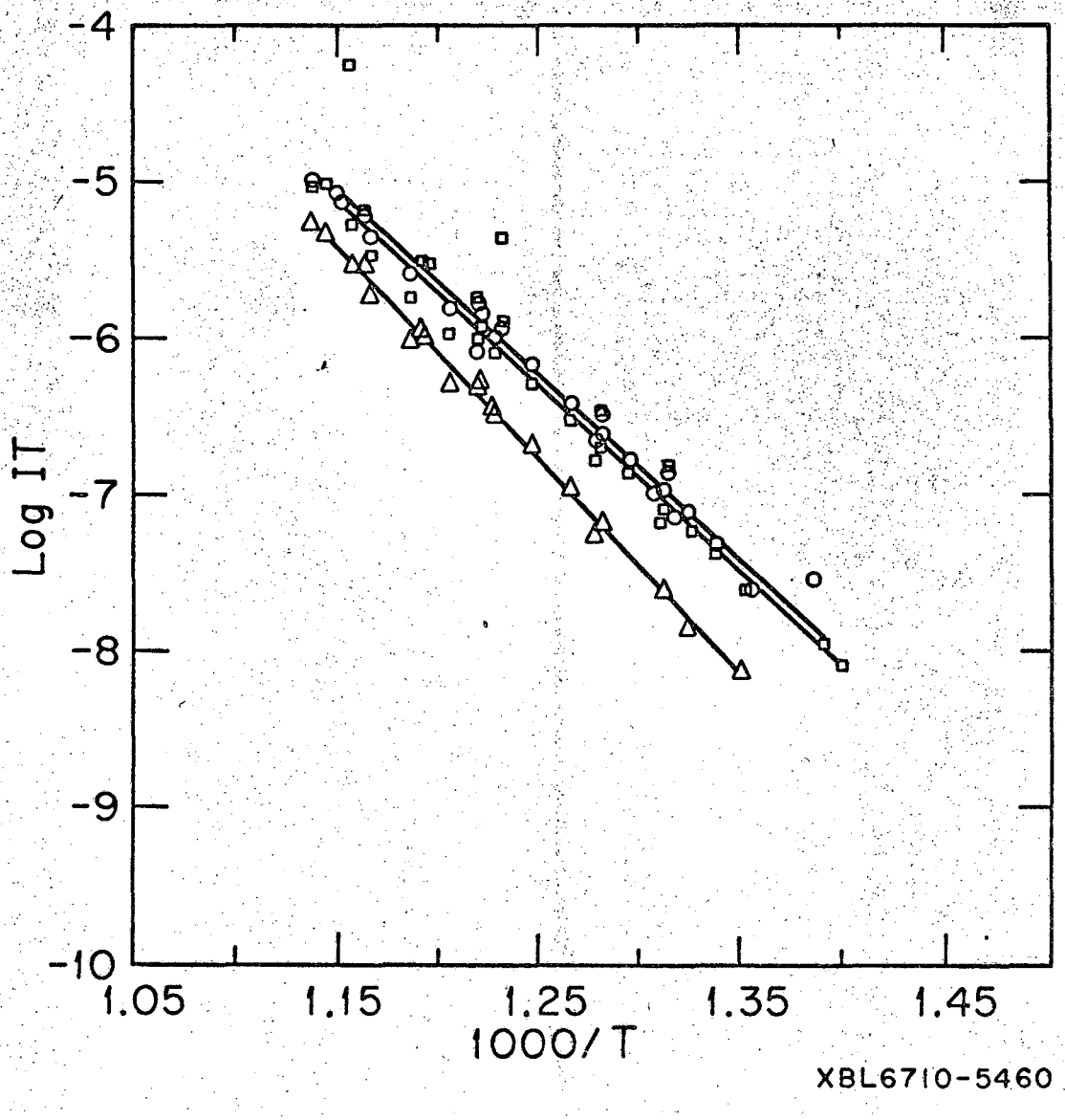

Fig. VI-9 Mass spectrometric results on sample IV 19 (100) K

(O = Na^+ □ = $NaCl^+$ △ = Na_2Cl^+)

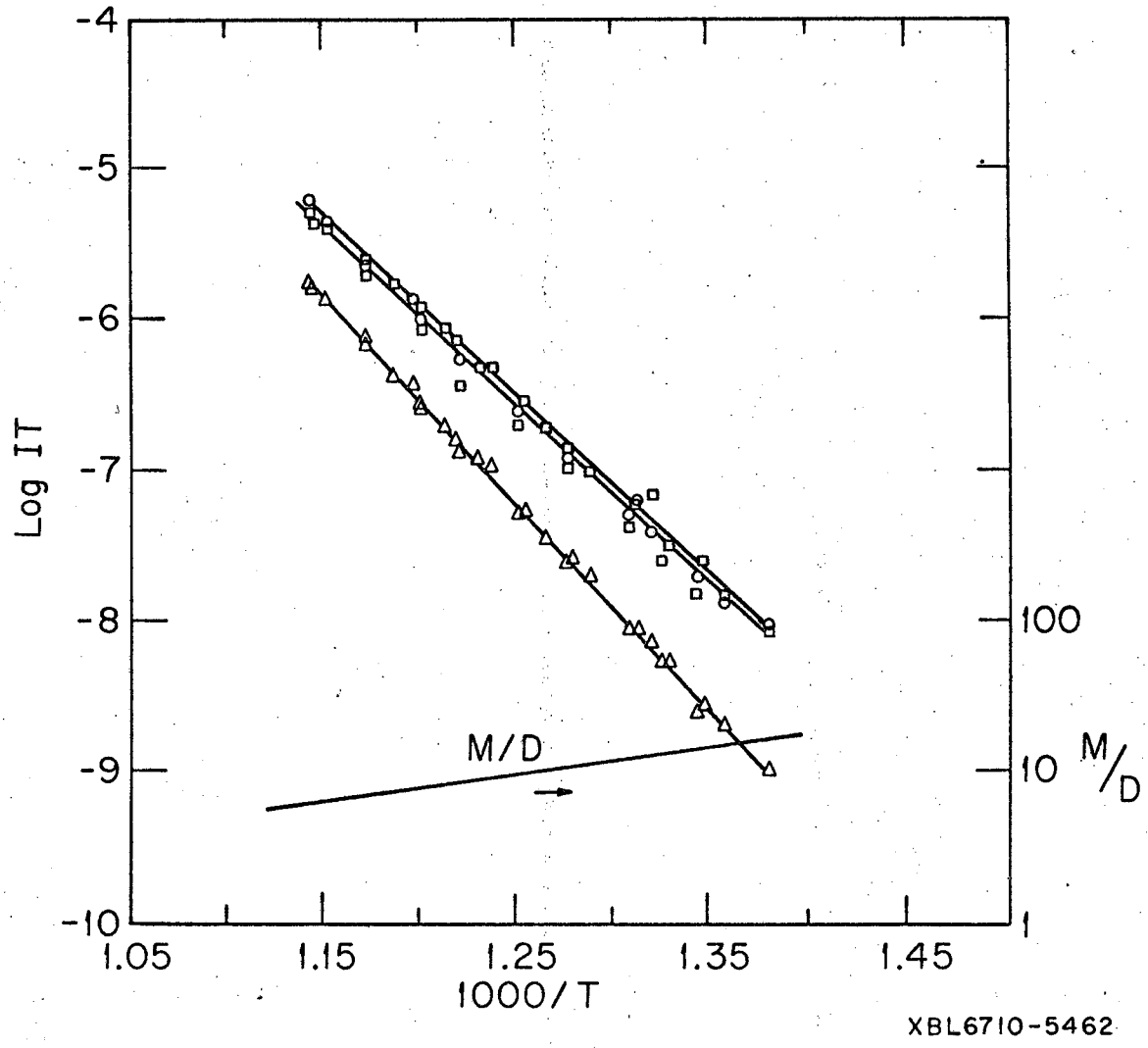

Fig. VI-10 Mass spectrometric results on sample II 58 (100) A
(O = Na^+ □ = $NaCl^+$ △ = Na_2Cl^+)

polyvalent ion impurities are known to strongly affect the electrical properties of NaCl.[16] The analyses of the samples are given in Table III-I. Although the "calcium doped" sample did not have the desired calcium concentration it was used anyway because it did have a high or polyvalent cation impurity content, (~100 ppm) than the Harshaw and zone refined crystals. The results are shown in Table VI-V and Figs. VI-11 to VI-14. The only impurity doped sample whose activation energy is significantly different from the average value of the undoped samples (Table VI-IV) is the calcium doped sample.

4. High Dislocation Density Crystals

Samples with high dislocation densities were also used in these mass spectrometer studies (See Sec. VI-B for weight loss measurements on high dislocation density samples). in order to obtain an activation energy of vaporization for the monomer and dimer from the highly strained crystals and to see what effect the dislocation density had on the monomer-dimer ratio. The results are shown in Table VI-VI and Figs. VI-15 to VI-17. Sample II58 (100) A is included in the table as a reference sample which was taken from the same lot of Harshaw crystals and annealed before use. The activation energies of the samples with the highest dislocation densities are significantly larger than those of the unstrained crystals.

Table VI-V

Mass spectrometer results on impurity doped NaCl.

Sample	I6(100)A0	V21(100)A	II57(100)0	III1(100)D
Impurity[a]	Oxygen	Bromine	Oxygen	Divalent
Etch Pit Count	3×10^6	1×10^6	unk	4×10^6
A_1	8.11±.2	8.46±.4	7.71±.3	8.89±.2
$-B_1\times10^4$	1.159±.015	1.177±.04	1.129±.01	1.239±.01
A_2	7.51±.3	8.54±.4	7.88±.2	8.63±.3
$-B_2\times10^4$	1.124±.03	1.189±.04	1.142±.01	1.214±.01
A_3	9.77±.2	10.60±.4	10.03±.3	10.58±.2
$-B_3\times10^4$	1.364±.02	1.392±.03	1.368±.01	1.423±.01
A_{MD}	-1.4±.2	-1.8±.3	-2.0±.3	
B_{MD}	2.0±.2	2.1±.2	2.3±.2	
E^*_M	52.3±1.3	54.2± 1	52.0±.5	56.1±.6
E^*_D	62.4± 1	63.7±1.4	62.6±.6	65.1±.4

a) See Table III-1 for impurity concentrations.

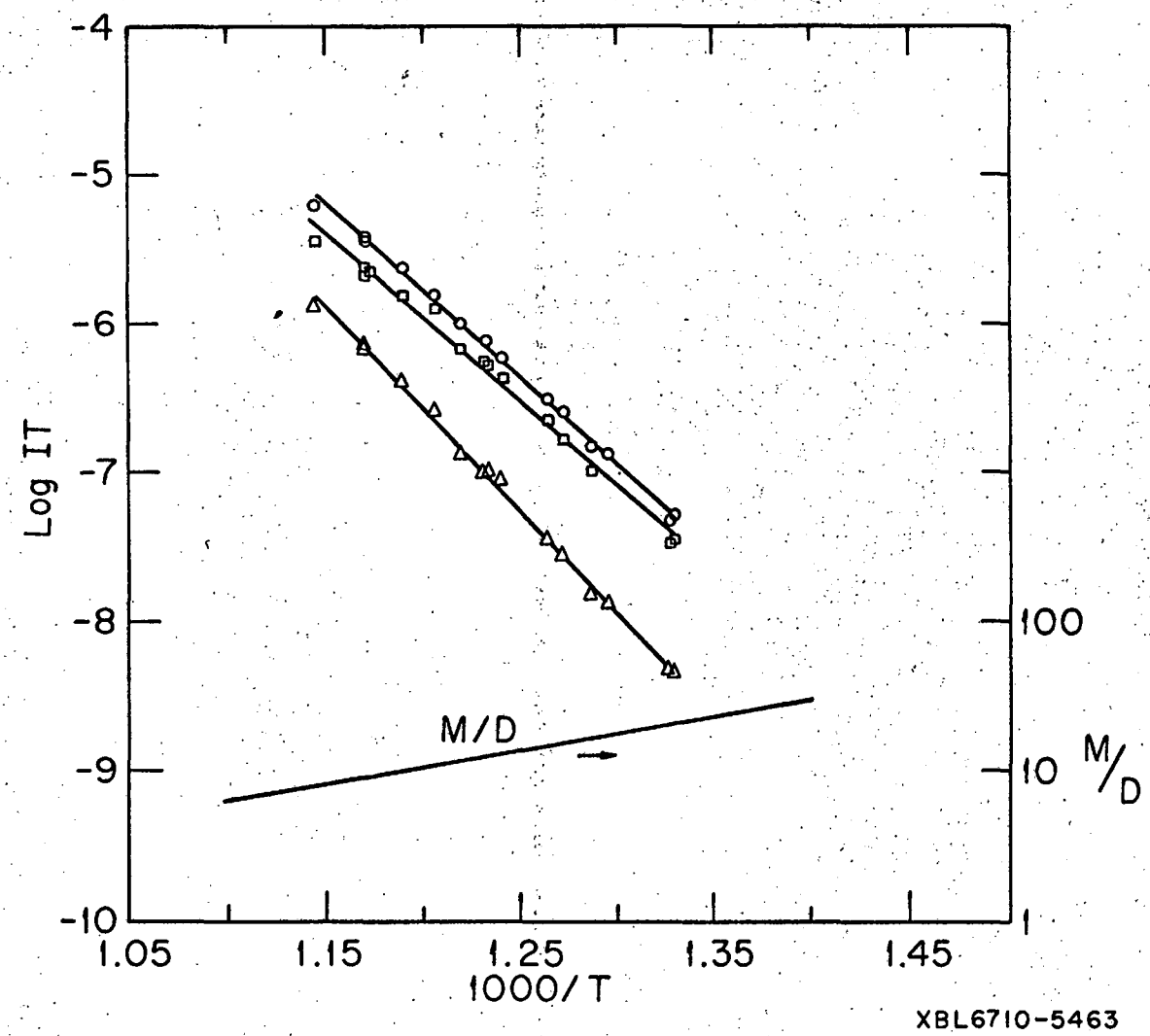

Fig. VI-11. Mass spectrometric results on sample I 6 (100) AO
(O = Na^+ □ = $NaCl^+$ △ = Na_2Cl^+)

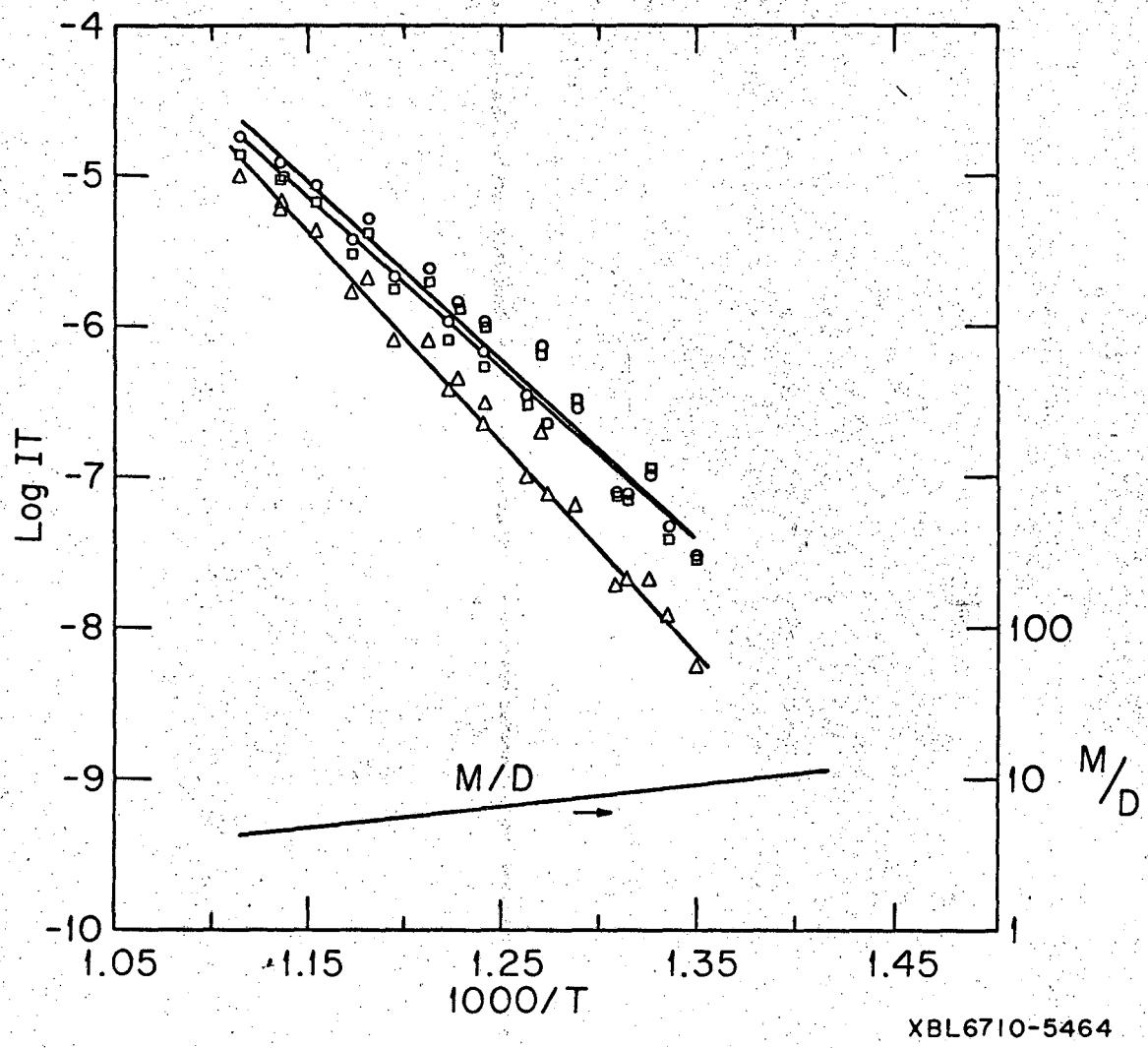

Fig. VI-12 Mass spectrometric results on sample V 21 (100) A

(O = Na^+ □ = $NaCl^+$ △ = Na_2Cl^+)

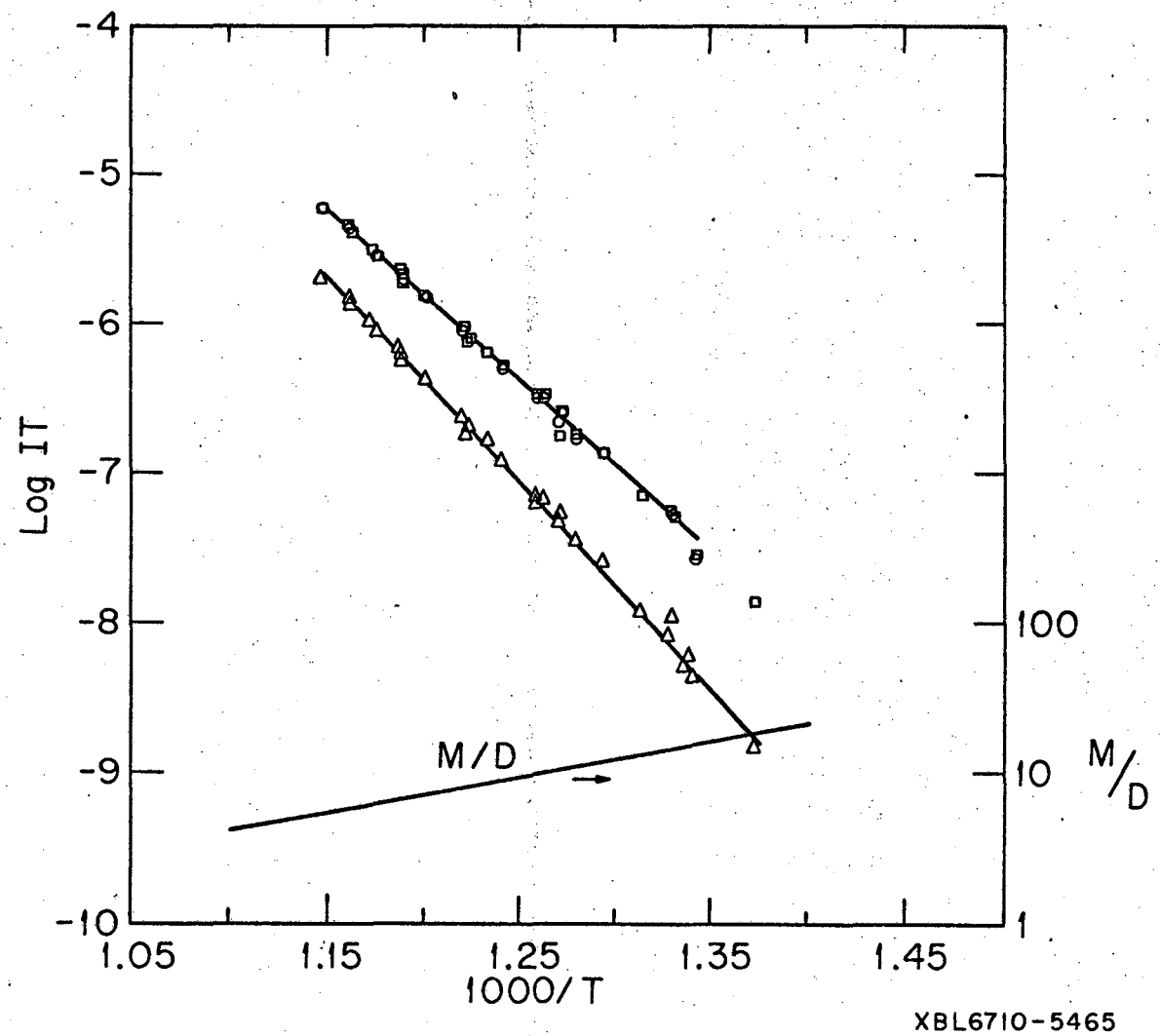

Fig. VI-13 Mass spectrometric results on sample II 57 (100) 0
(0 = Na^+ □ = $NaCl^+$ △ = Na_2Cl^+)

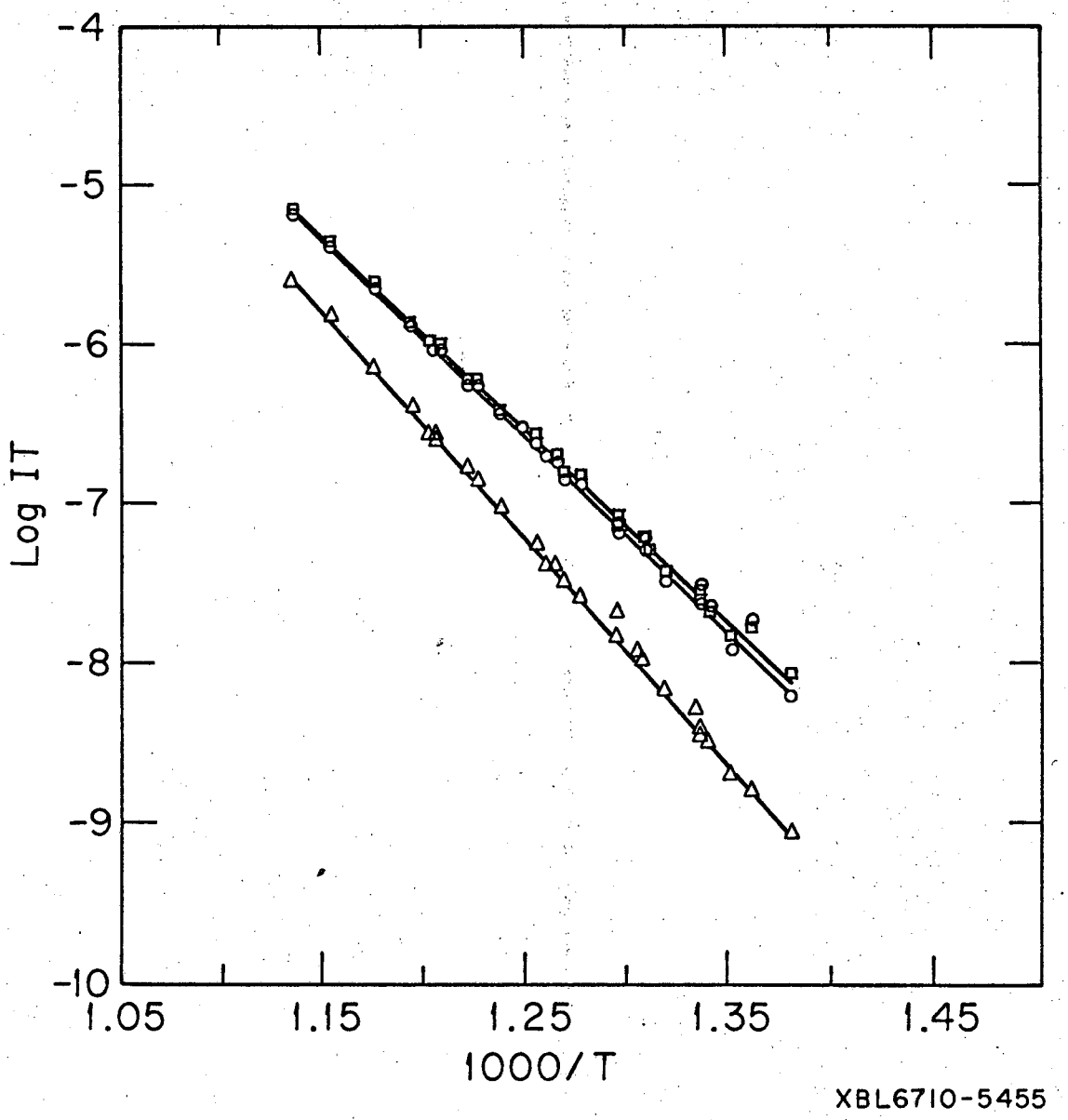

Fig. VI-14 Mass spectrometric results on sample III-1 (100) D
(O = Na^+ □ = $NaCl^+$ △ = Na_2Cl^+)

Table VI-VI

Mass spectrometer results on NaCl crystals with high dislocation densities.

Sample	II58(100)A	II56(100)BS	II59(100)AS	II62(100)AS
Etch Pit Count	2×10^6	$\sim4\times10^6/cm^2$	$\sim6\times10^6$	$>15\times10^6/cm^2$
A_1	8.28±.2	9.05±.3	8.50±.3	8.88±.3
$-B_1$	1.188±.01	1.222±.02	1.190±.02	1.249±.02
A_2	8.03±.2	8.76±.4	8.08±.4	8.62±.3
$-B_2$	1.169±.02	1.211±.01	1.164±.02	1.223±.02
A_3	9.68±.1	11.06±.3	10.30±.3	9.75±.3
$-B_3$	1.354±.01	1.433±.01	1.383±.02	1.373±.02
$-A_{MD}$	1.2±.2	1.8±.3	1.6±.3	.8±.3
$B_{MD}\times10^{-3}$	1.8±.2	2.2±.2	2.0±.2	1.4±.2
E^*_M	54.0± 1	55.6±.6	53.8±1.1	56.6±.7
E^*_D	62.0±.4	65.6±.6	63.3±.8	62.8±.9

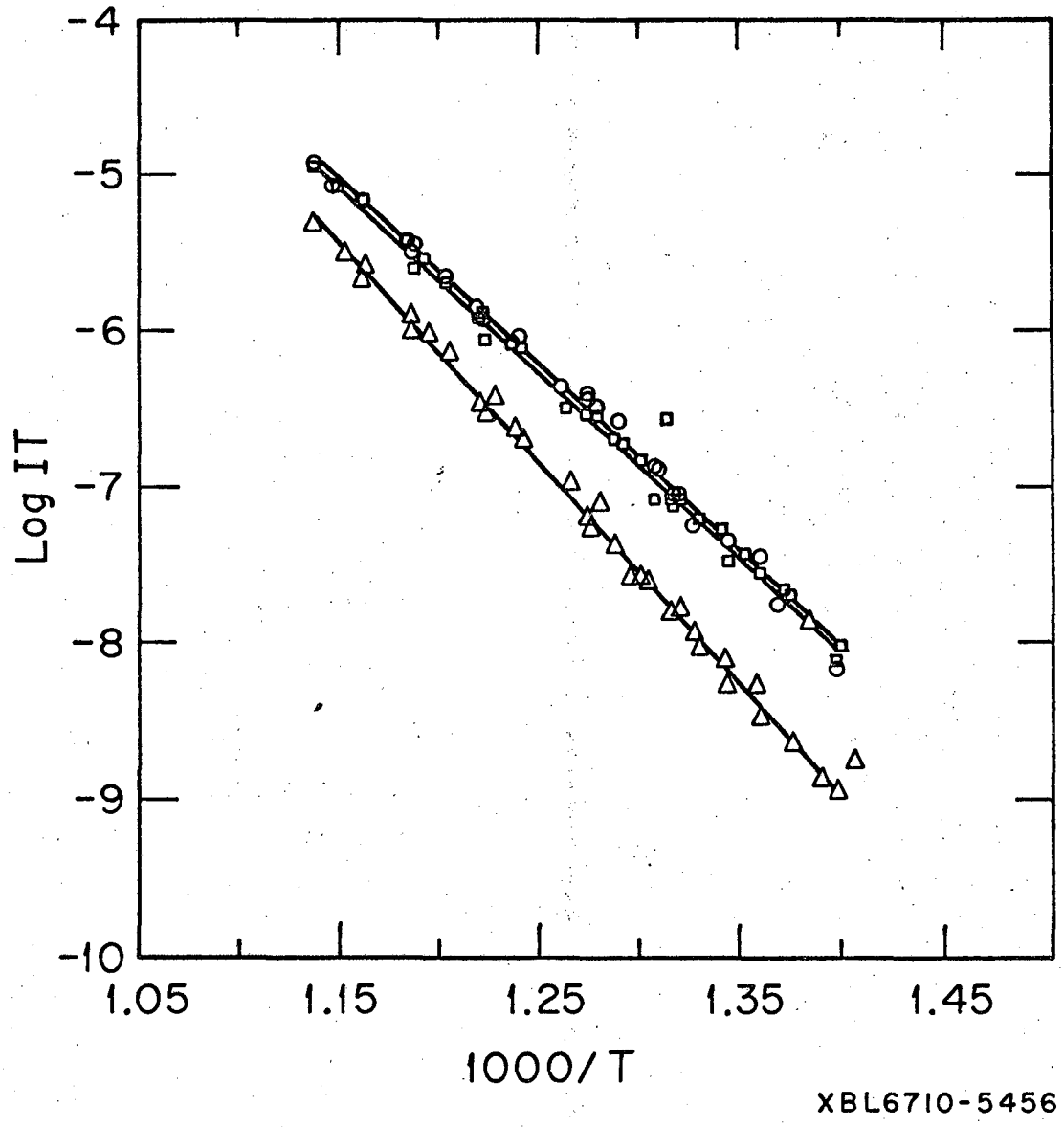

Fig. VI-15 Mass spectrometric results on sample II 56 (100) BS
(O = Na^+ □ = $NaCl^+$ △ = Na_2Cl^+)

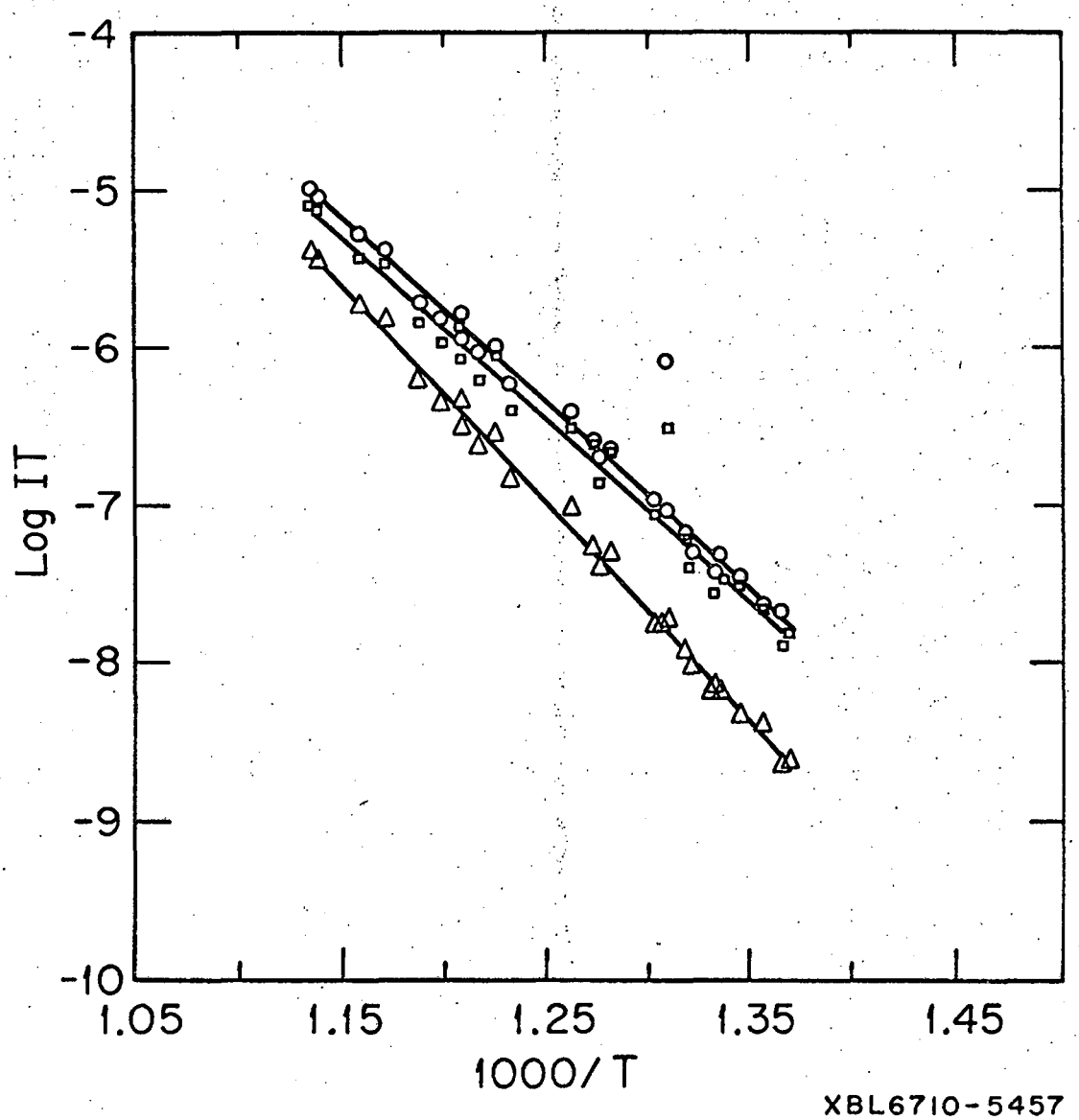

Fig. VI-16 Mass spectrometric results for sample II 59 (100) AS
(O = Na^+ □ = $NaCl^+$ △ = Na_2Cl^+)

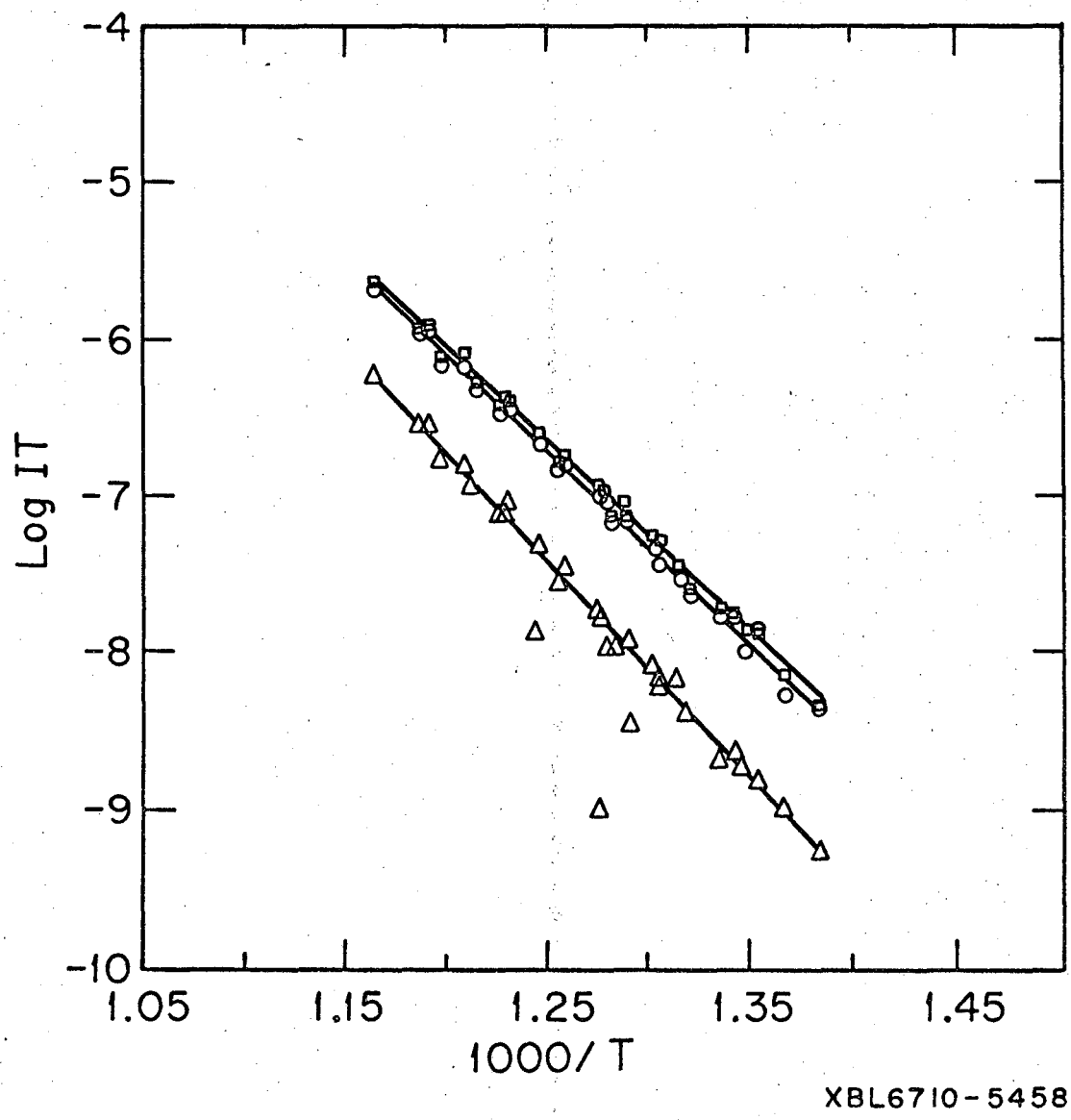

Fig. VI-17 Mass spectrometric results on sample II 62 (100) AS
(O = Na^+ □ = $NaCl^+$ △ = Na_2Cl^+)

VII. DISCUSSION

A. Effect of Dislocation Density on the Vaporization Characteristics of NaCl

The total rate of vaporization of the (100) face of NaCl single crystals measured in this research was lower than the equilibrium rate (Eq. II-2) by about a factor of two for crystals which had an etch pit count of approximately $1\times10^6/cm^2$. However, crystals with larger etch pit counts, in the range of $5\times10^6/cm^2$ to $15\times10^6/cm^2$, had evaporation rates which were equal to the equilibrium rate. Other than the difference in their dislocation density, the crystals were identical; they were grown under identical conditions and had approximately equal impurity concentrations. The only other determination of the total rate of vaporization of NaCl single crystals was reported by Rothberg, Eisenstadt, and Kusch.[22] Their reported total evaporation rate is almost an order of magnitude below the equilibrium rate in the temperature region in which it was measured. They do not report the dislocation density of their crystals. Expressing these results in terms of the evaporation coefficient, an order of magnitude increase in the dislocation density increased the average evaporation coefficient from $\alpha_v \sim 0.5$ to $\alpha_v \sim 1.0$, while Kusch, et al. reported an evaporation coefficient of $\alpha \approx 0.1$ The variations in evaporation rates of crystals with different dislocation densities are greater than the estimated error in our measurements by about a factor of two.

The mass spectrometric data indicates that an increase in the evaporation rate is accompanied by an increase in the activation energy. These changes were small, two to four kilocalories, but the deviation

of E_v^* from the average activation energy exhibited by the low dislocation density crystals was greater than the standard deviation of the data.

The overall vaporization rate can be expressed by

$$R_v = K_o(A)\ e^{-E^*/RT}$$

where K_o is a constant related to the frequency of motion of a molecule over the energy barrier, E^*, and (A) is the concentration of molecules at the initial site from which vaporization proceeds. A change of two kilocalories in the activation energy would change the evaporation rate of NaCl by a factor of 3 at 800°K if there were no accompanying change in the pre-exponential factors. The observed higher activation energy of vaporization for crystals with large dislocation densities should lower their evaporation rate. We observed an increase in the rate (×2), however. Thus it must be concluded that the pre-exponential factor increased by approximately an order of magnitude in order to account for the increased evaporation rate. It is most likely that this increase in the magnitude of the pre-exponential factor as more dislocations are introduced is due to an increase in the number of surface sites from which vaporization is initiated. Rosenblatt, et al.[7] have observed an arsenic single crystal face during vaporization using an optical microscope. They found that they could account for all of the vaporization flux by the growth of pits around dislocations. There is a definite roughening of the sodium chloride surface during evaporation which is probably due to a combination of normal ledge motion and enhanced vaporization around dislocations. It is apparent, from our data, that a dislocation density of about $10^7/cm^2$ is sufficient to establish a rate equal to the equilibrium rate, however we cannot say what the lower limit of α_v will be as we were not able to prepare any

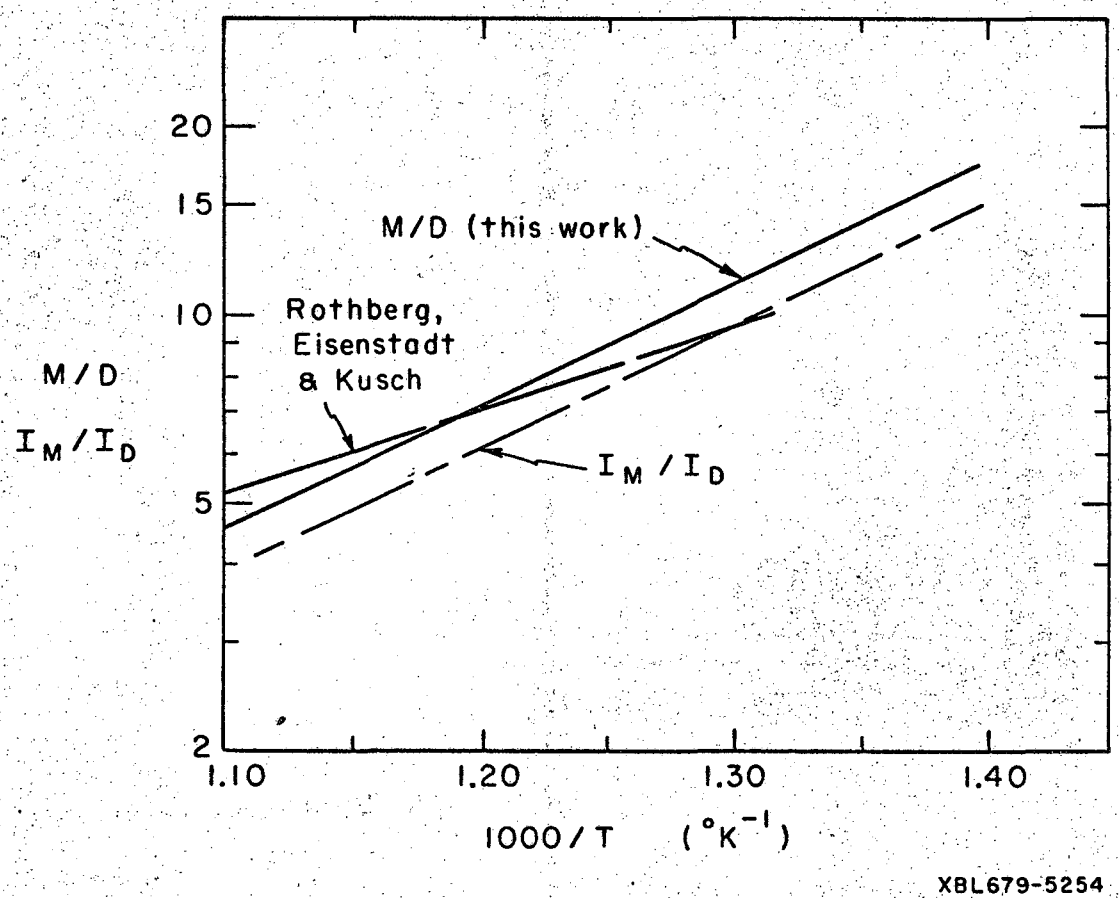

Fig. VII-1 Monomer-dimer ratios obtained by molecular beam and mass spectrometric techniques (see appendix for conversion of I_M/I_D to M/D).

samples with dislocation densities lower than ~ 1×10^6.

Since both the evaporation rate and activation energy depend on the dislocation density we had to determine what free evaporation rate and activation energy are intrinsic to an unstrained, pure NaCl (100) crystal surface. We have chosen the average of the activation energies and total rates of the unstrained and undoped crystals as characteristic of the vaporization of pure NaCl. These crystals had an average dislocation density of ~ $1\times10^6/cm^2$ as measured by etch pit density. The activation energies are 52.6±1 and 62.1±1 kcal/mole of vapor for the monomer and dimer, respectively. Kusch, et al.[22] reported 61.7±4.6 and 67.2±4.6 kcal/mole, respectively.

The monomer-dimer ion ratios that we measured are unchanged by the dislocation density of the crystal to the accuracy of the experimental data. If we apply the cross section ratio necessary to fit our effusion cell data to Gorokhov's[56] reported monomer-dimer ratio, then our average monomer-dimer ratio in the temperature range 450°C to 900°C agrees with the values of Rothberg, Eisenstadt and Kusch within the experimental error of the experiments (Fig. VII-1), and yields M/D = 4.5 at 900°K and M/D = 18 at 700°K. The constancy of the ratio, M/D(T) for all the crystals, even though the activation energies change from crystal to crystal, is a consequence of the fact that the difference, $E_M^*-E_D^*$, is constant within experimental error.

B. Effect of Impurities on the Evaporation Behavior of NaCl

Of the impurities that we introduced into the lattice bromine (as Br^-) and oxygen (as O_2^- or OH^-) had no detectable effect on the activation energy or monomer-dimer ratio. This was determined by comparing the results of crystals containing (deliberately or otherwise) these impurities with the results of the zone refined Kyropolous

grown sample which had a very low impurity concentration (see Table III-1). The divalent cation doped crystal ($M^{++} > 100$ ppm) did show higher activation energies than the normal crystals. However, this crystal had a somewhat high dislocation density ($\sim 4\times10^6/cm^2$) which may be responsible for part of the change. We also observed however that the total evaporation rate of this crystal was not as high as the dislocation density would indicate if it behaved in the same way as the strained crystals. More work is needed in this area in order to elucidate the effect of the impurity (if any) from the effect of the dislocations.

C. Comments on the Mechanism of Vaporization of NaCl

The major features of the vaporization kinetics of sodium chloride seem to be explainable in terms of the Kossel-Stranski[26,27] model of a crystal surface (Fig. VII-2) and a stepwise model of vaporization. We shall consider a possible model of the vaporization of an alkali halide which is capable of explaining most of the results, that is:

1) Ledges (of approximately monatomic height) are formed at both the edges of the crystal and at positions where dislocations intersect the surface.

2) Both monomer and dimer molecules are formed at sites on these ledges.

3) The surface diffusion rate of molecules away from the ledges and the desorption rate of these molecules from the surface are comparable and rapid.

Let us consider the third hypothesis first. Knacke, Stranski and Schmolke[30] have followed the evaporation rates of KCl and KI as a function of pressure. They found that the vaporization coefficient,

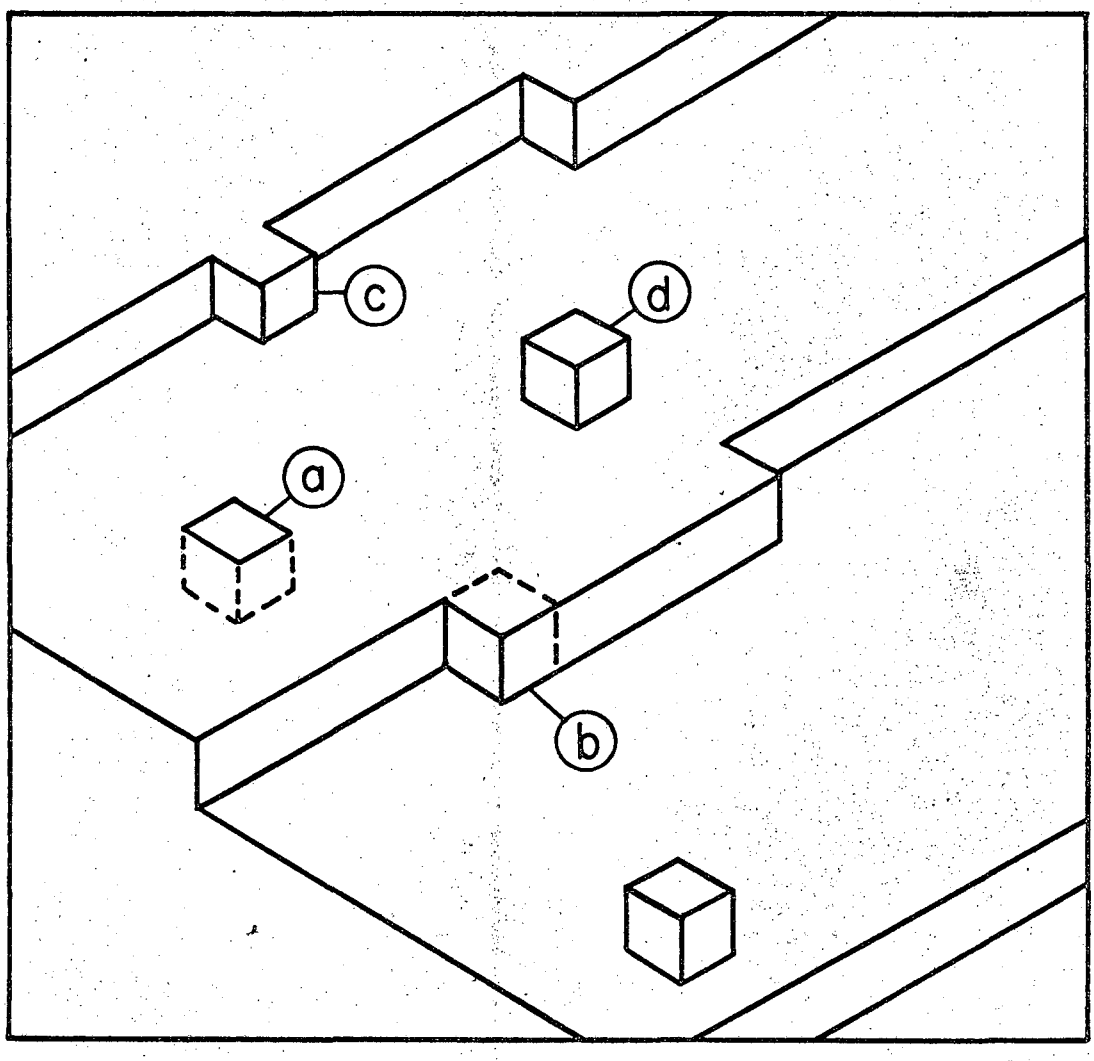

MUB-11115

Fig. VII-2 Kossel-Stranski model of a crystal surface

α_v, was higher than 1/3 and lower than 2/3 at high undersaturations (far from equilibrium, $(P_{eq}-P)/P_{eq} = 1$) and decreased with decreasing undersaturation ($P \rightarrow P_{eq}$). Jaeckel and Peperle[31] found similar results for NaCl, in good agreement with our free vaporization data. Knacke, et al. made electron micrographs of the surface after evaporation for several undersaturations (pressures). At high undersaturations (free vaporization conditions) the surface was completely roughened after evaporation and the distance between macroscopic steps was about 10^{-5} to 10^{-6} cm. These values are equal to or smaller than the values of the equilibrium ledge spacing estimated by Hirth and Pound. If the undersaturation was lowered the step structure of the same sample becomes smooth again, i.e., the spacing between ledges increases and α decreases. If the final desorption step was "rate determining" then the surface diffusion step occurring before desorption should lead to an "equilibrium" ledge spacing at any undersaturation.

Hove[59] has calculated the activation energy for diffusion of a KCl molecule on an infinite ideal surface and found it to be about 0.23 ev. The calculated binding energy was 0.36 ev. (These energies will be similar for NaCl.) Assuming that the frequency factors for these motions are similar ($\sim 10^{12}$ sec^{-1}) then the mean path length of a molecule would be at most a few lattice spacings before it evaporates (on a plane surface). This implies that surface diffusion does not play an important role in the vaporization of the alkali halides.

In support of 2 we found that the difference between the activation energies of the monomer and dimer ($E_D^*-E_M^*$) was essentially constant for all of the NaCl crystals, within the accuracy of our experiments. If the dimer were formed by the reactions of two monomer molecules adsorbed

on the surface then the dimer to monomer ratio should go up as a function of monomer concentration, i.e.,

$$D/M \propto M \quad \text{or} \quad M/D \propto 1/M$$

For crystals which have a high vaporization flux (strained crystals) there are more monomer molecules on the surface; but, if anything the dimer to monomer ratio goes down (M/D goes up) for these crystals with respect to the lower vaporization rate crystals (low dislocation density crystals).

In this model the monomer-dimer ratio is fixed by the difference in the energy necessary to remove a monomer or dimer, respectively, from the kink.

The increase of the activation energy with increasing dislocation density can be explained by considering the effect of ledge spacing on the potential energy of an ion pair (molecule) on the surface. Lennard-Jones and Dent[19] have shown that the potential energy of an ion pair on the surface has a larger contribution from interaction with ions in the same plane than from interaction with ions in underlying planes in the bulk lattice. The energy due to a partial plane at a distance, r, from the ledge associated with this plane decreases slowly with respect to r.

Thus, as the ledge spacing decreases, the potential energy of the molecules between the ledges increases since their interaction with more than one ledge must be considered.

Proposition 1) is fairly obvious. Dislocations can serve as nucleation sites in crystal growth,[12,13] and thermal etch pits[60,61] have been observed on alkali halide crystals at the points of emergence

of dislocations on the surface. Thus increasing the dislocation density will increase the number of ledge nucleation sites and thus increase the density of kinks on the surface.[12] This increase in kink density will increase the total vaporization rate, as can be seen from Eq. VII-1.

D. Suggestions for Further Experiments to Test the Proposed Model

Two experiments which should shed some light on whether the dimer is formed from two mobile monomers or at a kink site are the following.

1) Direct a molecular beam of an isotopically labeled monomer onto a surface at a rate low enough not to appreciably increase the surface concentration and look for the formation of dimers from two labeled monomers. This beam could be formed by effusion from a super heated vapor. It would have to be pulsed and the surface cleared of isotopically labeled atoms between pulses in order to minimize the effect of isotopes substituting into surface sites and introducing ambiguity into the position of dimer formation.

2) The energy difference between removing a monomer and a dimer from a kink should be calculable. If the experimental energy difference between monomer and dimer activation energy of this halide are the same with respect to the calculation as NaCl is then this would be additional evidence for the formation of both monomer and dimer at the kink position.

ACKNOWLEDGEMENTS

Of the many people who have been of assistance in the completion of this research I am especially grateful to : Professor G. A. Somorjai for his help as my research director and for the many informative and inspirational discussions we have had; the members of the research group for their many suggestions and aid; Duane Newhart for the use of his zone refining apparatus; Pat Cookson and Charlotte Machen for their typing of this thesis and for listening to my conversation for three years; my wife, Jane, for her understanding and encouragement during the research and writing and for her help in the preparation of the manuscript; and to NSF for its fellowship support.

This work was performed under the auspices of the United States Atomic Energy Commission.

APPENDIX A

THEORY OF QUADRUPOLE MASS FILTER

The equations of motion of an ion in a time varying field derived from a quadratic potential $\Phi(\vec{r}, t)$ has been given by Paul[51] and is summarized here. A DC voltage and superimposed RF voltage are imposed on the quadrupole rods as shown in Fig. A-1. If the rods were hyperbolic cylinders, the potential of this electrostatic field would be,

$$\Phi = (V_1 + V_0 \cos \omega t)(y^2 - z^2)/r_o^2 \qquad \text{(A-1)}$$

The force exerted on a charged particle in the ith direction by this field is

$$F_i(t) = e\, E_i(t) = e\, \frac{\partial V(\bar{r},t)}{\partial q_i} \qquad \text{(A-2)}$$

$$(i = x,y,z)$$

The trajectory of such a particle is described by the vector equation, obtained by force balance,

$$m\, \frac{\partial^2 q_i(t)}{t^2} - e\, \frac{\partial V(\bar{r},t)}{\partial q_i} = 0 \qquad \text{(A-3)}$$

Using Eq. (A-1) and the above form for $\Phi(\bar{r},t)$, Eq. (A-3) is resolved into its three cartesian components.

$$m\, \frac{\partial^2 m}{\partial t^2} = 0 \qquad \text{(A-4)}$$

$$\frac{\partial^2 y}{\partial t^2} - \frac{2e}{mr_o^2}\, (V_1 + V_0 \cos \omega t)y = 0 \qquad \text{(A-5)}$$

$$\frac{\partial^2 z}{\partial t^2} + \frac{2e}{mr_o^2}\, (V_1 + V_0 \cos \omega t)z = 0 \qquad \text{(A-6)}$$

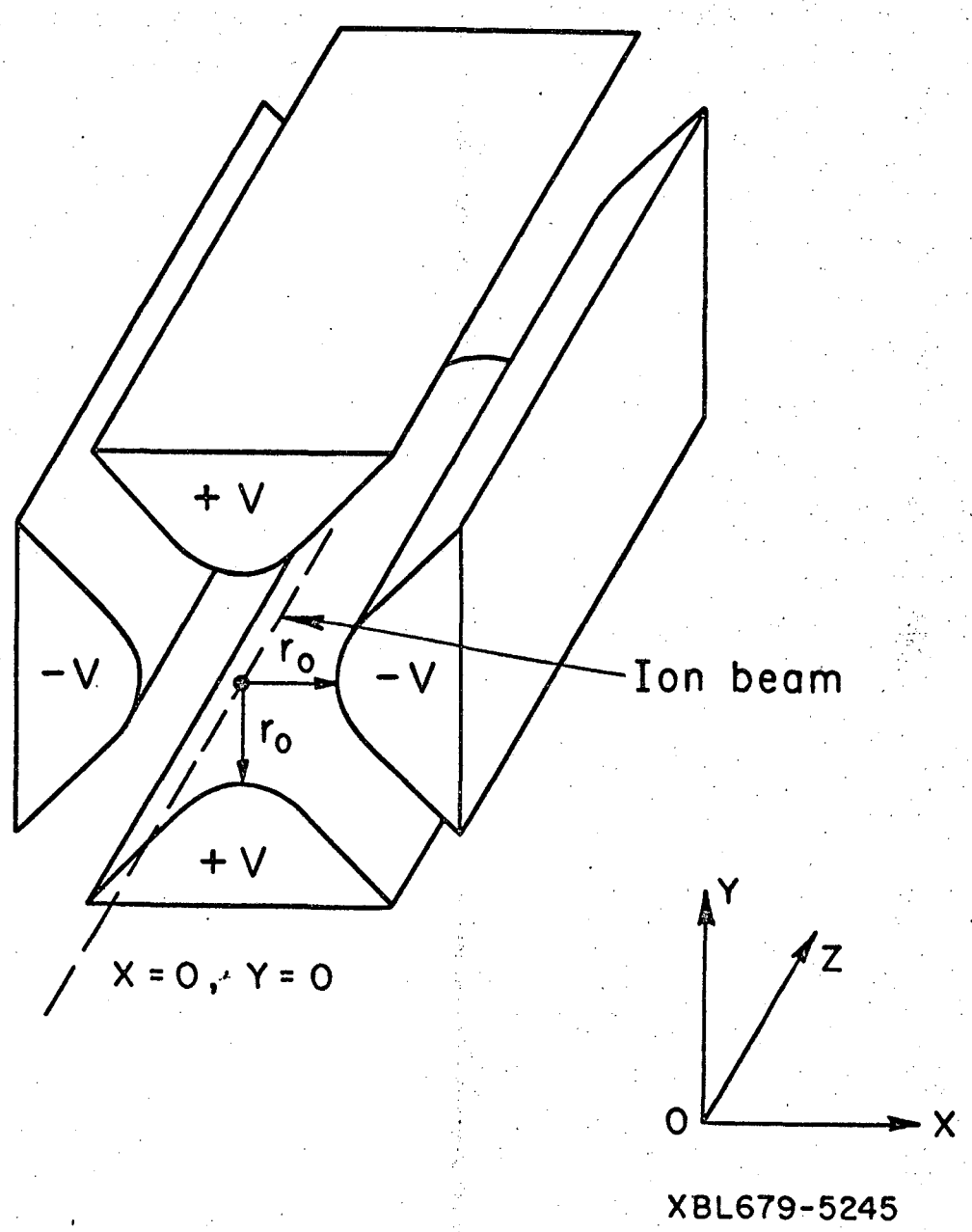

Fig. A-1 Voltage configuration on idealized hyperbolic quadrupole rods

These equations are re-arranged into a more convenient form,

$$m \frac{\partial^2 x}{\partial t'^2} = 0 \qquad \text{(A-7)}$$

$$\frac{\partial^2 y}{\partial t'^2} + (-a - 2q \cos zt')y = 0 \qquad \text{(A-8}$$

$$\frac{\partial^2 z}{\partial t'^2} + (a - 2q \cos zt')z = 0 \qquad \text{(A-9)}$$

where $t' \equiv \omega t/z$; $a \equiv \dfrac{8eV_1}{r_o^2 m\omega^2}$; $q = 4eV_0/r_o^2\omega^2 m$.

Equation (A-7) is readily solved to yield the trajectory along the axis of the quadrupole array.

$$x(t) = vt \qquad \text{(A-10)}$$

where v is simply $\sqrt{eZV_{F.C.}/m}$, where $V_{F.C.}$ is the voltage of the Faraday cage in the ionizer and z is the ion charge (usually 1) and the time-origin is measured from that time when the ion enters the quadrupole array.

Except for a sign, Eqs. (A-8) and (A-9) are identical and are expressed here in general form.

$$\frac{\partial^2 \xi}{\partial t'^2} + (a - 2q \cos \omega t')\xi = 0 \qquad \text{(A-11)}$$

Equation (A-11) is the canonical form of the Mathieu Equation, without a damping term $(k\partial\xi/\partial t')$ or a phase shift. The solution is well known and tabulated from such problems as tidal waves in cylindrical vessels with elliptical boundaries, decay of magnetic forces in metal cylinders, the mechanical spring problem with a spring constant which varies

sinusoidally with position, and criticallity calculations of cylindrical reactor cores with elliptical boundary conditions.

The general solution to Eq. (A-11) is

$$\xi(t') = Ae^{\mu t'} \sum_{-\infty}^{+\infty} C_n e^{int'} + Be^{-\mu t'} \sum_{-\infty}^{+\infty} C_n e^{-int'} \qquad \text{(A-12)}$$

This leads to two types of solutions. The first will be called stable since as $t' \to \infty$, ξ remains finite for all t'. The other will be called unstable since as $t' \to \infty$, $\xi \to \infty$. μ, which is called the characteristic exponent determines which type of solution is present. μ is defined unambiguously by the parameters a and q. The following cases are distinct possibilities:

a) $\mu = i\beta$, pure imaginary, β not a whole number $\to$ stable solution.

b) $\mu = in$, n a whole number $\to$ a non-trivial, limited, periodic solutions. Each of these linearly independent solutions is unstable.

c) μ is complex, the solution is unstable unless $A = 0$.

The stability of the solution depends only upon μ and thus upon a and q, which do not contain the initial conditions. One can define areas in the (a,q) plane for which all (a,q) values lead to stable solutions. In this way one obtains the stability diagram which is shown in Fig. A-2. Only those ions for which both the y and z orbit are stable will have stable trajectories. Thus the points (a_y, q_y) and (a_z, q_z) must both lie in a stable region. $a_y = -a_z$ and $q_y = -q_z$. If the (a,q) plane is reflected at both the a and q axis then the points (a_y, q_y) and (a_z, q_z) are superposed.

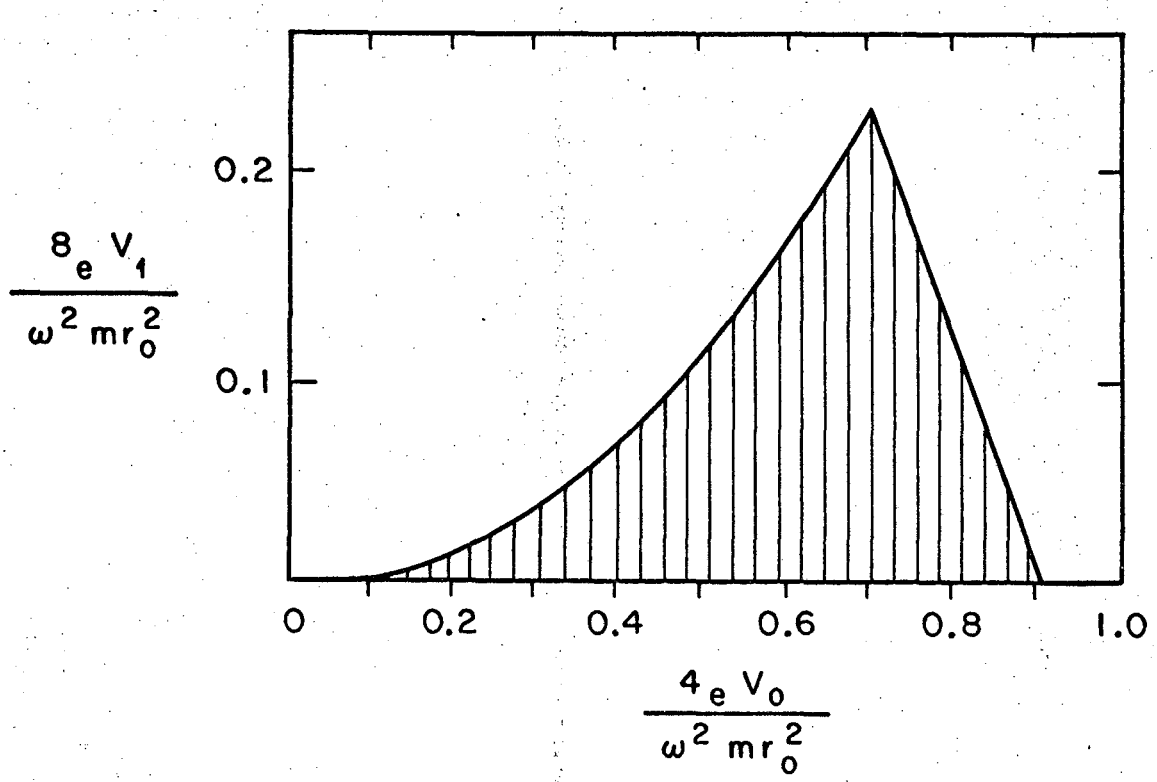

QUADRUPOLE STABILITY DIAGRAM

XBL679-5255

Fig. A-2 Quadrupole stability diagram

For fixed values of the field parameters, r_o, ω, V_1 and V_0 all ions of the same m/e have the same (a,q). Since the relation $a/q = 2, V_1/V_o$ does not contain the mass of the ion. The operating points of all ions, regardless of mass lie on the same straight line, the mass line, through the origin of the stability diagram. By increasing V_1/V_0 the stable q-interval, which corresponds to a stable mass interval may be made so small that only ions of one mass are able to pass through the field. This is the action of the mass filter which permits its use as a mass spectrometer. Only masses in the interval

$$q_1\left(\frac{r_o^2\omega^2}{4\,V_0}\right) \leq \frac{e}{m} \leq q_2\left(\frac{r_o^2\omega^2}{4\,V_0}\right)$$

where q_1 and q_2 are the intercepts of the mass line with the boundaries of the stable region.

The limitations on the mass filter are:

1) The derivation given above has assumed that the rods are infinitly long in order to remove all unstable ions. The finite length of the rods demands that the ion transit time be much longer than the period of oscillation of the R.F. voltage.

2) Even though an ion may theoretically exhibit a stable orbit its amplitude may exceed the pole spacing, r_o, and it will be lost. This effect is a function of the mass, the initial coordinates at which the ion entered the quadrupole, its radial velocity on entry, and the amplitude of the field at its entry time.

APPENDIX B

QUADRUPOLE MASS TRANSMISSION AND IONIZATION CROSS-SECTIONS

As discussed in Appendix A the stability of an ion in the quadrupole field depends on its entrance conditions and other factors which cannot be theoretically calculated. Therefore, in order to compare our relative ion intensities to those obtained with other types of mass spectrometers, it is necessary to calibrate the ion transmission of the quadrupole as a function of mass. The way that we chose to do this was to take mass spectra of known organic compounds and to compare these spectra with the A.P.I. published spectra taken on magnetic deflection types of mass spectrometers.[62]

The compounds chosen were spectroquality n-heptane and n-hexane. These compounds were introduced into the mass spectrometer at a constant rate through a pin hole in a gold foil leak from the gas handing manifold. A pressure in the manifold of ~200μ was sufficient to obtain reproducible spectra. The relative peak heights in our spectra were compared to the relative peak heights in the published spectra (m/e = 43 as reference) and the ratio of our results to the accepted results taken as the transmission ratio, τ_m, for that mass. A plot of τ_m as a function of mass is shown in Fig. B-1.

Certainly part of this ratio is not due to quadrupole transmission factors, but to differences between our ionizer region and the one in the mass spectrometer used to obtain the published spectra.

Another way of checking the transmission and ionization efficiencies of our instrument is by comparing our Knudsen effusion data to a reported monomer to dimer pressure ratio from an effusion source. Gorokhov[56] has reported that the monomer dimer ratio is ~3.0 at T = 1000°K.

Our data yields

$$I_{23} = 5.5\times10^{-5}$$

$$I_{58} = 7.05\times10^{-5}$$

$$I_{81} = 4.07\times10^{-5}$$

Thus, without any corrections

$$\frac{I_M}{I_D} = \frac{12.6}{4.1} = 3.1$$

The pressure ratio is given by

$$\frac{P_M}{P_D} = \frac{I_M\ \tau_D\ \sigma_D}{I_D\ \tau_M\ \sigma_M}$$

where the τ's are transmission corrections and the σ's are ionization cross sections. $\tau_D/\tau_M \sim .4/.8$, which would lead to $\sigma_D/\sigma_M \sim 2$ in order to obtain the reported pressure ratio. This cross section ratio is the one that would be assumed from the additivity rule used by many mass spectroscopists in the absence of other information. Berkowitz[54] has found $\sigma_D/\sigma_M = 1.25$ at 70 eV by comparing his mass spectrometric data to Miller and Kusch's[21] molecular beam data. However, there is a question of the accuracy of the latter data since there is evidence[63] that the NaCl reacted with the copper cell used as an effusion source.

In order to get agreement between our data and that of Gorokhov, we will choose $\tau_D\sigma_D/\tau_M\sigma_M \sim 1$ in the analysis of our data. This assumption results in reasonably good agreement between our free vaporization data and that of Rothberg, Eisenstadt and Kusch.[22]

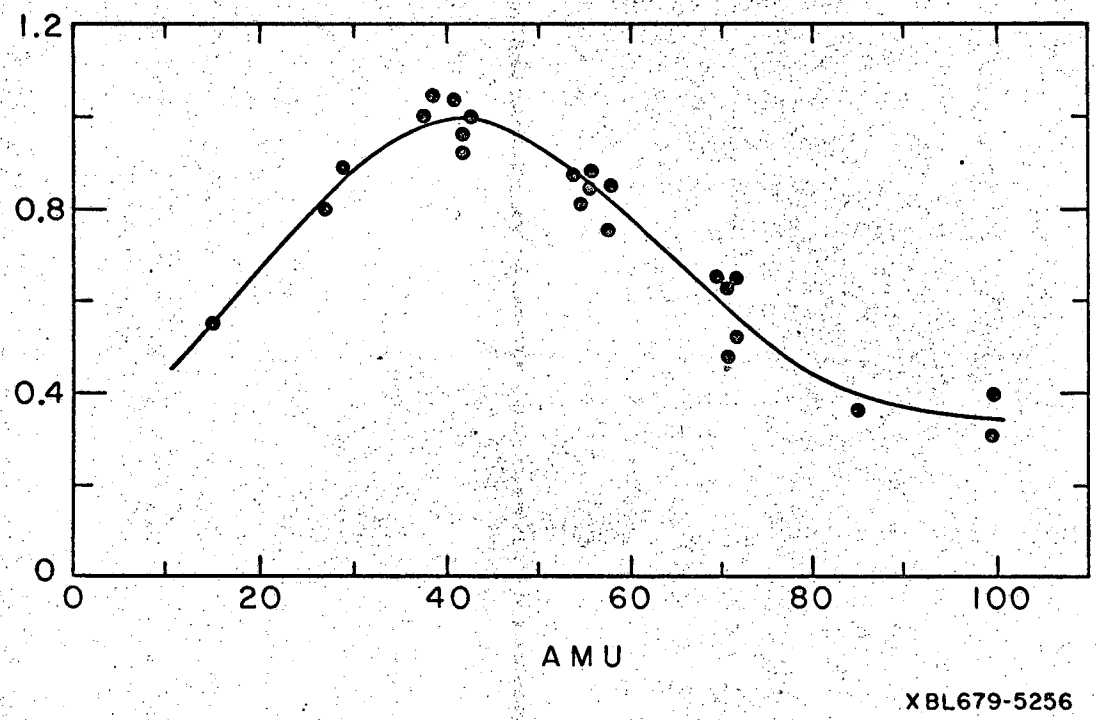

Fig. B-1 Quadrupole transmission probability (normalized to m/e = 43).

APPENDIX C

MASS SPECTROMETRIC DATA ANALYSIS

The mass spectrometric data were analysed to obtain a least squares fit to the experimental data with standard deviation, σ_S, and the several activation energies on the Lawrence Radiation Laboratory CDC 6600 computer. Standard deviations for both the slope and intercept were also computed.

The intensity of the peak used to characterize one of the ion species (e.g., m/e = 58 for $NaCl^+$) was corrected for the isotopic abundance of the constituent atoms so that the total ion species intensity was obtained.

The program fits a line to the data expressed as log IT = A +B/T. Then it compares the deviations of the data points to the standard deviation. Any points more than 2.5 σ from the line are discarded and the curve refit. This is continued until all the remaining points are within 2.5 σ of the fitted curve. Generally this only discarded data points in which an error in the order of magnitude of the intensity had been made when the data was reduced to cards or tape. The program then drew a graph of all the intensity data and the fitted curve for each of the ions of interest. A listing of the program except for the plotting subroutine which is a library subroutine in this computer follows.

```
      SUBROUTINE DATFIT(K,N,A)
      COMMON/TMM/TMM(3,2),QCALC(3,2),T(200),Q(200)
      COMMON/AR/AR(3,200,3),AMASS(5)
      DIMENSION A(3),QT(200),TCUR(200)
      J=0
      ITER=1
      DO 10 L=1,N
      IF(Q(L).EQ.-4.0) GO TO 10
      J=J+1
      QT(J)=Q(L)
      TCUR(J)=T(L)
 10   CONTINUE
 5    CALL LINLSQ(TCUR,QT,J,A,SIGMA,SA,SB)
      PRINT 1,K,ITER,A(1),A(2),SIGMA,SA,SB
    1 FORMAT(// 20H PARAMETERS FOR ION,I1,5X,9HITERATION,I2/5X,
     X 5HA(1)=,E12.4,5X,5HA(2)=,E12.4,5X,6HSIGMA=,E12.4,5X,3HSA=,E12.4
     X ,5X,3HSB=,E12.4)
      JJ=0
      DO 20 L=1,N
      AR(K,L,3)= A(1)+A(2)*T(L)
      IF( (ABS(AR(K,L,3)-Q(L))- 2.5*SIGMA).GT.0.0) GO TO 20
C     POINTS WITH DEVIATION GREATER THAN 2.5*SIGMA ARE DISCARDED AND
C     THE CURVE IS REFITTED UNTIL ALL REMAINING POINTS ARE WITHIN
C     2.5*SIGMA -THIS IS ABOUT THE .95 CONFIDENCE LEVEL
      JJ=JJ+1
      QT(JJ)=Q(L)
      TCUR(JJ)=T(L)
 20   CONTINUE
      IF(JJ.EQ.J) GO TO 6
      J=JJ
      ITER=ITER+1
      GO TO 5
 6    DELTAH=-A(2)*1.987*2.303
      SIGMAH=1.987*2.303*SB
      PRINT 2,DELTAH,SIGMAH
    2 FORMAT(10X,7HDELTAH=,E12.4,5X,8HSIGMA H=,E12.4)
      QCALC(K,1)=A(1)+A(2)*TMM(K,1)
      QCALC(K,2)=A(1)+A(2)*TMM(K,2)
      RETURN
      END
```

XBL 679-4869

```
      SUBROUTINE MAXMIN(TINV,N,TMAX,TMIN)
      DIMENSION TINV(N)
      TMAX=TINV(1)
      TMIN=TINV(1)
      DO 10 I=1,N
      IF (TMAX-TINV(I))1,2,2
    1 TMAX=TINV(I)
    2 IF (TMIN-TINV(I))10,10,3
    3 TMIN=TINV(I)
   10 CONTINUE
      RETURN
      END
```

```
      SUBROUTINE GRAPH(K,LABEL,I)
      COMMON/TMM/TMM(3,2),QCALC(3,2),T(200),Q(200)
      DIMENSION K(3) ,Y(2),TINV(2)
      COMMON/TVPOOL/XMIN,XMAX,YMIN,YMAX,TVXMIN,TVXMAX,TVYMIN,TVYMAX
      XMIN=1.05E-03   $XMAX=1.50E-03
      YMIN=-10.     $ YMAX=-4.
      CALL TVGRID(1,9,6HNOLBLS,1,6)
      CALL TVLBL(9,6)
      IP=K(I)
      IF(I.EQ.1) KK=23
      IF(I.EQ.2) KK=7
      IF(I.EQ.3) KK=6
      CALL TVPLOT(T,Q,IP,6HNOJOIN,KK,1)
      Y(1)=QCALC(I,1)
      Y(2)=QCALC(I,2)
      TINV(1)=TMM(I,1)
      TINV(2)=TMM(I,2)
      CALL TVPLOT(TINV,Y,2,4HJOIN)
      CALL TVLTR(12.,12.,0,3,LABEL,10)
      CALL TVLTR(400.,15.,0,2,3H1/T)
      CALL TVLTR(15.,530.,1,2,7HLOG(IT) )
      IF(I.LT.3)  RETURN
      CALL TVNEXT
      RETURN
      END
```

XBL 679-4871

```
      PROGRAM MSDDAS(INPUT,OUTPUT,TAPE6,TAPE98,TAPE99)
C     MASS SPEC DATA ANALYSIS
C     NO CORRECTION FOR TRANSMISSION RATIOS,ELECTRON CURRENT,CROSS SECT.
      LOGICAL INDEF
      COMMON/AR/AR(3,200,3),AMASS(5)
      DIMENSION K(3),A(3),AISOT(5)
      COMMON/TMM/TMM(3,2),QCALC(3,2),T(200),Q(200)
C     AISOT=INVERSE OF RATIO OF CONCENTRATIONS OF ISOTOPES IN MEASURED
C     PEAK TOALL ISOTOPES IN ATOMS OF ION
C     NO MORE -AS LABEL IN DATA CARDS TERMINATES PROCESSING
      PRINT 99
 200  CALL RETRV(K,LABEL,NP)
      IF( NP.EQ.999) GO TO 151
      AISOT(1)=1.0  $AISOT(2)=1.32398  $AISOT(3)=1.32398
      AISOT(4)=1.00  $AISOT(5)=1.00
      PRINT 99
 99   FORMAT(1H1)
      DO 90 I=1,3
      KP=K(I)
      CALL TEMPER(I,KP)
      DO 30 L=1,KP
      IF(INDEF(AR(I,L,2))) GO TO 28
      IF( AR(I,L,2) ) 28,28,21
 28   Q(L)=-4.0
      GO TO 29
 21   Q(L)= AR(I,L,2)*AISOT(I)/T(L)
      Q(L)=ALOG10(Q(L))
 29   AR(I,L,2)= Q(L)
   30 CONTINUE
      CALL DATFIT(I,KP,A)
C     DATFIT RETURNS PARAMETRES OF FITTING CURVE AND DEVIATIONS
      PRINT 7,I,I,I
 7    FORMAT(//  *        1/T(*,I1,1H),*        IT(*,I1,1H),
     X *      ITCALC(*,I1,1H) )
      PRINT 6, ((AR(I,J,N),N=1,3),J=1,KP)
 6    FORMAT( 3(5X,E12.4) )
      PRINT 99
      CALL GRAPH(K,LABEL,I)
 90    CONTINUE
      GO TO 200
 151  CALL TVEND
      STOP
      END
```

XBL 679-4867

```
      SUBROUTINE RETRV(K,LABEL,NP)
      COMMON/AR/AR(3,200,3),AMASS(5)
      DIMENSION K(3)
      IEOF=7HENDFILE
      INTEGER TERMIN
      TERMIN=7HNO MORE
 11   READ 1, LABEL
 1    FORMAT(A10)
      IF ( LABEL.EQ. TERMIN ) GO TO 100
      IT=6
 12   READ (6) LBL
      IF(LBL.EQ.LABEL ) GO TO 15
      IF (LBL.EQ.IEOF) GO TO 5
      DO 99 IJ=1,4
      READ(6) DUMMY
 99   CONTINUE
      READ (6) EOF
      IF (ENDFILE 6) 12,7
 7    PRINT 6,LBL,LABEL,IT
 6    FORMAT(5X,A10,*SOMEHOW AN EDNFILE HAS DISAPPEARED*/
     1*  THIS SET OF DATA *,A10, *HAS NOT BEEN READ ON TAPE*,I2)
      GO TO 5
 15   READ(6) K(1),K(2),K(3)
      DO 10 I=1,3
      L=K(I)
      READ(6)  ((AR(I,J,1),AR(I,J,2)),J=1,L)
 10   CONTINUE
      READ(6) EOF
      PRINT 13, LABEL,K(1),K(2),K(3)
 13   FORMAT(/13H DATA LABEL= ,A10,*NO. OF PTS. IN ARRAYS ARE*,3I10)
      NP=0
      KKK=MAX0(K(1),K(2),K(3))
      PRINT9,(((AR(I,J,1),AR(I,J,2)),I=1,3),J=1,KKK)
 9    FORMAT( 3(10X,2E12.4))
C  THIS IS NOT THE ORDER THAT THE POINTS WERE READ ONTO THE TAPE.
      REWIND 6
      RETURN
 5    PRINT 60, LABEL
 60   FORMAT(A10,* ISNOT ON TAPE 6 * )
      GO TO 11
 100  NP=999
      REWIND 6
      RETURN
      END
```

XBL 679-4868

```
      SUBROUTINE LINLSQ(X,Y,N,A,SIGMA,SA,SB)
      DIMENSION X(N),Y(N),A(2)
C     LINLSQ IS A LINEAR LEAST SQARES FIT
C     N=NUMBER OF POINTS,A*S ARE PARAM. OF LINE
C     SIGMA = RMS DEV.
C     SA=STD.DEV. OF INTERCEPT/SB=STD.DEV. OF SLOPE
      FN=FLOAT(N)
      SUMX=0.0
      SUMYSQ=0.0
      SUMY=0.0
      SUMXSQ=0.0
      SUMXY=0.00
      SUMDEV=0.0
      DO 10 I=1,N
      SUMX=SUMX+X(I)
      XSQ=X(I)*X(I)
      XY=X(I)*Y(I)
      SUMXSQ=SUMXSQ+XSQ
      SUMY=SUMY+Y(I)
      SUMYSQ=SUMYSQ+Y(I)*Y(I)
      SUMXY=SUMXY+XY
   10 CONTINUE
      A(2)=(SUMX*SUMY-FN*SUMXY)/(SUMX*SUMX-FN*SUMXSQ)
      A(1)=(SUMY-A(2)*SUMX)/FN
      SIGMA=SQRT((SUMYSQ-A(1)*SUMY-A(2)*SUMXY)/(FN-1.))
      SB=SIGMA*SQRT(FN/(FN*SUMXSQ-SUMX**2))
      SA=SIGMA*SQRT(SUMXSQ/(FN*SUMXSQ-SUMX**2))
      RETURN
      END
```

```
      SUBROUTINE TEMPER(I,KP)
      COMMON/AR/AR(3,200,3),AMASS(5)
      COMMON/TMM/TMM(3,2),QCALC(3,2),T(200),Q(200)
      DO 20 J=1,KP
      V=AR(I,J,1)*1000.
      T(J)= 32.945+V*(121.88+V*(-3.039+V*0.094))
      T(J)= 1./(T(J)+ 273.2)
      AR(I,J,1)= T(J)
 20   CONTINUE
      CALL MAXMIN(T,KP,TMAX,TMIN)
      TMM(I,1)=TMIN
      TMM(I,2)=TMAX
      RETURN
      END
```

XBL 679-4870

APPENDIX D

SYMBOLS USED

ρ_v	gas density
$\bar{v}$	most probable gas velocity
N	number of molecules
n	number of moles
m	molecular weight in grams per molecule
ϵ_o	zero point energy of the solid
k	Boltzmann constant
T	absolute temperature
h	Planck constant
ν	frequency of vibration
Q	partition function
α_v	vaporization coefficient
λ_o	mean distance between ledges
d_o	mean distance between "kinks"
E_c	lattice crystallization energy
w_1	formation energy of a single "kink"
$\bar{x}$	mean free path of an adsorbed atom
D_s	surface diffusion coefficient
ΔF^*	activation free energy
P	pressure
P_{eq}	equilibrium pressure
R	gas constant

ΔH°	standard enthalpy of reaction
R_v	vaporization rate
ϵ	emissivity
κ	thermoconductivity
K_{SB}	Stefan-Boltzmann constant
m/e	mass to charge ratio of an ion
P'	apparent pressure.
M	molecular weight in grams per mole
E^*	activation energy of a reaction
I	ion current
(hkℓ)	Miller indices of a crystal face

REFERENCES

1. JANAF Thermochemical Tables, (Dow Chemical Co., Midland, Michigan, Dec. 1960).

2. J. Drowart, in Condensation and Evaporation of Solids (Gordon and Breach, New York, 1964).

3. B. Paul, A. R. S. Journal 32, 1321-1328 (1962).

4. I. Karutz, I. N. Stranski, Z. Anorg. Allg. Chemie 292, 330 (1957).

5. E. R. Rideal, Pk. M. Wiggins, Proc. Roy. Soc. A210, 291 (1952).

6. J. S. Kane, Ph. D. Thesis, University of California, Berkeley, UCRL-2957 (1955).

7. G. M. Rosenblatt, P. K. Lee, M. B. Dowell, J. Chem. Phys. 45, 3454 (1966).

8. G. A. Somorjai, J. E. Lester, J. Chem. Phys. 43, 1450 (1965); G. A. Somorjai, H. B. Lyon, J. Chem. Phys. 43, 1456 (1965).

9. O. Knacke, I. N. Stranski, Progr. Met. Phys. 6, 181 (1956).

10. W. Hirschwald, I. N. Stranski, in Condensation and Evaporation of Solids (Gordon and Breach, New York, 1964).

11. G. A. Somorjai, J. E. Lester, in Progress in Solid State Chemistry (Pergamon Press, Oxford, England, 1967), Vol. IV.

12. W. K. Burton, N. Cabrera, F. C. Frank, Phil. Trans. Roy. Soc. 243A, 299 (1951).

13. A. A. Cerhnov, Soviet Physics Uspekhi, 4, 116 (1961).

14. J. P. Hirth, G. M. Pound, J. Chem. Phys. 26, 1216 (1957).

15. L. Brewer, E. Brackett, Chem. Revs. 61, 4 (1960).

16. R. W. Dreyfus, A. S. Nowick, I. B. M. Research Paper, R.C.-531(1961).

17. M. P. Tosi, in Solid State Physics, XVI (Academic Press, New York p. 1 (1964).

18. J. Hove, J. A. Krumhansl, Phys. Rev. 92, 569 (1953).

19. J. E. Lennard-Jones, B. M. Dent, Trans. Faraday Soc. 24, 92 (1928).

20. G. C. Benson, P. I. Freeman, E. Dempsey, J. Chem. Phys. 39, 302 (1965).

21. R. C. Miller, P. Kusch, J. Chem. Phys. 25, 860 (1956).

22. G. M. Rothberg, M. Eisenstadt, P. Kusch, J. Chem. Phys. 30, 517 (1959).

23. I. Langmuir, Phys. Rev. 2, 329 (1913).

24. R. J. Ackermann, R. J. Therm. G. H. Winslow, Argonne National Lab. Report, A.N.L. 6663 (1962).

25. K. Neumann, Z. Physik. Chem. 196, 16 (1950).

26. W. Kossel in Falkenhangen, Quantentheorie und Chemie, Vorgra, Leipzig, 1928; Naturwissenschaften 18, 901 (1930); Ann. Phys. 33, 651 (1938).

27. I. N. Stranski, Z. Phys. Chem. 136, 259 (1928).

28. W. K. Burton, N. Cabrera, F. C. Frank, Phil. Trans. Roy. Soc. (London) A243, 299 (1951).

29. J. P. Hirth, G. M. Pound, J. Chem. Phys. 26, 1216 (1957).

30. O. Knacke, R. Schmolke, I. N. Stranski, Z. Kristallogr. 109, 184 (1957).

31. R. Jaeckel, W. Peperle, Z. Physik. Chemie (Leipzig) 217, 321 (1961).

32. J. P. Hirth, G. M. Pound, J. Phys. Chem. 64, 619 (1960).

33. Harshaw Chemical Co., Solid State Division, Cleveland, Ohio.

34. R. W. Dreyfus, in The Art of Science of Growing Crystals (John Wiley and Sons, Inc., New York, 1965).

35. S. Kyropoulos, Z. Anorg. Allgem. Chem. 154, 308 (1926).

36. R.W. Warren, Rev. Sci. Instrum. 36 (6) 731 (1965).

37. Semi-Elements, Inc., Saxonburg, Pa. 16056.

38. W. Känzig, J. Phys. Chem. Solids 23, 479 (1962).

39. W. Känzig, M. H. Cohen, Phys. Rev. Letters 3, 509 (1959).

40. C. C. Klick, J. H. Schulmann, Solid State Physics, Vol. V (Academic Press, New York, 1958).

41. R. W. Davidge, Phil. Mag. 8, 359 (1963); R. W. Whitworth, Phil. Mag. 10, 801 (1964).

42. J. C. Fisher, W. G. Johnston, R. Thomson, T. Vreeland, jr. Dislocations and Mechanical Properties of Crystals (John Wiley and Sons, Inc., London, 1957).

43. R. W. Whitworth, Phil. Mag. 15, 305 (1967).

44. A. H. Cottrell, Dislocations and Plastic Flow in Crystals (University Press, Oxford, 1958).

45. D. Krasnopolsky de Grinberg, A. Grinberg, Czechoslov. J. Phys. 11, 609 (1961).

46. V. Ruth, J. P. Hirth, in Condensation and Evaporation of Solids (Academic Press, New York, 1964).

47. A. W. Czanderna, J. M. Honig, Anal Chem. 29, 1206 (1957).

48. Vacuum Microbalance Techniques, Vols. I-IV (Plenum Press, New York, 1961).

49. Electronic Associates, Inc., Palo Alto, Calif.

50. J. R. Pierce, Theory and Design of Electron Beams, (D. Van Nostrand Co., Princeton, N. J., 1954).

51. W. Paul, H. P. Reinhard, U. Von Zahn, Z. Physik 152, 143 (1958).

52. W. L. Winterbottom, J. P. Hirth, in Condensation and Evaporation of Solids (Gordon and Breach, New York, 1964).

53. C. A. McDowell, Mass Spectrometry (McGraw-Hill Book Co., New York, 1963).

54. J. Berkowitz, W. A. Chupka, J. Chem. Phys. 29, 653 (1958).

55. L. N. Gorokhov, U. S. Khodev, P. A. Akishin, Zhur. Neorg. Khom 3, 2597 (1958).

56. P. A. Kishin, L. N. Gorokhov, L. N. Sidorov, Zhur. Fiz. Khim. 33 2822 (1959).

57. B. H. Zimm, J. E. Mayer, J. Chem. Phys. 12 (9), 362 (1944).

58. T. A. Milne, H. M. Kelin, J. Chem. Phys. 33, 1628 (1960).

59. J. E. Hove, Phys. Rev. 99 (2) 480 (1955).

60. H. Bethge, G. Kastner, M. Krohn, Z. Naturforshung 16a, 321 (1961).

61. E. Kern, H. Pick, Z. Physik, 134, 610 (1953).

62. American Petroleum Institute, Research Project 44. Mass spectral Data.

63. J. Berkoqitz, H. A. Tasman, and W. A. Chupka, J. Chem. Phys. 36 (8), 2170 (1962).

This report was prepared as an account of Government sponsored work. Neither the United States, nor the Commission, nor any person acting on behalf of the Commission:

A. Makes any warranty or representation, expressed or implied, with respect to the accuracy, completeness, or usefulness of the information contained in this report, or that the use of any information, apparatus, method, or process disclosed in this report may not infringe privately owned rights; or

B. Assumes any liabilities with respect to the use of, or for damages resulting from the use of any information, apparatus, method, or process disclosed in this report.

As used in the above, "person acting on behalf of the Commission" includes any employee or contractor of the Commission, or employee of such contractor, to the extent that such employee or contractor of the Commission, or employee of such contractor prepares, disseminates, or provides access to, any information pursuant to his employment or contract with the Commission, or his employment with such contractor.